Inspection at Inaccessible Locations Using Medium-Range Guided Waves

Konstantinos Tzaferis

Department of Electronic and Electrical Engineering

University of Strathclyde

A thesis submitted for the degree of

Doctor of Philosophy

February 2024

Copyright

Signed:

Date: 26/3/2024

Acknowledgements

I would like to sincerely thank Professor Gordon Dobie for giving me the opportunity to be part of his research team. His continuous support, mentorship, encouragement, and advice were the key enabler to complete this research journey. I would like to thank my second supervisor Professor Anthony Gachagan for his support. I would also like to thank Morteza Tabatabaeipour for his constant help and patience. Our many conversations shaped the outcome of this work. I would also like to thank all my colleagues that I have worked with in the Centre for Ultrasonic Engineering (CUE) for their positive attitude, technical support, and innovative ideas.

Finally, I would like to thank Jessica, whose support through the last three years has meant so much to me. I would like to thank my parents Anna and Meletis for their continuous support and encouragement, and my brother Fotis and sister Sofi for believing in me.

Abstract

Medium-range guided wave testing is commonly employed for inspection of plate and plate-like structures. The method is attractive for crack imaging and wall loss quantification, especially in hidden locations where direct access is limited.

Lamb wave excitation at high-frequency-thickness products offers a potential solution for high-resolution guided wave testing, especially sensitive to vertical cracks and sharps pits. The technique usually works in pulse echo mode and at high frequency-thickness products, around 20 MHz·mm, offering good sensitivity and resolution. Defect sizing is based on the reflection amplitude of the received mode(s). However, the scattering of guided waves is complex, and the amplitude of the reflected modes does not provide sufficient information for defect sizing. This work aims to overcome this limitation using a focusing technique based on Lamb waves. Specifically, multiple Lamb wave modes are excited individually and superimposed to form a new mode with a desired through-thickness energy distribution. This way, energy is focused on a single point in the structure. Using weighting functions, the location of the focal point is swept across the thickness of the sample. The technique allows for accurate sizing of flaws, such as cracks and wall loss.

In contrast to abrupt thickness changes, corrosion scrabs can also appear as gradual wall thinning areas. The main objective is to determine the remaining wall thickness in the

affected area in order to decide further actions. For this reason, wall loss quantification is performed utilising the cut-off frequency of mode SH1. The approach requires the excitation of SH1 across a range of frequencies. For this reason, a novel excitation technique using guided wave phased array steering is developed. Specifically, an array generating shear horizontal waves is employed. The influence of the array's length, pitch, element width, and mode excitability on excitation is investigated. By appropriately phasing the elements of the array, mode SH1 is targeted and dynamically excited over a wide frequency-wavelength range. The directionality of SH1 is also studied, as in certain conditions, this can be critical for the success of the quantification. Simulation results show the technique can accurately quantify a 65% wall thinning defect, offering a 15% increase compared to established techniques. This is critical, as wall loss defects above 50% are considered severe. Additionally, using electronic steering, rapid quantification can be achieved. Experiments using an electromagnetic acoustic transducer and synthetic steering on an intact area and an artificially machined corrosion-like defect validate the technique.

Contents

List of Figures

List of Tables

Abbreviations

NDT: Non-Destructive Testing

MR-GWT: Medium-Range Guided Wave Testing

FMC: Full Matrix Capture

SH: Shear Horizontal

LR-GWT: Long-Range Guided Wave Testing

CHIME: Creeping Head-wave Inspection Method

M-skip: Multi Skip

HOMC: Higher Order Mode Cluster

EDM: Envelope Difference Coefficient

PPM: Periodic Permanent Magnet

EMAT: Electromagnetic Acoustic Transducer

PEC: Pulsed Eddy Current

SANR: Singla to Ambient Noise Ratio

SMNR: Signal to Modal Noise Ratio

2DFFT: 2-Dimensional Fast Fourier Transform

FEM: Finite Element Method

Chapter 1

Introduction

Context of Research

Over the past three decades, significant advancements have been made in enhancing ultrasonic techniques for non-destructive testing (NDT). The integration of new and sophisticated imaging algorithms, such as phase coherent imaging and the total focusing method [1,2], coupled with increased processing power using the graphics processing unit [3], has significantly enhanced short-range (bulk wave) ultrasonic testing. Concurrently, significant progress has been achieved in the area of long-range guided wave testing (LR-GWT) [4,5]. The technique is now commercially available and widely employed for rapid screening and monitoring of pipelines, especially in the oil and gas sector. Finally, recent research work is focused on the development of medium-range guided wave testing (MR-GWT). This ultrasonic technique is suitable for the inspection of components from a moderate distance (approximately up to 5 meters) from the probe location.

Bulk wave ultrasonic NDT is capable of delivering high-resolution imaging of areas directly beneath the probe, yet it necessitates physical access to the site under inspection. In contrast, long-range guided wave techniques obviate the need for such access, but don't provide the quantitative information that can be achieved from a localised inspection, such as defect depth. Moreover, due to their low operating frequency (~50 kHz), they are not sensitive to small defects, such as pitting. On the other hand, MR-GWT is designed to provide quantitative measurements. This methodology proves especially beneficial in circumstances where the inspection site is not directly accessible. A schematic example of an inspection at an inaccessible location is shown in Figure 1.1. The probe cannot approach the inspection area closer than 1 m due to the presence of a wall. This scenario is representative of the in-service inspection of the annular plate of storage tanks [6]. Other potential applications of MR-GWT include crack imaging [7,8] and inspection for corrosion on pipe networks, especially in hidden locations, such as corrosion under pipe supports [9,10].

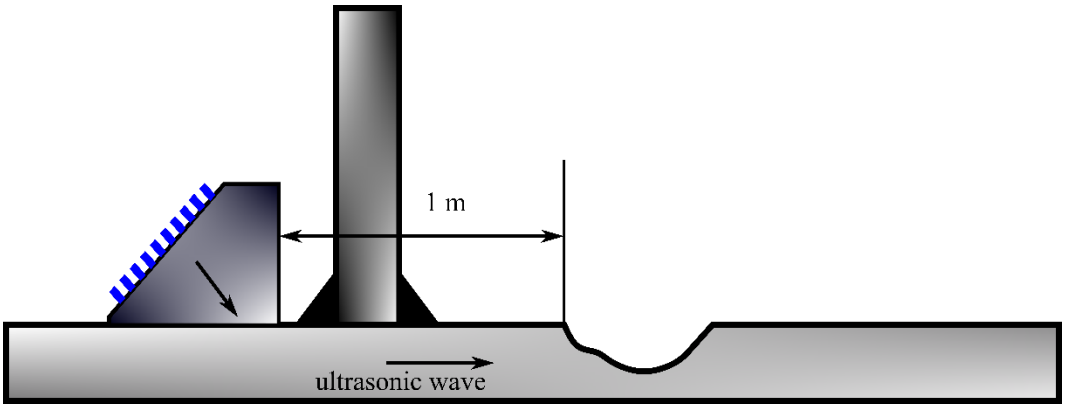

Figure 1.1. Schematic showing an example of medium-range testing at a hard to access location. The set-up is representative of the inspection of the annular plate of above-ground storage tanks while in-service.

Ongoing developments in the field on medium rang ultrasonic testing introduce new inspection techniques with the aim of increasing sensitivity and resolution, reliably detecting and quantifying wall loss, and improving sizing capabilities. A map of developed techniques is presented in Figure 1.2. Specifically, two main bulk wave-based techniques have been reported in the literature, namely the Creeping Head-wave Inspection Method (CHIME) and Multi-Skip (M-Skip) inspection methods. Guided wave related techniques are split between two classes: frequency-based and amplitude-based. The available techniques for MR-GWT are described in detail in Section 2.1.

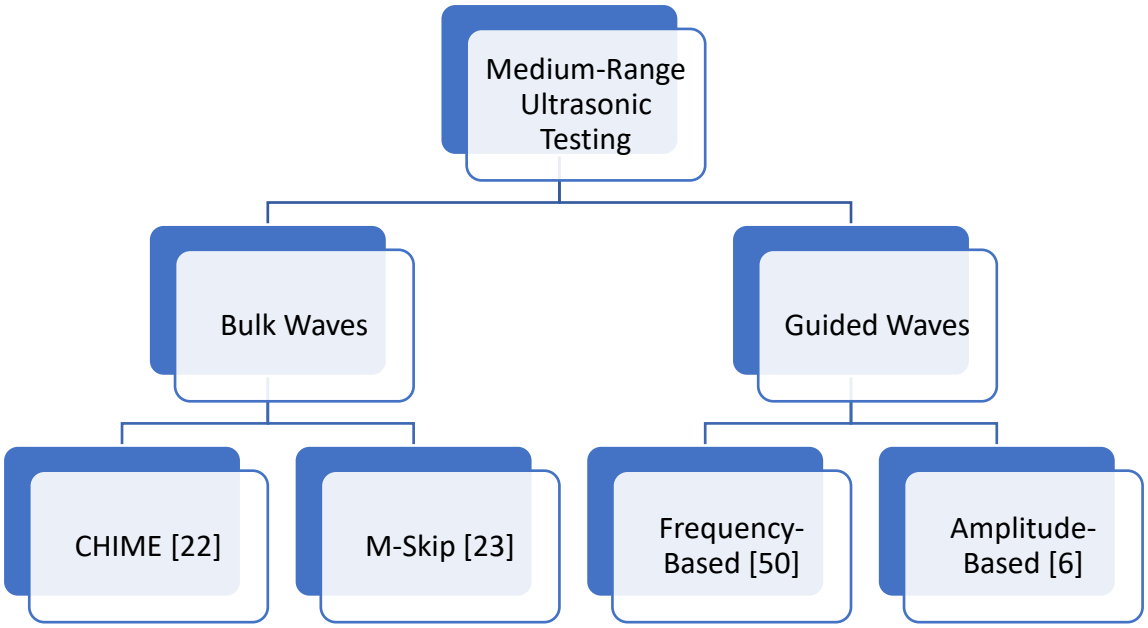

Figure 1.2. A map of medium-range testing techniques.

Problem Statement

Currently, many inspections at hard to access areas are intrusive or even impossible. For instance, examining corrosion under pipe supports necessitates lifting the pipe to remove the rust, a process typically accompanied by draining the pipe to mitigate leakage risks. Similarly, inspecting the bottom plate of above-ground storage tanks conventionally relies on Magnetic Flux Leakage, requiring the tank to be emptied and cleaned. Accessing the critical area where the annular plate welds to the lower tank shell remains cumbersome. Another example is the inspection for corrosion under insulation. Several inspection strategies may be followed, each with its advantages and limitations. For instance, precise wall thickness measurements may be performed using a network of thin sensors permanently attached to the pipe [11]. However, these can inspect only a single point. LR-GWT or pulsed eddy current (PEC) are another alternative, yet these are screening solutions. To address these problems, in this thesis, novel techniques are developed for non-destructive and non-intrusive inspection at inaccessible locations using medium-range guided wave testing.

The suitability of an inspection technique depends mainly on the nature of the defects one is looking to find. Ideally, a single inspection technique would cover all cases. Unfortunately, in the case of inspection at inaccessible locations, this is not yet realised. The morphology of corrosion defects can be categorised into two main cases: gradual wall loss corrosion with no abrupt thickness changes or when abrupt thickness changes occur, such as sharp pits. Therefore, suitable techniques must be developed, that can detect and size both types of defects.

Research Aims

The main aim of this thesis is to develop a set of techniques for the non-intrusive inspection of structural components at inaccessible locations. For this purpose, two techniques using medium-range guided waves were developed.

1. A technique capable of sizing flaws with abrupt thickness changes, such as sharp pits, at inaccessible locations using a probe 1-2 metres away from the defect area.
2. A technique to accurately quantify remaining wall thickness due to hidden local gradual wall loss corrosion.

Research Objectives

An amplitude-based technique based on Lamb waves is developed to size defects causing abrupt thickness changes, such as vertical cracks. The technique works in ‘pulse-echo’ configuration. An array probe is used, capable of dynamically emitting and receiving multiple guided waves selectively, using the principles of phased array steering. The emitted Lamb wave modes operate around 20 MHz·mm with a nominal wavelength of around 2 mm, offering high resolution and sensitivity. Note that this technique would fail to quantify smooth local corrosion, as the wave packet would be transmitted and no reflected waves would be received by the probe.

The technique can be seen as an extension of single mode Lamb wave testing in the higher order mode region, offering several advantages compared to alternative techniques. First, the technique is insensitive to defect length. This overcomes the limitation with low frequency modes, where interference phenomena complicate depth estimation. Moreover,

the through-thickness location of a defect can be estimated if, for example, it is a top or bottom surface breaking crack. Finally, using a synthetic focusing approach, it provides a way to accurately size the depth of sharp defects.

A frequency-based technique for remnant wall thickness quantification of relatively smooth corrosion patches is also developed. An SH wave is emitted, and both the reflected and transmitted waves are monitored. Specifically, mode SH1 is swept across a wide range of frequencies, from 200-500 kHz.

This is an extension of established cut-off frequency techniques based on mode SH1. In contrast to what is already available in the literature, SH1 is generated using a phased array approach. This allows rapid quantification. Moreover, it increases the frequency-wavelength range that can be covered, thus increasing the maximum wall loss depth that can be accurately quantified. The technique works well for relatively large corrosion scabs, approximately with a width of 60 mm. This means its sensitivity is similar to that of PEC. However, instead of the average, the maximum wall loss is reported.

Contribution to Knowledge

This thesis presents unique and novel contributions with direct academic and industry focused merits, related to inspection at hard to access areas. More specifically, this work has focused on the investigation and development of MR-GWT using Lamb and shear horizontal (SH) guided waves.

The following bullet points summarise the novelty and critical contributions achieved within this thesis:

- An analytical model was developed, describing forced guided wave problems.
- A set of conditions for single-mode excitation and unidirectional propagation using a linear array was derived. The number of elements, pitch value, frequency bandwidth, and apodisation profile were determined for single-mode excitation. The pitch value alone decides unidirectional propagation.
- Multiple higher order Lamb wave modes were selectively excited around 20 MHz·mm and superimposed to form a desired through-thickness energy distribution. The new energy distribution is focused on a desired depth and can be swept across the thickness of the sample. The depth of a series of surface-breaking and internal notches representing corrosion pits was accurately determined.
- Mode SH1 was excited across a wide frequency-wavelength range. The emitted wave is unidirectional. A severe 65% wall loss defect representative of uniform corrosion was accurately quantified.

Research Assumptions and Limitations

Although the material developed is applicable to a range of engineering structures, some assumptions and limitations come with this work.

First, the developed techniques assume that the component under inspection is an isotropic, linear elastic solid. These assumptions are valid for a range of structural materials, such as mild steel, carbon steel, stainless steel, and aluminium. These materials are heavily used in the power generation, offshore, and oil and gas industries. Moreover, the longitudinal

and shear wave velocities of these materials are very similar, so their dispersion curves are also similar. Therefore, although all the experiments in this thesis were conducted on an aluminium sample, the results are immediately transferable to other materials, such as mild steel. This approach is commonly adopted in the research community [12], [13].

Second, the developed techniques are applicable to plates or plate-like structures with thicknesses ranging from 1 mm up to approximately 15 mm. This makes the techniques not applicable in the case of inspecting thick plates, such as the bottom walls of above ground storage tanks, which are commonly thicker than 20 mm. Nevertheless, a lot of engineering components fall within the specified thickness range. Specifically, the thickness of the annular plate of above ground storage tanks, which are usually used in the oil and gas sector, is typically 10 mm [6]. In fact, all experiments in this work were conducted on a 10 mm thick plate. Moreover, a large number of operating pipelines with varying nominal pipe sizes and schedule numbers have thicknesses in the 1mm - 15 mm range [14]–[16].

Thesis Structure

Chapter 2 discusses existing MR-GWT and related techniques for inspection at inaccessible locations. Furthermore, theoretical material for guided wave propagation in plate structures under forced motion is presented. No specific conditions on the force load were made, and transient loads were studied. Based on these results, guided wave excitation using linear arrays is studied in later Chapters.

The excitation of a single Lamb wave mode at high-frequency thickness products, around 20 MHz·mm, is examined in Chapter 3. Using the analytical model derived in Chapter 2, the influence of key parameters such as element width, number of elements, pitch, and temporal excitation profile is determined, and a set of conditions related to the targeted mode's unidirectionality and purity is derived. Experimental results validate the derived conditions using a dataset acquired with the Full Matrix Capture (FMC) method. Chapter 4 presents a novel imaging technique, termed Lamb wave focusing. An array probe emits dynamically multiple Lamb wave modes (one at a time) in the higher order mode region. The modes are superimposed synthetically to focus the energy at a desired depth. The focus depth can be varied. This way, focusing throughout the thickness of the plate is achieved. The technique is tested on a series of notches in simulations and experiments.

In Chapter 5, mode SH1 is generated over a wide frequency-wavelength range. An electromagnetic acoustic transducer (EMAT) array is utilised, and its elements are appropriately phased to target mode SH1 using beam steering. The array is modelled as a shear horizontal load, and the effect of key parameters on excitation is determined. The results are compared with those obtained in the case of Lamb wave generation (see Section 3.3). Simulations and experiments validate the ability of the array to generate mode SH1 in the desired frequency-wavelength range. Chapter 6 is concerned with the usage of the EMAT array to determine the maximum wall loss of relatively uniform corrosion defects. The minimum remaining wall thickness of a simulated smooth wall thinning defect is quantified. Experimental results on a corrosion-like defect validate the approach. Finally, in Chapter 8, key conclusions are drawn.

Lead Author Publications Arising From This Thesis

K. Tzaferis, M. Tabatabaeipour, G. Dobie, S. G. Pierce, D. Lines, C. MacLeod and A. Gachagan, “Dual Mode Inspection Using Guided Waves and Phased Array Ultrasonics from a Single Transducer,” 2023, pp. 79–88. doi: 10.1007/978-3-031-07322-9_9, 10th European Workshop on Structural Health Monitoring.

K. Tzaferis, M. Tabatabaeipour, G. Dobie, D. Lines, and C. N. MacLeod, “Single-mode Lamb wave excitation at high-frequency-thickness products using a conventional linear array transducer,” *Ultrasonics*, p. 106917, Dec. 2022, doi: 10.1016/j.ultras.2022.106917.

K. Tzaferis, M. Tabatabaeipour, R. McMillan, G. Dobie, and A. Gachagan, “A shear horizontal phased array steering excitation technique for remnant wall thickness quantification,” *Ultrasonics*, vol. 136, no. August 2023, p. 107142, 2024, doi: 10.1016/j.ultras.2023.107142.

K. Tzaferis, M. Tabatabaeipour, G. Dobie, G. Pierce, M. Papaelias C. MacLeod and A. Gachagan., “The effect of complex corrosion profiles on remaining wall thickness quantification using shear horizontal guided waves,” 14th International Workshop on Structural Health Monitoring - Stanford University, California, United States.

K. Tzaferis, G. Dobie, D. Lines and C. MacLeod, “A technique for medium-range through-thickness focusing using Lamb waves”, NDT&E International, accepted for publication.

Co-Author Publications Arising From This Thesis

R. McMillan, R. Hampson, M. Tabatabaeipour, W. Jackson, D. Zhang, K. Tzaferis and G. Dobie, “Design and Manufacture of an Optimised Side-Shifted PPM EMAT Array for Use in Mobile Robotic Localisation,” *Sensors (Basel).*, vol. 23, no. 4, 2023, doi: 10.3390/s23042012.

G. D. Adam Gilmour, M. Tabatabaeipour, R. McMillan, K. Tzaferis, R. Hampson, W. Jackson, D. Zhang, A. Lawley, A. Mohamed, C. MacLeod, A. Gachagan and G. Pierce, “Robotic ultrasonic inspection of large and complex structural assets,” in *Structural Health Monitoring 2023*, 2023, pp. 2143–2150.

A. G. Ross McMillan, M. Tabatabaeipour, K. Tzaferis, W. Jackson, R. Edwards, O. Trushkevych, C. Macleod and G. Dobie, “Crawler-based automated non-contact ultrasonic inspection of large structural assets,” 2022.

Chapter 2

Background and Theoretical Framework

This Chapter presents background material on guided wave testing at inaccessible locations. Moreover, the theoretical basis for understanding the propagation of ultrasonic waves in solid media is covered. Specifically, in Section 2.1, a literature review on available techniques for inspection at hard to access areas is provided. Section 2.2 covers the underlying theory for wave propagation under forced motion. First, a review of bulk waves in a linear elastic solid is briefly presented. Then, ultrasonic waves in plate or plate-like structures are discussed. Boundary conditions are introduced, leading to guided wave solutions. Finally, analytic solutions for forced guided wave problems are studied. A new solution method is presented based on modal analysis. The procedure is simple and can be applied to a range of forced problems in acoustics. The material presented in Section 2.2.3 is employed in Chapters 3 and 4.

2.1. Research Background

2.1.1. Guided waves in plates and plate-like structures

Ultrasonic guided waves are sound waves that propagate through a structure, such as a plate or pipe, guided by its geometric boundaries. These waves can travel long distances along the structure. Their exact range depends mainly on their frequency bandwidth, material attenuation, the general condition of the structure, and the presence of liquids or coatings. Guided waves distribute energy throughout the thickness of the structure; thus, the entire thickness is interrogated. They are extensively used in NDT in industries such as oil and gas, aerospace, and nuclear.

This thesis focuses on the study of guided waves in plate or plate-like structures. A plate is characterised as a solid rectangular parallelepiped body with a thickness significantly less than its length and width. A plate-like structure is one that exhibits behaviour akin to a plate. For example, circumferential waves in a thin wall pipe can be approximated as a plate guided waves, provided the ratio between the inner (r_{in}) and outer radius (r_{out}) is $\frac{r_{in}}{r_{out}} > 0.95$ [12]. Throughout this thesis, the term "plate" is used for both traditional flat plates and structures resembling them. For plates with traction-free top and bottom surfaces, two distinct types of guided waves occur: Lamb waves and SH waves.

2.1.1.1. Lamb waves

Lamb waves represent elastic waves with particle vibrations occurring in the direction of propagation and the shear vertical direction [13–16]. They can be decomposed into symmetric and antisymmetric modes. Symmetric modes have symmetric compressional

and antisymmetric shear vertical through thickness displacement components. Conversely, in antisymmetric modes, the wave structure across the thickness is symmetric for the shear vertical and antisymmetric for the compressional component. The fundamental antisymmetric and symmetric modes, termed A0 and S0, respectively, exist at all frequency-thickness products. At low frequencies, the former is a flexural (bending) wave, whereas the latter is almost purely compressive. Therefore, the phase velocity of mode S0 is similar to the compressional speed of sound of the material, making it faster compared to mode A0.

The properties of Lamb wave modes, such as phase velocity, dispersion, and modal density, depend on the frequency-thickness product. The dispersion curves for an aluminium plate are shown in Figure 2.1. In the low regime, below ∼1.5 MHz·mm, the fundamental modes are well separated, and higher order modes cannot propagate. Modes A0 and S0 combine and form the Rayleigh wave for frequency-thickness products above ∼5 MHz·mm. In this thesis, emphasis is placed on the region above 15 MHz·mm, referred to as the higher-order mode region. Within this region, the first few higher order modes exhibit little dispersion and have low wavelength. Nevertheless, these modes are closely spaced, posing a challenge to achieving single-mode excitation, although it remains feasible. The utilisation of these modes for NDT presents a distinctive advantage, as it enhances sensitivity and resolution, thereby elevating the overall effectiveness of the inspection process.

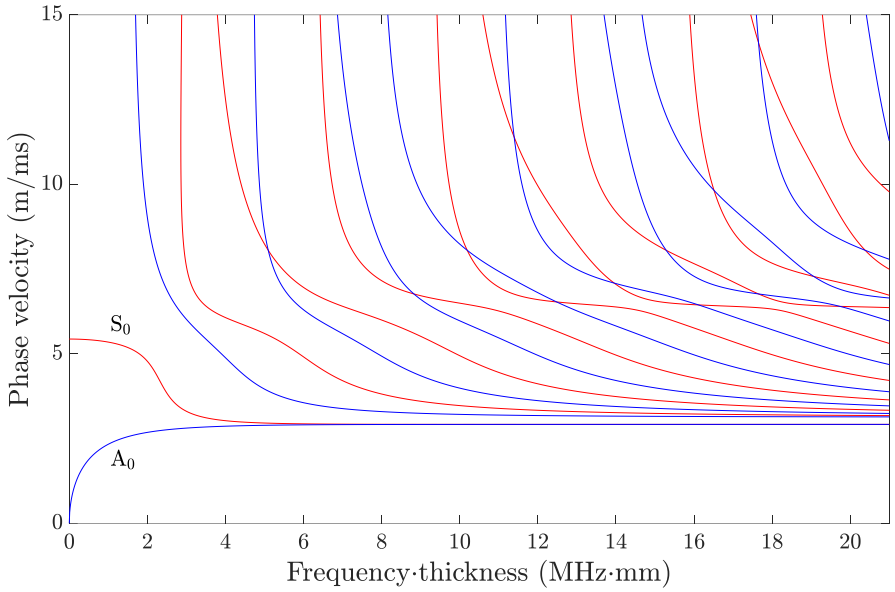

Figure 2.1. Frequency-thickness product vs phase velocity Lamb wave dispersion curves for an aluminium plate

2.1.1.2. Shear horizontal waves

SH waves are travelling waves characterised by oscillations exclusively in the shear horizontal direction concerning the propagation direction [13]. For this reason, their properties are independent of the compressional velocity. SH waves exhibit modes that can be classified into symmetric and antisymmetric categories. Notably, the fundamental mode of SH0 stands out as the sole mode (including Lamb waves) with a uniform energy distribution throughout the plate thickness. Its speed is independent of the frequency-thickness product, as shown in Figure 2.2. This means SH0 is non-dispersive. There is no fundamental antisymmetric mode. The first antisymmetric mode is SH1, which exists approximately above 1.5 MHz·mm. Its displacement maximises at the top and bottom surfaces of the plate and tends to zero as it approaches the plate's middle surface. In

contrast to Lamb waves, which require a numerical solution for the calculation of the dispersion curves, closed-form expressions exist describing SH mode curves.

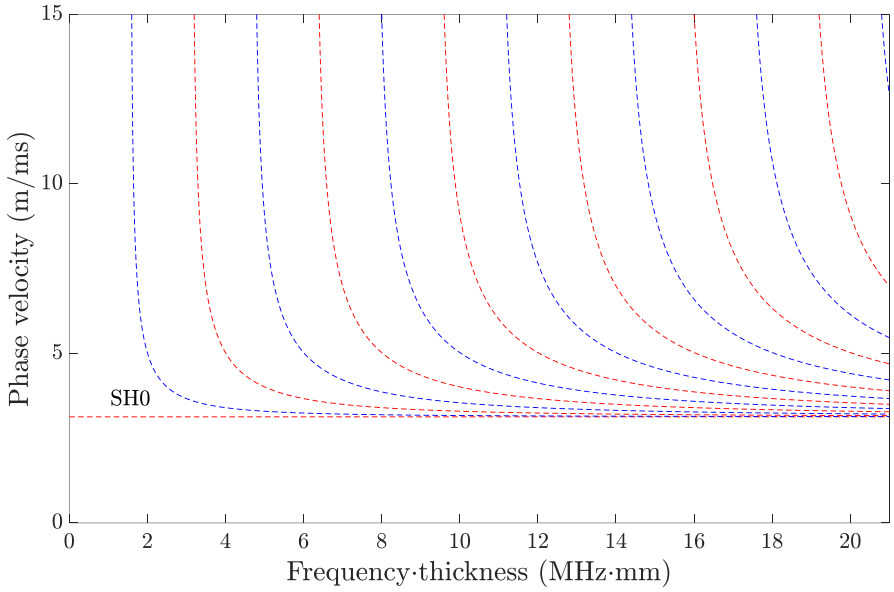

Figure 2.2. Frequency-thickness vs phase velocity product SH wave dispersion curves for an aluminium plate

2.1.2. Long-range guided wave testing (LR-GWT)

LR-GWT is a screening technique used to inspect structures over extended distances. The technique is particularly useful for the inspection of pipework, such as pipe racks and transmission lines [17–21]. Common practice is to mount a ring of transducers around the pipe and generate a low frequency torsional wave travelling in the axial direction. The emitted wave can propagate for many metres along the length of a structure (typically around $30 - 100$ m). Upon interaction with a pipe feature (weld, support) or defect, a signal is reflected and received by the same ring. By analysing the reflected waves, defects such as corrosion, erosion, and other anomalies can be identified. Defect severity is determined mainly by the signal's amplitude, shape, and energy leakage to flexural modes.

Potential problem areas are further investigated using a more precise method to determine the exact dimensions of the defect.

This approach is valuable for continuous monitoring and maintenance planning, offering a cost-effective and efficient solution for industries such as oil and gas, where the integrity of long-distance pipelines is crucial for operational safety and reliability. It allows inspection of buried pipes and corrosion under insulation without the need for extensive excavation or numerous access points.

The main limitation of the technique is its low sensitivity to small defects. For this reason, in cases where finer defect detection is required, alternative inspection techniques must be employed.

2.1.3. Medium-range guided wave testing (MR-GWT)

MR-GWT covers a range of a NDT techniques that utilise ultrasonic waves to inspect structures over intermediate distances, offering a balance between the coverage of LR-GWT and the precision of traditional ultrasonic testing. MR-GWT is advantageous in scenarios where access may be limited or inspection speed is critical. These include corrosion under pipe supports, in-service inspection of the annular plate of above-ground storage tanks, in-process weld inspection of relatively thin plates, or rapid inspection of large plates, such as tank shells or pressure vessels. Corrosion under insulation can also be addressed by permanently installing a probe under the insulation. MR-GWT provides a cost-effective and efficient solution for industries where continuous monitoring of structural integrity is essential, enabling timely maintenance interventions and

contributing to the overall reliability and safety of critical infrastructure. Over the previous years, several medium-range guided wave and related inspection techniques have been developed:

- CHIME
- M-Skip
- Amplitude based guided wave testing
- Frequency based guided wave testing

In what follows, each technique is discussed in detail.

2.1.3.1. CHIME

CHIME is a screening method for the inspection of plates or pipes whose outer/inner ratio does not exceed a value of 1.19 [22]. The technique utilises single-element transducers positioned on the opposite sides of an obstacle. Ultrasonic waves are emitted at the critical angle to produce a creeping wave propagating along the surface of the component. The first creeping wave generates a head wave, and the head wave generates in turn a secondary creeping wave at the opposite boundary. The head wave travels as a plane wavefront at the critical shear wave angle. This way, the full volume between the two probes is covered. Due to beam spreading, bulk waves are also generated below or above the critical angle. The received signal consists of a series of peaks including all the propagating wave modes. As acoustic waves propagate through the material, the differences in amplitude and arrival times of these wave patterns are analysed to identify defects or irregularities within the structure. Ravenscroft et al. demonstrated the ability of

the technique to detect a series of corrosion pits (with a minimum surface diameter of 11 mm) and generally corroded areas. Similar results were reported in [23]. Defect severity may be estimated by ranking the signals into three corrosion categories: $< 10\%, 10 - 35\%$ and $> 35\%$ [24,25].

2.1.3.2. M-skip

M-Skip is an ultrasonic technique used to quantify the average wall loss between a pair of piezoelectric transducers [23]. The probes are positioned on the opposite sides of an obstacle. The transmitter is mounted on an angled wedge and emits shear waves that reflect between the structure's boundaries and are received on the opposite side by an identical probe without converting to compressional waves. The number of skips depends on the thickness of the structure and the separation distance. Wall loss is estimated using the time of arrival of a series of skip signals. The technique has been tested both in laboratory and industrial environments. Burch et al. [23] tested its performance against several machined defects representative of corrosion as well as on a naturally corroded pipe. Average wall loss was successfully quantified along the line of sight between the probes; however, pitting was not detectable. Further on-site trials were conducted by Shell in partnership with Sonomatic [25]. Specifically, a M-skip scanner was developed and used for wall loss quantification at clamped saddle support locations. The technique showed good sensitivity to local wall loss. However, in the presence of attenuative coatings or rough surfaces, the signal is significantly distorted, and wall loss detection and quantification become difficult. Recently, an expansion of M-skip has been implemented, utilising phased array probes [26][27]. This is advantageous, as different beam angles are

sensitive to different pipe geometries and corrosion morphologies, resulting in some beam angles being more effective than others in arriving at the receiver.

2.1.3.3. Amplitude based guided wave testing

Most commonly, detection and severity estimation of an indication depend on signal amplitude. Additional features, such as phase or time of flight, have been used by researchers to detect or size imperfections. To reduce mode conversion effects and simplify signal interpretation, commonly, a single guided wave mode is targeted [28]. Depending on the inspection requirements, such as inspection range, defect morphology, and location, a specific mode is chosen.

Single mode inspection below 15 MHz·mm

The region below 15 MHz·mm has been investigated by several authors, particularly for steel and aluminium samples, utilising both Lamb [29–35] and SH waves [36–40].

Below 5 MHz·mm

Lowe et al. performed a detailed study on the reflection coefficient of mode S0 around 1.5 MHz·mm using a series of notches of varying depth and width [31]. It was shown that depending on the width, the echoes from the two sides of the notch interfere constructively or destructively, affecting the reflection amplitude. A monotonic relationship between notch depth and reflection coefficient was observed. Nevertheless, the relationship between notch width with the reflection coefficient is not monotonic, making sizing difficult. Jenot et al. used mode S0 to quantify wall loss in a corroded region [32]. Using

time of flight measurements, variations in group velocity and wall thickness were deducted. The technique was successful for smooth and shallow corrosion profiles.

Clough and co-workers developed a screening system for rapid pipe inspection [38]. The system operates in pitch-catch, generating and receiving modes SH0 and SH1 that travel in the circumferential direction, approximately at 3 MHz·mm. The presence of a defect is indicated by the amplitude drop and time of flight of the transmitted signal. Corrosion defects could be identified by comparison with an intact reference signal, yet wall loss quantification was not possible. A similar configuration has also been reported in [39]. Specifically, Andruschak et al. generated SH1 in a dispersive region to detect wall thinning defects under pipe supports. The generated wavepacket was found to be sensitive to corrosion patches but insensitive to supports. The amplitude of the transmitted signal, time of flight, and beam spreading were used to detect defects. Hirao and Ogi proposed an alternative technique for pipe thickness inspection [37]. A single probe is used to emit and receive SH waves. Modes SH0 and SH1 were selectively excited at 2.3 and 2.8 MHz·mm, respectively. The technique was tested against machined dish-shaped and flat-bottom rectangular defects on a steel pipe. The authors claim that by measuring the amplitude and phase values of SH0 and SH1, a procedure for determining wall loss can be established.

Between 5-10 MHz·mm

Cirtautas and co-workers [41] demonstrated the feasibility of generating the symmetric mode S3 on a 10 mm sample with a linear 1 MHz array mounted on an angled wedge using a two-sided excitation approach. The interaction of S3 with corrosion-like defects

was simulated, showing the potential of the mode for corrosion defect detection and classification. In a follow-up paper, Cirtautas et al. studied the interaction of S3 and other higher order modes with corrosion defects in more detail [42]. A method was proposed, termed phase velocity mapping, to be used as input to train a neural network. The current models detected corrosion with high accuracy but were unable to quantify maximum wall loss.

Single mode inspection above 15 MHz·mm

Recently, there has been a research interest in the inspection at high frequency-thickness products, above 15 MHz·mm [6–9,43–47].

Balasubramaniam et al. pioneered a technique they call Higher Order Mode Cluster (HOMC). The technique has been researched for use in the inspection of the critical zone in the annular plate of storage tanks [6], corrosion under pipe supports [9,44] and the heat-affected zone during pipe welding [48]. A monolithic piezoelectric transducer is mounted on a wedge to emit ultrasonic waves at an angle. Both ‘pulse-echo’ and ‘pitch-catch’ configurations are attainable. A broadband excitation toneburst is used, and it is claimed that multiple higher order modes propagate in the sample. These modes have very similar group velocities and propagate as a single wavepacket for the range of interest. Defect detection and sizing are performed based on the amplitude of the reflected signal. In a related study, Khalili and Cawley showed the properties of the mode cluster are essentially those of mode A1 [43].

2.1.3.4. Frequency based guided wave testing

Apart from amplitude-based methods, researchers have used frequency-based techniques to quantify defects. These techniques are suitable for the minimum remaining wall thickness estimation of gradual wall thinning defects.

Lamb waves

Higher-order Lamb wave modes have been effectively applied for defect quantification. Early studies focused on tracking the presence or absence of specific wave modes, utilising their cut-off frequency property, to estimate wall loss [49,50]. Another frequency-based property investigated by the research community is the so called frequency compensation concept [50–52]. This concept relies on the increase in frequency of a mode when propagating through a wall thinning region to maintain a constant frequency-thickness product. Zhu et al. [51] estimated wall loss using simulations and experiments using two probes across the defect region. Accurate results were obtained. However, the probes were located inside the wall thinning region, limiting the technique to cases where this is possible.

More recently, Cao et al. [53] detected envelope variations of mode A1 at a frequency slightly above its cut-off. A metric called ‘envelope difference coefficient’ was derived (EDM). Although EDM was found to increase with an increase in width and depth, ensuring detection of corrosion, its complex relationship with corrosion morphology complicates wall loss quantification. Suresh and Balasubramaniam [54] used a linear transducer array to monitor the reflection of A1 mode on a 1 mm thick aluminium plate. By activating different groups of elements, mode A1 is excited at four different frequency-

thickness products. The approach was tested against a series of machined dish-shaped defects. Wall loss was estimated within a thickness range. Moreover, another series of experiments was conducted, where the elements of the array were activated with a varying pitch to excite a range of wavelengths from 3.8 to 5.56 mm. Wall loss was estimated with a maximum error of 2.3%.

SH waves

Recently, the cut-off properties of SH modes have been investigated for remnant wall thickness estimation [55–58]. Belanger used multiple higher order SH modes simultaneously to estimate wall loss between a source and a sensor [55]. However, experimental results show a 20% underestimation of wall loss for a 30% wall thinning area. It was suggested that surface roughness may be the reason for this mismatch.

An alternative approach, which has shown promise, is to excite a single higher order mode across a wide frequency range [59–61]. The technique uses a pair of transducers placed before and after the corrosion scab. Both the reflected and transmitted waves are monitored. The wall thinning regions act as a frequency filter, allowing only frequencies above the cut-off to pass, whereas lower frequencies are reflected. To reduce mode conversion, mode SH1 is excited with a periodic permanent magnet (PPM) EMAT. The conventional PPM EMAT is a mature probe used to emit and receive SH waves [62]. These waves exhibit a specific wavelength, which is determined by magnet spacing. Therefore, this transducer is incapable of sweeping across a wide range of wavelengths. To compensate for this matter, two different approaches have been reported in the literature. The first involves a built-in mechanism that adjusts the spacing between magnet

rows [59,60,63]. For a given frequency, the spacing is selected to match the wavelength of the targeted mode. Although robust and straightforward, physically changing the distance of the magnets can be time-consuming. Moreover, the system can quantify up to 50% wall loss. The second approach involves the design of a novel broadband transducer [61]. The spacing between the magnet rows varies to cover a range of selected wavelengths. A temporal excitation that spans the required frequencies is selected. This is accomplished with only one capture, allowing for rapid data acquisition. The designed transducer can quantify wall loss between $30\% - 50\%$. Covering a larger range of wall loss requires larger probes, which may not be practical in some scenarios.

2.1.4. PEC

An alternative to ultrasonic-based techniques applicable in the case of inspection for corrosion under insulation is pulsed eddy current testing. PEC is designed to assess corrosion in ferromagnetic structures such as carbon steel and cast iron. It is commonly used for inspection of corrosion under insulation and corrosion scab and blister assessment. The method works without the need to remove insulation (if less than 100 mm) or prepare rough or dirty surfaces. A pulsed magnetic field is induced into the material using a coil. As this magnetic field interacts with the conductive material, it generates eddy currents. These eddy currents are sensed by the probe. Their characteristics depend on the material properties and thickness of the sample. The received electromagnetic signals are compared with reference signals from known calibration blocks, and this way are related to the thickness of the component. PEC is practical and provides quantitative results on corrosion. However, instead of quantifying the maximum wall loss, PEC determines the

average wall loss with the footprint area. These two values are close when general wall loss defects are examined; as corrosion morphology becomes more irregular, their difference is significant. This means the method offers limited sensitivity and resolution. For instance, inspecting a 50% deep defect from a 50 mm lift off, the minimum detectable defect diameter is approximately 58 mm.

2.2. Theory

Understanding ultrasonic wave propagation is essential for NDT. Depending on the dimensions of the material and the wavelength bandwidth, a linear elastic solid can be modelled as finite, infinite, or semi-infinite. In the first case, the boundary conditions determine the mode shapes of the solid. These are essentially standing waves that oscillate at the mode's eigenfrequency. If the wavelength is significantly lower compared to the dimensions of the body, it may be treated as infinite. In this case, it is convenient to express the fundamental solutions as a travelling wave. These travelling waves depend only on material properties and not on boundary conditions; thus, they are called bulk waves. The third case includes bodies that have one dimension significantly larger compared to the others. In this case, a body is modelled as finite in the thin direction and infinite in the directions that are large compared to the wavelength. These waves are termed guided waves and are a combination of a standing and a travelling wave along the thin and large directions, respectively. For the purposes of NDT, bulk and guided waves are the most interesting.

2.2.1. Bulk waves

Assume a linear elastic solid. A right-handed frame (x_1, x_2, x_3) is located at the centre of the body. The equations of motion appear in the following form [13],

$$\rho \ddot{u}^i = \sigma_{ik,k} + F_i, \tag{2.1}$$

where ρ is the material density, u^i is the displacement vector, F_i denotes the external force per unit volume and σ_{ik} is the stress tensor. Lower case Latin indexes i, j, k, l vary in the range 1,2,3 and the summation convention for repeated indices is adopted [64]. The generalised Hooke's law is assumed,

$$\sigma_{ik} = C_{iklj} \epsilon_{lj},$$

where ϵ_{ij} is the strain tensor and C_{iklj} is the four-rank elasticity tensor.

Next, let's assume a time harmonic solution of the form

$$u^i = \mathrm{Re}\left\{ a_i \exp\left(i\left(k_j x_j - \omega t \right) \right) \right\} \tag{2.2}$$

where a_i is the amplitude vector, k_j is the wavevector, ω is the angular frequency, and t represents time. Plugging equation (2.2) into (2.1) and in the absence of external forces one gets

$$-\rho \omega^2 u^i = -C_{iklj} k_k k_l u^j.$$

After algebraic manipulations, it can be shown that

$$\left(\rho \omega^2 \delta_{ij} - C_{iklj} k_k k_l \right) u^j = 0$$

where δ_{im} is the Kronecker delta. Setting $k_k = kn_k$, where k is the wavenumber and n_k is a unit vector and using $c^2 = \frac{\omega^2}{k^2}$, the above expression becomes

$$\left(\Gamma_{ij} - \rho c^2 \delta_{ij}\right) a_j = 0,$$

where $\Gamma_{ij} = C_{iklj} n_k n_l$, and in matrix form

$$(\Gamma - \rho c^2\ I)\ \underline{a} = \underline{0}. \tag{2.3}$$

To obtain non-trivial solutions, it is required that

$$\det\left(\Gamma - \rho c^2 I\right) = 0 \tag{2.4}$$

Matrix Γ depends on the material properties and selection of vector $\underline{n}$. In the case of an isotropic solid, the elasticity tensor has only 2 independent components [13]. Equation (2.4) reads

$$\left(\rho c^2 - \lambda_L - 2\mu_L\right)\left(2\rho c^2 - 2\mu_L\right) = 0,$$

where λ_L and μ_L are Lame's constants. Two velocities satisfy equation (2.4), namely the longitudinal and shear wave velocity,

$$c_L^{\ 2} = \frac{\lambda_L + 2\mu_L}{\rho} \text{ and } c_T^{\ 2} = \frac{\mu_L}{\rho},$$

respectively. Note that although the vector $\underline{n}$ was kept arbitrary in the analysis, the velocities do not depend on $\underline{n}$. This means that the speed of sound is independent of the direction of propagation. For $c = c_L$, equation (2.3) is satisfied when $a_k = n_k$. Therefore,

the body's particles are oscillating in the direction of wave propagation, and the motion is compressional. For $c = c_T$, all vectors $\underline{a}$ that satisfy $\underline{a} \cdot \underline{n} = \underline{0}$ are admissible. The particles oscillate perpendicular to the direction of propagation, exhibiting shear motion.

2.2.2. Guided waves in plates and plate-like structures

Consider a homogeneous isotropic plate of length ℓ, width b and thickness $d = 2h$, as shown in Figure 2.3. A frame $(\mathrm{x}_1 = \mathrm{x}, \mathrm{x}_2 = \mathrm{y}, \mathrm{x}_3 = \mathrm{z})$ is located at the centre of the plate. If the thickness of the plate is comparable to the wavelength of the propagating waves, interference [65] phenomena occur and standing waves form in the z-direction. Satisfaction of the boundary conditions at the top and bottom surfaces of the plate leads to guided wave solutions. These are travelling waves in the x-y plane but standing waves in the z-direction.

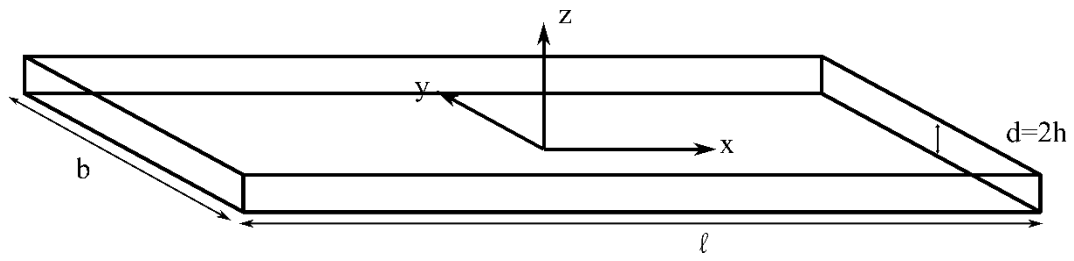

Figure 2.3. Schematic of a plate structure

Assume a wave solution of the form,

$$u^j = Re\left\{a_j \exp\left(ik\left(x + l_z z\right) - i\omega t\right)\right\}, \tag{2.5}$$

where the wavevector is given by

$$\underline{k} = k\left(1, 0, l_z\right)^T. \tag{2.6}$$

Equation (2.6) states that the direction of propagation lies in the x-z plane. This implies that travelling waves are generated by a source load extending sufficiently along the y-direction. In the transduction mechanisms employed in this work, the width of the source excitation is multiple times the wavelength, thus condition (2.6) is valid. Plugging (2.5) into (2.4) and using equation (2.6), a sixth order algebraic equation on l_z is obtained. Each solution represents a longitudinal, in-plane (x-z plane) shear or shear horizontal wave travelling towards the top or bottom surface. Taking a linear combination of the six partial waves yields

$$u^j = Re\left\{\sum_{J=1}^{6} C_J a_j^{(J)} exp\left(ik\left(x + l_z^{(J)} z\right) - \omega\, t\right)\right\}. \tag{2.7}$$

Next, boundary conditions are employed. Specifically, the plate is traction-free at the top and bottom surfaces,

$$T_i = \sigma_{ij} n_j = 0, \tag{2.8}$$

where $\underline{n} = (0,0,1)^T$. Inserting (2.7) into (2.8) yields a systems of six homogenous linear equations with respect to C_J. Arranging the equations in matrix form and requiring the determinant to be zero to obtain non-trivial solutions yields the so-called dispersion equations,

$$\frac{\tan\left(\bar{q}h\right)}{\tan\left(\bar{p}h\right)} = -\frac{4k^2\bar{p}\bar{q}}{\left(\bar{q}^2-\bar{k}^2\right)^2}, \text{ for symmetric Lamb wave modes}$$

$$\frac{\tan\left(\bar{q}h\right)}{\tan\left(\bar{p}h\right)} = -\frac{\left(\bar{q}^2-\bar{k}^2\right)^2}{4k^2\bar{p}\bar{q}}, \text{ for antisymmetric Lamb wave modes}$$

$$\left(\frac{a\pi}{2h}\right)^2 = \frac{\omega^2}{c_T^2} - k^2,\ a = 0,1,\ldots,\infty, \text{ for shear horizontal modes}$$

Where $\bar{p}^2 + k^2 = \omega^2 / c_L^2$ and $\bar{q}^2 + k^2 = \omega^2 / c_T^2$. For an admissible solution (ω, k), the coefficients C_J determine the contribution of each partial wave to a guided wave mode. The displacement field can then be expressed as $\underline{u} = \underline{X}\exp(-i\omega t)$, where $\underline{X}$ denotes a guided wave mode.

Lamb wave modes are formed by combining four partial waves, namely the longitudinal and in-plane shear. After summation of the partial waves, the displacement field of the Lamb wave modes appears in the form

$$\begin{aligned} X^1 &= X^1(z)\exp(ikx) \\ X^2 &= 0 \\ X^3 &= X^3(z)\exp(ikx) \end{aligned} \tag{2.9}$$

where $X^1(z)$, $X^3(z)$ are provided in Appendix A. In the x-direction, a time-harmonic Lamb wave propagates with phase velocity $c_p = \omega/k$. Its wavelength is determined by $\lambda = 2\pi/k$. In the thickness direction, superposition of the partial waves yields a standing wave. It's through-thickness profile depends on the specific mode and frequency examined.

The shear horizontal partial waves construct the so-called SH wave modes, given by

$$X^1 = 0$$
$$X^2 = \begin{cases} \cos\left(a\pi z/d\right)\exp(ikx), & \text{a} = 0,2,4,... \\ \sin\left(a\pi z/d\right)\exp(ikx), & \text{a} = 1,3,5,... \end{cases} \tag{2.10}$$
$$X^3 = 0$$

In contrast to Lamb waves, closed form expressions exist for their modal properties. For instance, the phase velocity of mode n is given by $c_p = 2c_T \dfrac{fd}{\sqrt{4\left(fd\right)^2 - n^2 c_T^2}}$, where $f = 2\pi/\omega$ is the frequency of the mode.

2.2.3. Forced motions of a plate

Forced guided wave problems are commonly solved using a suitable analytical method. Among others, the normal mode expansion method [66,67] and methods based on integral transforms, such as the Fourier transform [13] are commonly utilised. This work presents an alternative technique to obtain an analytic solution of wave motion under a general loading force. Specifically, the plate is treated as a finite body, and tools from modal analysis are applicable. The method is straightforward and intuitive. Furthermore, there is no need to define new concepts, such as a new orthogonality condition [66]. Throughout the analysis, all quantities remain finite. A drawback of the method is that solutions are naturally expressed in terms of vibration modes (standing waves) rather than travelling waves. However, a standing wave can be expressed as the sum of two travelling waves [15]. After the final solution is derived, the limit as $\ell \to \infty$ is obtained.

Consider the plate shown in Figure 2.3. Forcing terms are considered to extend sufficiently along the y-direction, thus, effectively, the dynamics are fully captured by studying a 2D layer of the plate in the x-z plane. Ultrasonic waves are assumed to propagate far from the left and right boundaries; thus, a particular choice of boundary conditions does not affect wave propagation. Therefore, the boundary conditions at the left and right edges can be arbitrarily chosen. In fact, any complete set of functions in $L^2\left(\left[-\frac{\ell}{2},\frac{\ell}{2}\right]\to\mathbb{C}\right)$ can be selected. In this work, the set

$$\left\{\exp(ik_n\ x),\ k_n=2\pi\ n/\ell,\ n=0,1,2,\ldots\right\}$$

is employed. Note that as $\ell\to\infty$, k becomes a continuous variable.

A guided wave mode is defined by a point in the angular frequency-wavenumber domain, (ω_p,k_n), where indices p,n vary from zero to infinity. To keep the notation simple, the pair (p,n) is mapped to a single index, say m, using the following bijection map

$$(p,n)\to(p+n)(p+n+1)/2+n=m.$$

This way, a guided wave mode $\underline{X}_m$ is denoted by a single index m. Since the modes form a complete basis, the displacement field can be expanded into an infinite series form,

$$\underline{u}=Re\left\{\sum_{m=0}^{\infty}\tau^m\ \underline{\hat{X}}_m\right\},\tag{2.11}$$

where $\underline{\hat{X}}_m$ is the m^{th} normalised mode, $\underline{\hat{X}}_m=\frac{1}{g_{mm}}\underline{X}_m$. The components of the metric tensor are given by

$$g_{mn}\left(\underline{X}_m,\underline{X}_n\right)=\int_V \rho\underline{X}_m\cdot\underline{X}_n^* dV=\rho b\ell\int_{-h}^{h}\underline{X}_m(z)\cdot\underline{X}_n^*(z)dz=\ell\overline{g}_{mn}, \tag{2.12}$$

where $\left(\ \right)^*$ denotes the conjugate operator.

According to modal analysis [68,69], the time coefficients τ^m satisfy the second order differential equation

$$\ddot{\tau}^m+\omega_p^2\tau^m=\hat{f}_m^*\left(t\right),$$

where $\hat{f}_m^*\left(t\right)=\dfrac{1}{\sqrt{g_{mm}}}f_m^*\left(t\right)$ and $f_m^*\left(t\right)$ is the projection of the external force on the conjugate of the m^{th} mode,

$$f_m^*\left(t\right)=\int_V\underline{F}\left(x,z,t\right)dV\cdot\underline{X}_m^*\left(x,z\right). \tag{2.13}$$

Assuming zero initial conditions, the solution can be obtained according to Duhamel's integral,

$$\begin{aligned}\tau^m(t)&=\frac{1}{\omega_p}\int_0^t\hat{f}_m^*\left(\tau\right)\sin(\omega_p(t-\tau))d\tau\\&=\frac{1}{\omega_p}\frac{1}{\sqrt{g_{mm}}}\left(A^*(t,\omega_p)\sin(\omega_p t)-B^*(t,\omega_p)\cos(\omega_p t)\right)\\&=\frac{1}{2\omega_p}\frac{1}{\sqrt{g_{mm}}}\left(\left(\left(A_I-B_R\right)+i\left(A_R+B_I\right)\right)\exp(-i\omega_p t)-\left(\left(B_R+A_I\right)+i\left(A_R-B_I\right)\right)\exp(i\omega_p t)\right),\end{aligned}$$

where

$$A_R = \mathrm{Re}\left\{\int_0^t f_m^*(\tau)\cos(\omega_p\tau)d\tau\right\},\ A_I = \mathrm{Im}\left\{\int_0^t f_m^*(\tau)\cos(\omega_p\tau)d\tau\right\}$$
$$B_R = \mathrm{Re}\left\{\int_0^t f_m^*(\tau)\sin(\omega_p\tau)d\tau\right\},\ B_I = \mathrm{Im}\left\{\int_0^t f_m^*(\tau)\sin(\omega_p\tau)d\tau\right\}. \tag{2.14}$$

Equation (2.11) can be expressed in the following form,

$$\begin{aligned}\underline{u}(x,z,t) &= \sum_{m=0}^{\infty}\tau^m \frac{1}{\sqrt{g_{mm}}}\underline{X}_m(z)\exp(ik_n x)\\ &= \frac{1}{\ell}\sum_{m=0}^{\infty}\left\{\underline{A}_+ exp\left(i(k_n x-\omega_p t\right)+\underline{A}_- exp\left(i(k_n x+\omega_p t\right)\right\},\end{aligned}$$

where

$$\underline{A}_-(z;\omega,k) = -\frac{1}{2\omega}\frac{1}{\bar{g}_{mm}}\ \underline{X}_m(z)\left(\left(B_R + A_I\ \right)+i\left(A_R - B_I\right)\right) \tag{2.15}$$

and

$$\underline{A}_+(z;\omega,k) = \frac{1}{2\omega}\frac{1}{\bar{g}_{mm}}\underline{X}_m(z)\left(\left(A_I - B_R\right)+i\left(A_R + B_I\right)\right). \tag{2.16}$$

Consider the case where $\ell \to \infty$. For clarity, index m is replaced with (p,n), and the displacement reads

$$\underline{u}(x,z,t) = \frac{1}{\ell}\sum_{n=0}^{\infty}\sum_{p=0}^{\infty}\underline{A}_- exp\left(i(k_n x+\omega_p t\right)+\underline{A}_+ exp\left(i(k_n x-\omega_p t\right).$$

Using the equality $k_n = 2\pi n/\ell$, it is true that $\Delta k = k_{n+1} - k_n = 2\pi/\ell$, thus

$$\underline{u}(x,z,t) = \frac{1}{2\pi}\lim_{\ell\to\infty}\sum_{n=0}^{\infty}\sum_{p=0}^{\infty}\left\{\underline{A}_{-}exp\left(i(k_n x+\omega_p t\right)+\underline{A}_{+}exp\left(i(k_n x-\omega_p t\right)\right\}\Delta k$$

$$\approx \frac{1}{2\pi}\int_0^{\infty}\sum_{p=0}^{Q}\underline{A}_{-}\exp\left(i\left(kx+\omega t\right)\right)dk+\frac{1}{2\pi}\int_0^{\infty}\sum_{p=0}^{Q}\underline{A}_{+}\exp\left(i\left(kx-\omega t\right)\right)dk,$$

where Q is the last mode that contributes significantly to the sum. Therefore, the contribution of a mode at a point in the angular frequency-wavenumber domain (ω,k) is given by

$$\underline{u}(x,z,t\ ;\omega,k) = \underline{A}_{-}(z;\omega,k)\exp\left(i\left(kx+\omega t\right)\right)+\underline{A}_{+}(z;\omega,k)\exp\left(i\left(kx-\omega t\right)\right). \quad (2.17)$$

Some remarks with respect to the length of the plate ℓ follow. First, if ℓ is treated as finite, a natural discretisation on the wavenumber occurs. Therefore, when solving numerically the dispersion equations, one can use this discretisation, and search for ω at each k_n. Finer discretisation in the wavenumber domain implies that a larger length was assumed. Next, assuming a finite plate length provides analytical results that can be compared up to amplitude with finite element method (FEM) simulation results, as FEM is conducted on finite bodies. Finally, letting $\ell\to\infty$, the solution for an infinite body is obtained in a rigorous and simple way.

The presented analysis is general, i.e., it applies in both cases where Lamb and SH waves are considered. The solutions to the forced Lamb and SH guided wave problems are provided in Chapters 3 and 5, respectively.

2.3. Conclusion

This chapter addressed the background and theoretical underpinnings of guided wave testing at inaccessible locations. A literature review on techniques for inspecting hard-to-reach areas was conducted, where different techniques were discussed and compared. Moreover, the theoretical framework for ultrasonic wave propagation was explored. The discussion covered bulk waves in linear elastic solids and guided waves in plate-like structures. A new solution method based on modal analysis for forced guided wave problems was presented. The proposed method contributes to the understanding of guided wave excitation but also offers a practical solution methodology for forced guided wave problems.

Chapter 3

Single-mode Lamb wave excitation at high-frequency-thickness products using a conventional linear array transducer

3.1. Introduction

In this Chapter, attention is placed on Lamb wave excitation in plates and plate-like structures. The region below 10 MHz·mm has been extensively investigated by several authors, particularly for steel and aluminium samples [13,70–81]. Recently, there has been a research interest in the region above 15 MHz·mm [6,9,10,43,45–47,55,82], which is very attractive because of the potential for medium-range, high-resolution inspection of relatively thick samples at higher frequencies. For example, operation at 20 MHz·mm implies guided waves can be generated on a 10 mm thick plate with a 2 MHz probe. However, due to the dense spacing of modes (see Figure 2.1), multiple modes can propagate simultaneously in the specimen, complicating signal interpretation [28,43]. To

excite a single Lamb wave mode, the study of the influence of key parameters on Lamb wave generation is critical.

Lamb waves can be excited with piezoelectric, laser, or EMATs [83]. Among others, piezoelectric transducer excitation includes wedge [43], comb [84], interdigital [80], periodic [85], phased comb [75,86] or apodised phased comb [41]. The latter is an extension of phased comb excitation, describing the case where both time delays and voltage amplitudes vary across the elements of a conventional linear array probe with individually addressable elements. Such arrays are commonly deployed for bulk phased array ultrasonic inspections due to their flexibility, and therefore guided wave excitation utilising these probes is advantageous as they are readily available and mature. However, transducer size constraints and scanning resolution requirements for common engineering structures obligate manufacturing usually above 1 MHz. This means that excitation at high-frequency-thickness products is required when inspecting plates around 10 mm thick.

Guided wave phased array excitation is influenced by two key objects, namely the excitation and frequency spectrum [13]. The applied pressure load's temporal profile determines the frequency spectrum. This profile is defined as the convolution of the excitation signal and the impulse response of the array elements. In guided wave applications, the excitation signal is typically a finite-cycled toneburst, controlled by the centre frequency, number of cycles, and applied window [71]. The impulse response of an element of the array depends on the specific array design and material properties. Although this response might vary across the elements of the array, these variations are usually minor, and thus all elements are considered identical. Ultimately, the frequency

spectrum functions as a bandpass filter, passing only guided wave modes whose frequencies fall within a specific frequency band. This band is determined by the spectrum's centre frequency and bandwidth [87]. To excite a single mode, a narrowband spectrum is preferred, as unwanted modes outside the band's range are filtered out. The excitation spectrum depends on the number of elements, pitch, time delay law, and apodisation profile employed. In the frequency-wavenumber domain, assuming linear time delays and uniform voltage amplitudes, the points (f, k) where the spectrum maximises appear as straight lines (excitation beams). Their slope is determined by the pitch, and the applied linear time delay law. Among the infinitely many excitation beams, one passes through the origin of the frequency-wavenumber domain. In the frequency-phase velocity domain, this beam appears as a straight horizontal line at constant phase velocity. Commonly, the time delays are adjusted so that the same excitation beam crosses the desired mode at the centre frequency. This way, the two spectra intersect on top of the targeted mode, which is then generated and propagates in the waveguide.

A systematic approach is presented, in an effort to determine the influence of the key parameters related to single higher order Lamb wave mode excitation using a conventional linear array transducer. Employing a linear time delay law, a single low-dispersion higher order mode is targeted at 20 MHz·mm. The arrays the length, pitch and apodisation profile are appropriately determined to optimise single-mode excitation. More specifically, the influence of the number of elements on the bandwidth of the excitation spectrum is investigated. The effect of the pitch on the elimination of the grating lobes is studied in detail. It is shown that, provided an appropriate pitch value, guided wave mode

propagation is unidirectional. This is due to the satisfaction of a condition involving the pitch and wavelength of the selected mode. The possibility of further enhancing the purity of the targeted mode using an apodisation profile is explored. Experiments conducted on an aluminium plate verify the theoretical results. The Full Matrix is acquired, and all signals are reconstructed synthetically.

The organisation of this Chapter is as follows. First, in Section 3.2, an array is modelled as a transient periodic pressure load acting on the top surface of the plate, leading to an explicit expression between the amplitudes of any mode and the parameters relevant to the excitation. Then, a set of conditions related to the number of elements, pitch, and apodisation profile is provided in Section 3.3. In Section 3.4, experimental results are presented using a dataset acquired FMC method. Finally, in Section 3.5, key conclusions are drawn.

3.2. An analytical solution for the apodised phased comb array excitation problem

Consider a piezoelectric array transducer with N elements, width w and pitch s mounted on top of a plate. The cross section of the plate at $y = \frac{b}{2}$ is shown in Figure 3.1. Each element exerts a surface load in the z-direction. The size of the elements in the y-direction is assumed to be much larger than their width (x-direction); therefore, the plane strain condition holds [13].

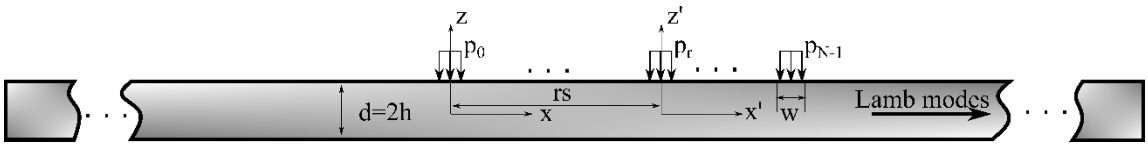

Figure 3.1. Apodised phased comb array excitation model. The plate has thickness d=2h. The pressure load p_r on the top surface of the plate models the r^{th} element.

The external load can be expressed as a summation of the force of each individual element,

$$\underline{F}_{Lamb}(x,t)=\sum_{r=0}^{N-1}\underline{p}_r\ ,\ \underline{p}_r=\left(0,0,\ p_r\delta_D(z-h)\right)^T,$$

where δ_D is the Dirac delta. The solution for an arbitrary element r of the array is expressed in the local frame $x'=x-rs, t'=t-t_r$, as shown again in Figure 3.1. The global frame (x, z) coincides with the local frame of the zeroth element. The pressure load exerted by the element is given by

$$p_r(x',t')=A_r\hat{g}(x';w)\hat{h}(t';M), \tag{3.1}$$

where A_r and $t_r=r\tau$ are the maximum voltage amplitude and linear time delay applied to the r^{th} element, respectively, τ is the time delay constant, $\hat{h}(t')$ is an M-cycle normalised toneburst with centre frequency f_e and $\hat{g}(x';w)$ is the normalised pressure distribution which is considered identical for all elements and is usually modelled as piston-source, parabolic-source distribution or a similar window function of width w. The projection of load $\underline{p}_r$ on the m$^{\text{th}}$ mode assuming a plate of unit width is given by

$$\begin{aligned} f_m &= \int_{-h}^{h}\int_{-l/2}^{l/2} p_r(x,t')\,X_m^3(x)\,X_m^3(z)\,\delta_D(z-h)\,dxdz \\ &= A_r X_m^3(z=h)\hat{h}(t')\int_{-l/2}^{l/2}\hat{g}(x;w)\exp(ikx)dx. \end{aligned} \tag{3.2}$$

Substitution of (3.2) into (2.14), assuming zero initial conditions and neglecting the initial time $t' < M/f_e$, yields

$$A_R = A_r X^3(h)\int_{-\ell/2}^{\ell/2} \hat{g}(x;w)\cos(kx)dx\int_0^{M/f_e} \hat{h}(\tau)\cos(\omega_p\tau)d\tau, \tag{3.3}$$

$$B_R = A_r X^3(h)\int_{-\ell/2}^{\ell/2} \hat{g}(x;w)\cos(kx)dx\int_0^{M/f_e} \hat{h}(\tau)\sin(\omega_p\tau)d\tau, \tag{3.4}$$

and $A_I = B_I = 0$. Substituting (3.3), (3.4), (2.15) and (2.16) into (2.17), the displacement component u^3 of a mode at the top surface of the plate reads

$$\begin{aligned} u_r^3(x',h,t') &= \frac{1}{2\omega}\frac{X^3(h)}{\bar{g}^{Lamb}}(-B_R - iA_R)\exp\left(i(kx'+\omega t')\right) + \frac{1}{2\omega}\frac{X^3(h)}{\bar{g}^{Lamb}}(-B_R + iA_R)exp(i(kx'-\omega t')) \\ &= A_r A_s exp\left(i(kx' \mp \omega t' \mp \varphi)\right). \end{aligned}$$

The expression for u^1 and other components, such as velocity or stress components, is similar. Emphasis is placed on deriving the u^3 component of the displacement field at the top surface of the plate, as this is sampled by the linear array.

The term A_s appears in the following form,

$$A_s(\omega,k) = \frac{1}{2\omega}\frac{X^3(h)^2}{\bar{g}^{Lamb}}\sqrt{\left(\int_0^{M/f_e}\hat{h}(t)\cos(\omega t)dt\right)^2 + \left(\int_0^{M/f_e}\hat{h}(t)\sin(\omega t)dt\right)^2}\left|\int_{-w/2}^{w/2}\hat{g}(x)\cos(kx)dx\right|.$$

Term A_s captures the single-element response of an array element. It can be decomposed into three terms; the first is known as the excitability function, defined as

$$E^{Lamb} = \frac{1}{2\omega}\frac{X^3(h)^2}{\bar{g}^{Lamb}(\underline{X},\underline{X})}.$$

This term is related to the properties of the waveguide and cannot be altered. The normalised excitability function for the first 10 guided wave modes on a 10 mm thick aluminum plate is shown in Figure 3.2 (a). The modes exhibit a transient behaviour until they reach a local maximum, after which their amplitude is strictly decaying. At high frequencies, modes $A0$ and $S0$ combine and form the Rayleigh wave [43], whose excitability remains constant with frequency. Figure 3.2 (b) displays the excitability of the same modes at 2 MHz. Neglecting the Rayleigh wave, the excitability is strictly increasing from mode $A1$ to $A5$. The second term is the frequency spectrum, which can be interpreted as the norm of the Fourier transform of $\hat{h}(t)$,

$$\left\| F\left(\hat{h}(t)\right) \right\| = \left\| \int_{-\infty}^{\infty} \hat{h}(t) \exp(-i\omega t) \right\| = \sqrt{\left(\int_0^{M/f_e} \hat{h}(t) \cos(\omega t) dt \right)^2 + \left(\int_0^{M/f_e} \hat{h}(t) \sin(\omega t) dt \right)^2} \quad (3.5)$$

The temporal profile of the applied load $h(t)$ can be seen as the convolution of the excitation signal and the impulse response of an array element. The frequency bandwidth of the main lobe of the frequency spectrum is approximately given by [41]

$$BW = \frac{2 f_e}{M}. \quad (3.6)$$

The third term is called single-element excitation spectrum, given by

$$H_{SE} = \left| \int_{-w/2}^{w/2} \hat{g}\left(x\right) \cos\left(kx\right) dx \right|. \quad (3.7)$$

This term depends on the element width and spatial pressure distribution profile. Assuming piston-like excitation, the single-element spectrum for an element of width 1

mm is shown in Figure 3.3 (a). The maximum value is reached at $k = 0$ rad/mm, while several local minima and maxima occur in the displayed range. However, Lamb wave modes around 20 MHz·mm propagate at wavenumbers below 4 rad/mm. The effect of element width in this range is shown in Figure 3.3 (b). The amplitude of high-wavenumber modes is reduced with increasing element width. For example, at $k = 3.5$ rad/mm, the amplitude drop is -1.1, -5 and -14.5 dB for element widths of 0.5, 1 and 1.5 mm, respectively.

Linearity of (2.1) permits the expression of the total displacement field as a superposition of the individual solutions of each element. These solutions are transformed to the global frame and summed according to

$$u^3(x,h,t) = \sum_{r=0}^{N-1} u_r^3 = \sum_{r=0}^{N-1} A_s A_r e^{j(kx' \mp \omega t' \mp \varphi)} = A_s \sum_{r=0}^{N-1} A_r e^{j(kx - krs \mp \omega t \pm \omega r\tau \mp \varphi)} = N A_s H_{\pm} e^{j(kx \mp \omega t \mp \varphi - \phi)}$$

where

$$H_{\pm}(\omega,k) = \frac{1}{N}\sqrt{\sum_{r=0}^{N-1} A_r^2 + 2\sum_{r=0}^{N-1}\sum_{q=0}^{r-1} A_r A_q cos\left(\left(ks \mp \omega\tau\right)\left(r-q\right)\right)} \tag{3.8}$$

and (φ, ϕ) are phase values and do not affect modal amplitudes. The above form of the spectrum holds for any linear time delay law and apodisation profile. It is important to note that the modal amplitudes can be decomposed into

$$A_{\pm} = A_S \; H_{\pm}, \tag{3.9}$$

where $A_S = NA_s$. Term A_s is related solely to the response of a single element; thus, it is determined by the frequency spectrum, mode excitability and element width. Multiplication by N is merely rescaling and thus insignificant. On the other hand, the excitation spectrum is strictly related to properties of the array, namely the pitch, number of elements, time delay law and apodisation profile. In the following section, the properties of the excitation spectrum are investigated in detail, to derive a set of conditions for single-mode excitation.

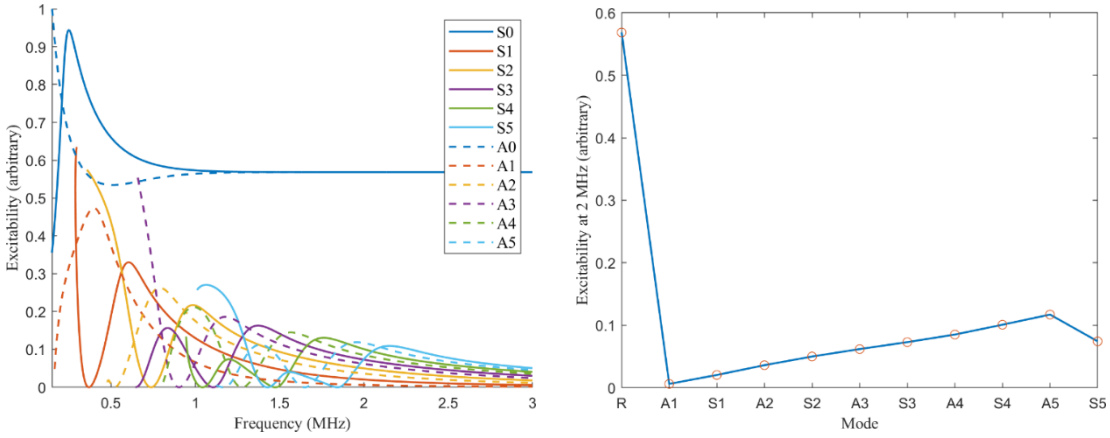

(a) (b)

Figure 3.2. Excitability function for a 10 mm thick aluminium plate. a) Excitability function of the first 10 modes. b) Excitability function of the same modes at 2 MHz.

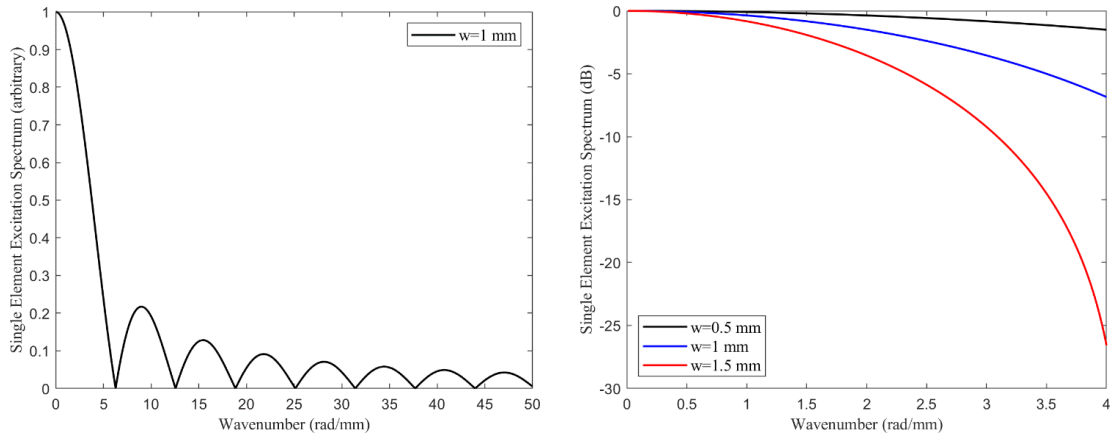

(a) (b)

Figure 3.3. Single-element excitation spectrum. a) Excitation spectrum for element width of 1 mm. b) Excitation spectra for element widths of w=0.5,1 and 1.5 mm. Higher wavenumbers are attenuated with increasing element width.

3.3. Selection of excitation parameters to enhance the purity of a single mode

If uniform amplitudes $A_r = 1$ are considered, the excitation spectrum (3.8) simplifies to

$$H_{\pm}(\omega, k\,; N, s, \tau) = \left| \frac{sin\left(\frac{1}{2} N\left(ks \mp \omega\tau\right)\right)}{Nsin\left(\frac{1}{2}\left(ks \mp \omega\tau\right)\right)} \right|. \tag{3.10}$$

The spectrum depends on angular frequency and wavenumber, while the number of elements, pitch and time delay law are treated as parameters. Furthermore, using the transformations $\omega = 2\pi f, c_p = \frac{\omega}{k}$ and $k = \frac{2\pi}{\lambda}$, equivalent representations such as $H_{\pm}\left(f, c_p; N, s, \tau\right)$ can be obtained. To enhance the forward propagation of a mode, say at

(f_e, c_{pe}), the time delay constant is selected to maximise $H_+(\omega_e, k_e)$, requiring the denominator of the same expression to vanish [86],

$$\sin\left(\frac{1}{2}(k_e\, s - \omega_e\, \tau)\right) = 0 \Rightarrow \tau = \frac{s}{c_{pe}} - \frac{v}{f_e}, \tag{3.11}$$

where $v \leq s\frac{c_{pe}}{f_e}$ and is an integer. For $v = 0$, the method is known as excitation at constant phase velocity [75].

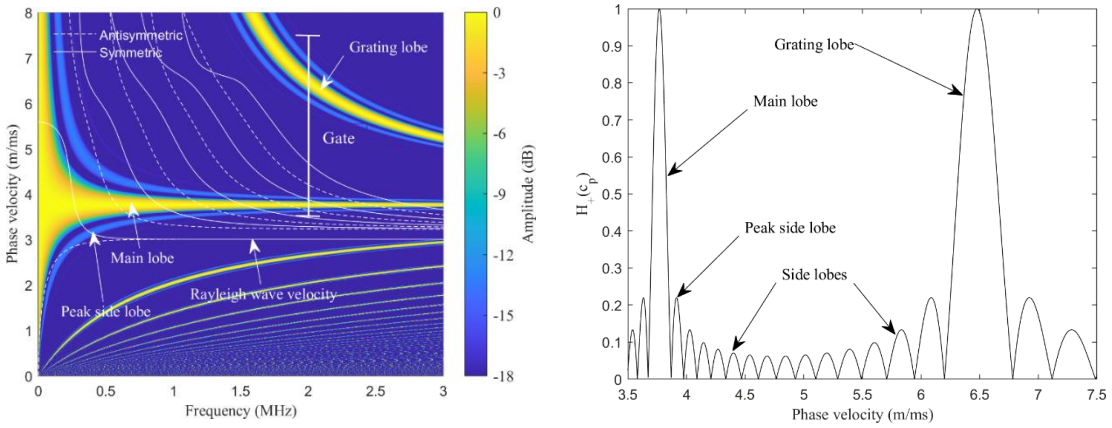

(a) (b)

Figure 3.4. Excitation spectrum H_+ for a 16-element array with a pitch of 4.5 mm. a) Spectrum in the frequency-phase velocity domain. The main lobe is at constant phase velocity. The white lines represent the dispersion curves of a 10 mm thick aluminium sample. b) Gated signal at 2 MHz, showing the main, grating and side lobes.

The excitation spectrum $H_+(f, c_p\,;\, N, s, \tau)$ for a 16-element array with pitch 4.5 mm on top of the dispersion curves (in white) of a 10 mm thick aluminium plate is shown in Figure 3.4 **(**a). Although the pitch value is not representative of a conventional linear array probe, it is selected here to make it simpler to illustrate the attributes of the spectrum, namely the main, grating and side lobes. The time delay constant is set to $\tau = s/c_{pe} =$

1194 ns to enhance $S3$ at $(f_e, c_{pe}) = (2\ \text{MHz}, 3.77\ \text{m/ms})$. The excitation beam at constant phase velocity is shown (main lobe), while several excitation beams appear below and above c_{pe} (grating lobes). Fortunately, not all of these beams are relevant to guided wave excitation. This is based on the fact that all guided wave modes lie within a well-defined region bounded by the Rayleigh wave c_R and cut-off velocity $c_{\text{cut-off}}$,

$$c_R \leq c_p \leq c_{\text{cut-off}},$$

thereafter referred to as the excitable phase velocity region. Therefore, beams outside this region do not intersect with a guided wave mode and thus have no effect on guided wave excitation. For common steel and aluminium samples, $c_R \approx 3$ m/ms and $c_{\text{cut-off}} \approx 22$ m/ms. The excitation spectrum captured by the gate at $f = f_e$ is shown in Figure 3.4 (b). The spectrum consists of the main, side and grating lobes. Note that the display dynamic range in Figure 3.4 **(**a) thresholds all but the biggest amplitude side lobes.

The features of the excitation spectrum in Figure 3.4 (b) are familiar from bulk wave steering. In fact, direct comparison of (3.10) with the directivity function [88] for phased array steering $H_2(\theta_{az})$ reveals that setting

$$\sin\theta_{az} = \pm\frac{c_p\tau}{s} \text{ and } \sin\theta_{st} = 1, \tag{3.12}$$

it turns out that

$$H_2(\theta_{az}) = H_{\pm}, \tag{3.13}$$

where θ_{az}, θ_{st} are the azimuthal and steering angles with respect to the centre of the array, respectively. This means the material for phased array beam steering is transferable to phased array guided wave excitation. However, the performance of the array is not tested against angle θ_{az} but phase velocity, which is not a material constant due to the multimodal and dispersive nature of guided waves. Note that setting $sin\theta_{st} = \pm\frac{c_p\tau}{s}$ and $\sin\theta_{az} = 1$ yields identical results, however, the former choice is made.

In what follows, emphasis is placed on the main attributes of the spectrum to improve guided wave excitation. More specifically, in Section 3.3.1, the bandwidth of the excitation spectrum is defined and an explicit form relating its width to relevant excitation parameters is provided. In Section 3.3.2, a set of conditions on the pitch of the array are derived, to eliminate the grating lobes in the excitable phase velocity region. Finally, the general form of the spectrum is re-considered and an optimised apodisation profile is derived to further enhance the purity of the targeted mode in Section 3.3.3.

3.3.1. Bandwidth of the excitation spectrum at constant phase velocity

At high-frequency-thickness products, the low-dispersion modes can be roughly approximated as straight horizontal lines in the frequency-phase velocity domain. Each guided wave mode can be associated with a phase velocity bandwidth, defined as

$$\Delta c_p^{a\pm} \equiv \left| c_p^a - c_p^{a\pm1} \right|,$$

where c_p^a is the phase velocity of mode a and c_p^{a-1}, c_p^{a+1} are the phase velocities of the modes closest to a such that $c_p^{a-1} < c_p < c_p^{a+1}$. The preceding definition is useful, as it quantifies how 'far' the examined mode is from its neighbours. The phase velocity bandwidth of $S3$ at 20 MHz·mm is shown in Figure 3.5.

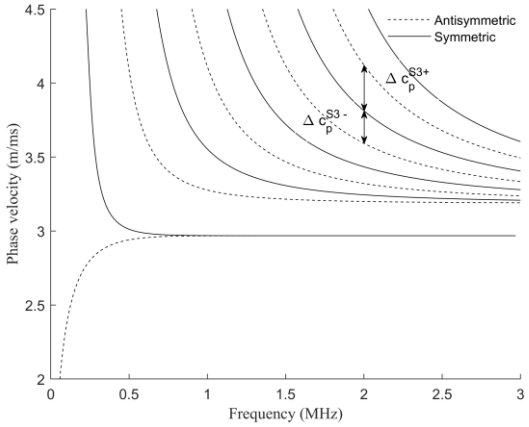

Figure 3.5. Phase velocity bandwidth of mode $S3$ at 2 MHz on a 10 mm aluminium plate.

Next, attention is shifted to the phase velocity bandwidth Δc_p of the spectrum H_+. Based on the above, single-mode excitation requires

$$\Delta c_p / 2 < \Delta c_p^{a+} \text{ and } \Delta c_p / 2 < \Delta c_p^{a-} \tag{3.14}$$

where Δc_p is defined as the phase velocity interval containing the main lobe together with the left and right peak side lobes, see Figure 3.6. More specifically, using (46) from [88] and (3.12) the phase velocity corresponding to the local maxima of the first three side lobes, located on the right-hand side of the main lobe reads

$$c_p \approx \left(1 - \frac{(2m''+1)\lambda_e}{2Ns}\right) c_{pe},\ m'' = -2, -3, -4 \tag{3.15}$$

with corresponding amplitudes at -13.5 dB, -18 dB and -21 dB, respectively, as shown again in Figure 3.6. Including the peak side lobes in the definition of the bandwidth ensures the maximum amplitude outside the bandwidth region is not greater than -18 dB. Note that in the above equation, the dispersion effects are neglected. This is a valid assumption for the low-dispersion modal region. For example, when $S3$ is targeted, the error between the exact phase velocity value corresponding to the maximum of the peak side lobe and (3.15) is less than 0.1%. Employing (29) from [88] and (3.12) and setting $a = \pm 2$, Δc_p is given by

$$\Delta c_p \approx \left(\left(1+\frac{2\lambda_e}{Ns}\right)-\left(1-\frac{2\lambda_e}{Ns}\right)\right)c_{pe} = \frac{4\lambda_e}{Ns}c_{pe}.$$

The above equation shows that the bandwidth of the excitation spectrum increases when the wavelength and phase velocity of the targeted mode are increased but decreases when the total length of the array is increased. The length can be increased by increasing the number of elements or the pitch. However, as will be shown in Section 3.3.2, increasing the pitch can have negative effects, as grating lobes may appear. The phase velocity bandwidth of $S3$ at 20 MHz $\cdot$ mm and the bandwidth of the excitation spectrum corresponding to an array with pitch 0.75 mm operating at 2 MHz for $32, 64$ and 128 elements are given in Table 3.1. We observe that $\Delta c_p^{a-} < \Delta c_p^{a+}$, which suggests that the modal density increases for lower phase velocities. The minimum number of elements required to satisfy condition (3.14) is given by

$$\Delta c_p / 2 < \Delta c_p^{S3-} \rightarrow N > \frac{2\lambda_e}{\Delta c_p^{S3-} s} c_{pe} \rightarrow N > 90,$$

which suggests $S3$ can be excited efficiently with an array length above 68 mm.

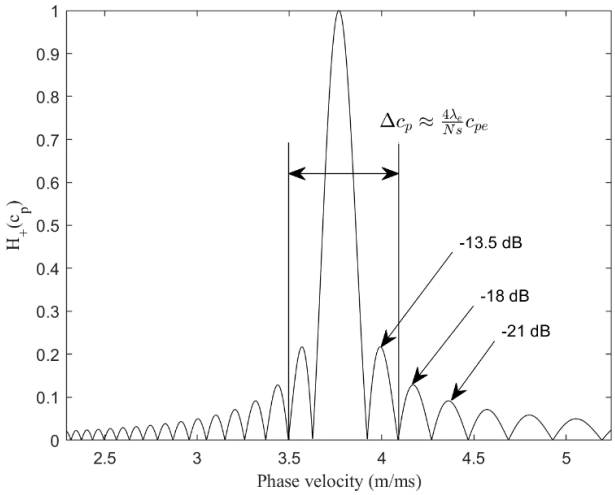

Figure 3.6. Excitation spectrum H_+ at 2 MHz for a 64-element, 0.75 mm pitch array. The maximum amplitude of the peak, second and third side lobes is shown.

Table 3.1. Phase velocity bandwidth at 2 MHz of mode $S3$ and a 0.75 mm pitch array with 32, 64 and 128 elements.

Mode/Spectrum	Phase velocity (m/ms)	Δc_p^{S3+} (m/ms)	Δc_p^{S3-} (m/ms)	$\Delta c_p/2$ (m/ms)
S3	3.77	0.32	0.21	-
32 −element array	3.77	-	-	0.59
64 −element array	3.77	-	-	0.30
128 − *e*lement array	3.77	-	-	0.15

3.3.2. Elimination of grating lobes in the excitable phase velocity region

The grating lobes correspond to local maxima of the excitation spectrum and are found by setting the denominator of the spectrum H_+ to zero. Combining (33) of [88] and (3.12), their location is determined according to

$$c_p(m') = \left(1 - \frac{m'\lambda}{s}\right)\frac{s}{\tau}, \tag{3.16}$$

where m' is an integer. For the general linear time delay law given in (3.11) the main lobe occurs for $m' = v$, while $m' \neq v$ corresponds to grating lobes. Therefore, there exists an infinite number of grating lobes. Nevertheless, as stated earlier, only lobes that lie in the excitable phase velocity region are relevant. To eliminate them in this region, two necessary conditions are required. The first requires the lobe at the right $m' = v - 1$ (see Figure 3.4(b)) of the main lobe to occur at phase velocity higher than the cut-off,

$$c_p\left(m' = v - 1\right) > c_{cut-off}. \tag{3.17}$$

The second condition requires the lobe at the left $m' = v + 1$ of the main lobe to occur at phase velocity lower than the Rayleigh wave velocity,

$$c_p\left(m' = v + 1\right) < c_R. \tag{3.18}$$

At this stage, it is convenient to transform (3.16) in the frequency-wavenumber domain,

$$k = \frac{\tau}{s}\omega + \frac{2\pi m'}{s} = \left(\frac{2\pi}{c_{pe}} - \frac{2\pi v}{f_e s}\right) f + \frac{2\pi m'}{s}. \tag{3.19}$$

This form is advantageous as it explicitly contains the frequency, which can be set to $f = f_e$. In the frequency-wavenumber domain, the excitation beams appear simply as straight lines of equal and positive slope, and the excitation beam for $m' = 0$ intersects the frequency spectrum (in red) on top of $S3$ mode at 2 MHz, as shown in Figure 3.7.

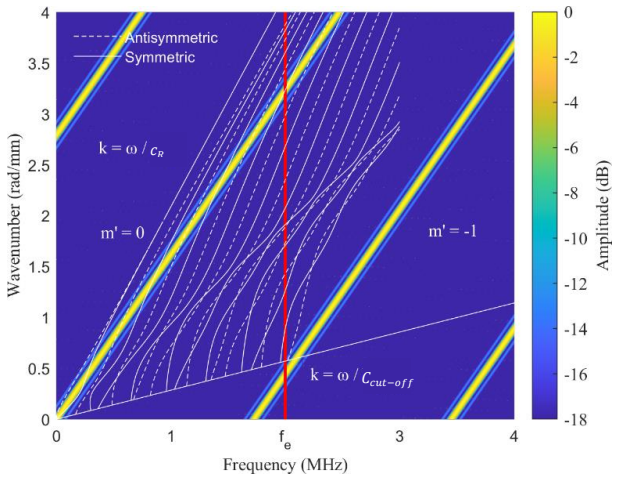

Figure 3.7. Excitation spectrum H_+ in the frequency-wavenumber domain for a 32-element array with pitch 2.25 mm and target mode at (f_e, c_{pe}). The white lines represent the dispersion curves of a 10 mm thick aluminium sample.

Condition (3.17) reads

$$\frac{\omega_e}{c_{\text{cut-off}}} > \left(\frac{2\pi}{\lambda_e} - \frac{2\pi\nu}{s}\right) + \frac{2\pi(\nu-1)}{s} \Rightarrow s < \frac{\lambda_e}{1 - \dfrac{c_{\text{phase}}}{c_{\text{cut-off}}}}. \tag{3.20}$$

Similarly, condition (3.18) is stated as

$$\frac{\omega_e}{c_{\text{R}}} < \left(\frac{2\pi}{\lambda_e} - \frac{2\pi\nu}{s}\right) + \frac{2\pi(\nu+1)}{s} \Rightarrow s < \frac{\lambda_e}{\dfrac{c_{\text{phase}}}{c_{\text{R}}} - 1}. \tag{3.21}$$

Conditions (3.20) and (3.21) set an upper bound for the pitch. Exploiting the fact that $c_{\text{cut-off}} > c_{\text{phase}}$ and $c_R < c_{\text{phase}}$ for any guided wave mode, both conditions can be expressed in the more compact form $s < \min\left(\frac{\lambda_e}{1-\eta_1}, \frac{\lambda_e}{\eta_2}\right)$, where η_1, η_2 are positive numbers such that $c_{\text{phase}}/c_{\text{cut-off}} = \eta_1$ and $c_{\text{phase}}/c_{\text{R}} = 1 + \eta_2$. As an example, consider an array on top of a 10 mm aluminium plate operating at 2 MHz with target mode S3. Then, $\eta_1 = 0.17, \eta_2 = 0.25,\ \lambda_e = 1.88$ mm, and simple calculations yield

$$\text{s} < \min\left(\frac{\lambda_e}{1-\eta_1}, \frac{\lambda_e}{\eta_2}\right) = \frac{\lambda_e}{1-\eta_1} = 2.27 \text{ mm}.$$

Condition (3.20) proved stricter than condition (3.21) at the scenario above. That is indeed the case when low- dispersion modes close to the Rayleigh wave are targeted. Therefore, for the cases examined in this work, only condition (3.21) is significant.

The above conditions do not eliminate grating lobes in the backward direction. For this purpose, H_{-} is examined. The grating lobes are located at

$$c_p = -\left(1 - \frac{m'\lambda}{s}\right)\frac{s}{\tau}. \tag{3.22}$$

In a similar manner, (3.22) is first transformed to

$$k = -\frac{\tau}{s}\omega + \frac{2\pi m'}{s} = -\left(\frac{1}{\lambda_e f_e} - \frac{v}{f_e s}\right)\omega + \frac{2\pi m'}{s}, \tag{3.23}$$

which shows that the excitation beams related to backward propagation are also straight lines with equal but negative slope. Next, it is required that the excitation beam given by $m' = -v + 1$ does not intersect with the frequency spectrum inside the modal region, as shown in Figure 3.8.

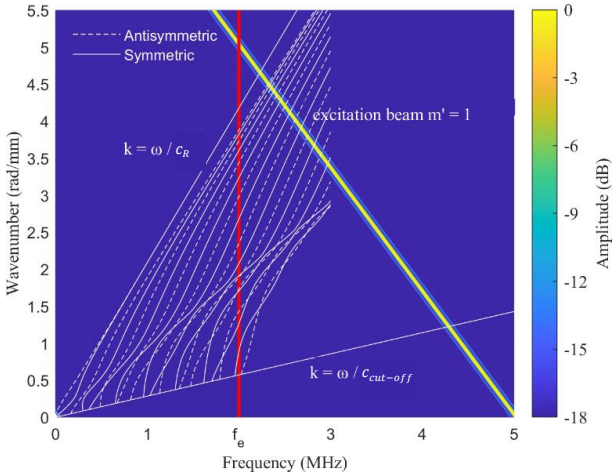

Figure 3.8. Excitation spectrum H_- in the frequency-wavenumber domain for a 128-element array with pitch 0.75 mm and target mode at (f_e, c_{pe}).

This is ensured if the excitation beam assumes a higher wavenumber value that the Rayleigh wave at $f = f_e$,

$$\frac{\omega_e}{c_R} < -\left(\frac{2\pi}{\lambda_e} - \frac{2\pi v}{s}\right) + \frac{2\pi(-v+1)}{s} \Rightarrow s < \frac{\lambda_e}{1 + \frac{c_{\text{phase}}}{c_R}}. \tag{3.24}$$

In contrast to condition (3.20), condition (3.24) is not only necessary, but also sufficient. In other words, if it is satisfied, unidirectional propagation is enforced. Furthermore, if $c_{\text{phase}} \approx c_R$ the condition becomes $s < \frac{\lambda_e}{2}$, which is a well-known condition applied in

phased array beam steering [88]. Note that this condition is related only to the unidirectionality of the mode and not to propagation in the forward direction.

Although conditions (3.20) and (3.24) were derived in a systematic way, some assumptions were made. Specifically, the whole derivation is solely based on the excitation spectrum, completely neglecting the effect of the single-element response. In a sense, it is assumed that a single element distributes energy uniformly across the modes, when in fact, more energy is distributed to the low-wavenumber modes, especially for arrays with large-width elements. Furthermore, the excitation beams and frequency spectrum are simply treated as lines with zero bandwidth. For these reasons, in practice, these conditions are expected to be slightly violated.

3.3.3. Apodisation

Apodisation profiles can be employed to potentially improve guided wave excitation. Standard apodisation windows such as Hanning or Blackman eliminate the side lobes but increase the width of the main lobe [41]. In this section, an apodisation profile is derived based on an optimisation process. This optimised profile is compared with common apodisation profiles in Section 3.4.3.

Consider the general form (3.8) of the spectrum H_+. First, the terms that do not depend on frequency or wavenumber are omitted. The modified spectrum is given by

$$\bar{H} = \sum_{r=0}^{N-1} \sum_{q=0}^{r-1} A_r A_q \cos\big((ks - \omega\tau)(r - q)\big),$$

which can be expressed in the more compact form

$$\bar{H} = \underline{A}^T \hat{H} \underline{A},$$

$\bar{H} = \underline{A}^T \hat{H} \underline{A}$, where $\underline{A} = (A_0, \dots, A_{N-1})^T$ and $\hat{H}$ is a $N \times N$ matrix with elements

$$[\hat{H}_{rq}] = \begin{cases} \cos\big((ks - \omega\tau)(r-q)\big), & q < r \\ 0, \text{ otherwise} \end{cases}$$

where $r, q = 0, \dots, N-1$. Next, an objective function that needs to be maximised is defined [77,89],

$$\Delta = \frac{\underline{A}^T \hat{H}_e \underline{A}}{\underline{A}^T \hat{H}_s \underline{A}}, \tag{3.25}$$

where $\hat{H}_e = \sum_{p'=0}^{P'} \hat{H}_{ep'}\left(f_{ep'}, k_{ep'}\right)$ and $\hat{H}_s = \sum_{p''=0}^{P''} \hat{H}_{sp''}\left(f_{sp''}, k_{sp''}\right)$. The points in the frequency-wavenumber domain $\left(f_{ep'}, k_{ep'}\right), \left(f_{sp''}, k_{sp''}\right)$ correspond to modes to enhance and suppress, respectively. The critical points of Δ are found by imposing the following requirement

$$\partial_{A_r} \Delta = 0 \Rightarrow \left(\hat{H}_e + \hat{H}_e^T - \lambda\left(\hat{H}_s + \hat{H}_s^T\right)\right)\underline{A} = \underline{0} \Rightarrow R\underline{A} = \kappa \underline{A}, \tag{3.26}$$

where $R = \left(\hat{H}_s + \hat{\mathrm{H}}_\mathrm{s}^\mathrm{T}\right)^{-1}\left(\hat{H}_e + \hat{\mathrm{H}}_\mathrm{e}^\mathrm{T}\right)$. Solution of (3.26) results in finding the eigenvalues and eigenvectors of R. In the cases examined in Section 3.4.3, R was found to be an invertible matrix. The apodisation profile is selected as the eigenvector $\underline{A}_{\text{opt}}$ which corresponds to the largest eigenvalue κ_{max}.

3.4. Experimental results

The experimental setup is presented in Figure 3.9. Two linear 2.25 MHz Vermon arrays with 128 elements and a pitch of 0.75 mm were used in pitch-catch configuration on top of a 10 mm thick 6082-T6 aluminium plate. FMC data was collected along an overall line scan of 192 mm by using each element of the receiver probe as independent receiver. The length of the phased array probe is 96mm so the 192mm line-scan was captured in two steps (2x96 mm) by manually moving the probe. The separation distance was set in the first capture at approximately 200 mm edge-to-edge. The transducers were aligned with a metallic frame (not shown in Figure 3.9). The signals were generated and received with the 32Tx/32Rx/128E FI Toolbox [90], which is an array driver capable of producing arbitrary waveform signals using pulse width modulation with a 3-state pulser. The sampling frequency was set to 50 MHz. To excite a single mode, a narrowband signal was required. For that reason, in all the following results, the excitation was a 14-cycle Hanning windowed toneburst centred at 2 MHz, leading to 20 MHz·mm operating frequency-thickness product. The excitation signal was Hanning windowed to suppress any sidelobes [71]. The selected number of cycles narrows the frequency band of the signal to approximately 0.17 MHz at -6 dB. Although this is desired to excite a single mode, an immediate downside is the decrease in spatial resolution of the travelling wave as the length of the wave-packet increases. However, the wavelengths of the guided wave modes at 20 MHz·mm are in the range of $1.5 - 3$ mm for the low-dispersion modes, say $A1 - S5$. This can compensate for the high number of cycles. All two dimensional fast

Fourier transform (2DFFT) [91] results are presented on top of the dispersion curves (in white) for the 10 mm thick aluminium sample that was used for the experiments.

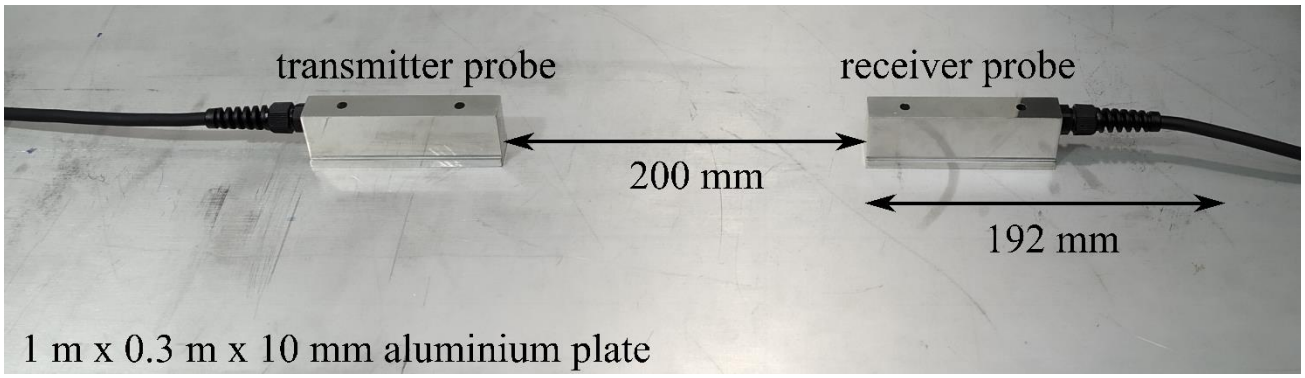

Figure 3.9. Experimental setup, showing two linear 2.25 MHz arrays with 128 elements operating in pitch-catch technique on top of a 10 mm 6082-T6 aluminium plate.

All signals were reconstructed synthetically [92,93]. More specifically, given the full matrix of signals $[\gamma_{rq}(t)]$, where index r and q denote the transmitting and receiving elements, respectively, the linearity of (2.1) suggests the reconstructed signal at x_q is given by

$$\gamma\left(x_q, h, t\right) = \sum_{r=0}^{N-1} A_r \gamma_{rq}\left(t - t_r\right).$$

This means once the full matrix is obtained, any delay law and apodisation profile can be constructed synthetically. In this work, only linear time delays are considered; however, general voltage amplitudes A_r are addressed in Section 3.4.3.

The 2DFFT of a single element of the array is shown in Figure 3.10. Considering the amplitude decomposition (3.9), this plot is related to term A_S. Essentially, the single-element response sets an amplitude floor, which is then enhanced or suppressed by the

excitation spectrum. Simple examination reveals more energy is placed in the low-wavenumber modes, which are in general more dispersive, such as $A8$ and $S8$, while little energy is distributed to higher wavenumber modes, such as $A1$ and $S1$. The 2DFFT map reveals that there is an offset between the experimental data and the dispersion curves, especially for high-wavenumber modes. This error is likely due to the frequency-wavenumber discretisation involved in the 2DFFT [94]. The numerical error was found to be around 3% and did not cause any problems throughout the analysis, so it was deemed acceptable for the purposes of this work.

In the experimental results that follow, mode $S3$ at $(f_e, k_e) = (2\text{ MHz}, 3.34\text{ rad/mm})$ was targeted. Based on the excitability function presented in Figure 3.2 (b), $S3$ is more excitable than any lower order mode at 20 MHz·mm. Furthermore, this mode is less dispersive compared to higher order modes such as $A5, S5, A6, \cdots$,A9. Modes $A4$ and $S4$ exhibit little dispersion and high excitability. However, mode $S3$ was preferred due to its lower wavelength at 2 MHz, namely 1.89 mm, over 2.03 and 2.21 mm of $A4$ and $S4$, respectively. Modes A4 and S4 are also considered in Section 3.4.3. In all that follows, modes $S3, A4$ and $S4$ were excited using (3.11) with $v = 0$.

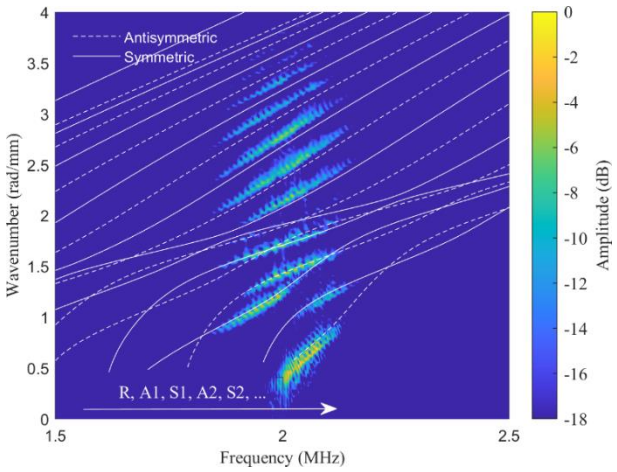

Figure 3.10. 2DFFT of a single element for a 14-cycle Hanning windowed toneburst centred at 2 MHz. More energy is distributed to the low-wavenumber modes.

3.4.1. Experimental investigation of the influence of the excitation spectrum's bandwidth on single-mode excitation

Three different setups are presented, varying the number of elements in the transmitter array, to investigate experimentally the effect of the excitation spectrum's bandwidth on guided wave excitation. In all setups, uniform amplitudes $A_r = 1$ and time delay constant $\tau = 200$ ns were employed. The excitation bandwidth as given in Table 3.1 is plotted in red on top of the 2DFFT results presented in Figure 3.11 (a), (b) and (c). In the first configuration, only the first 32 elements of the transmitter array were used. As shown in Figure 3.11 (a), a significant amount of energy is distributed not only to $S3$ but also to its neighbours, namely modes $A3$ and $A4$. This is expected, as the excitation bandwidth associated with a 32-element array is large enough to significantly overlap with $A3$ and $A4$ around 2 MHz. In the second configuration, the first 64 elements were used for the excitation. Energy leakage is reduced, and more energy is focused on mode $S3$, see Figure 3.11 (b). This is due to the narrower spectrum bandwidth of a 64-element array. Finally,

the excitation is further improved by utilising all 128 elements and can be considered single mode. Overall, the response improves significantly when the number of elements is increased, which narrows the bandwidth of the excitation spectrum. Example A-scans for the three configurations investigated are provided to help understand the effect of the number of elements on the excitation. The signals shown in Figure 3.12 (a), (b) and (c) were captured at a distance of around 303, 307 and 320 mm from the first element of the transmitter array, respectively. This way, the peak amplitude of S3 occurs around 122 μs for all three cases. The group velocities of $A3, S3$ and $A4$ were found to be 2.77 m/ms, 2.62 m/ms and 2.45 m/ms, respectively, with errors less than 0.5%, 0.5% and 1.3% compared with the theoretical group velocities obtained from the Dispersion Calculator [95].

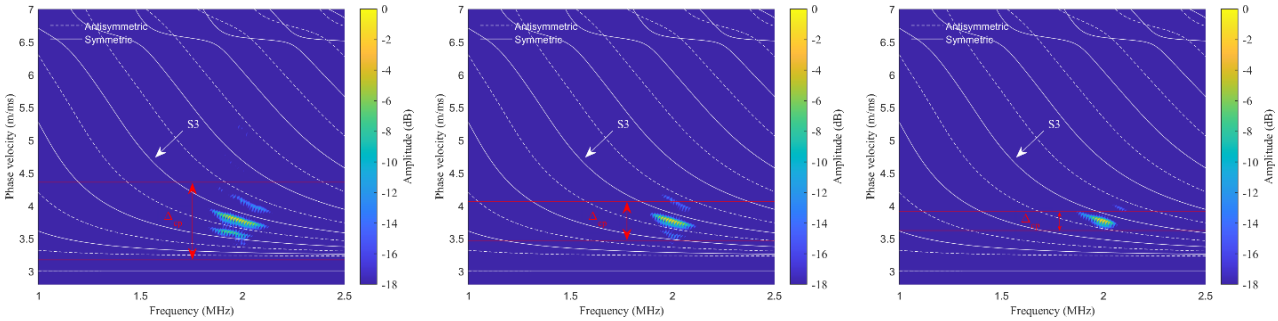

(a) (b) (c)

Figure 3.11. 2DFFT produced with a 0.75 mm pitch array and a) 32, b) 64 and c) 128 elements.

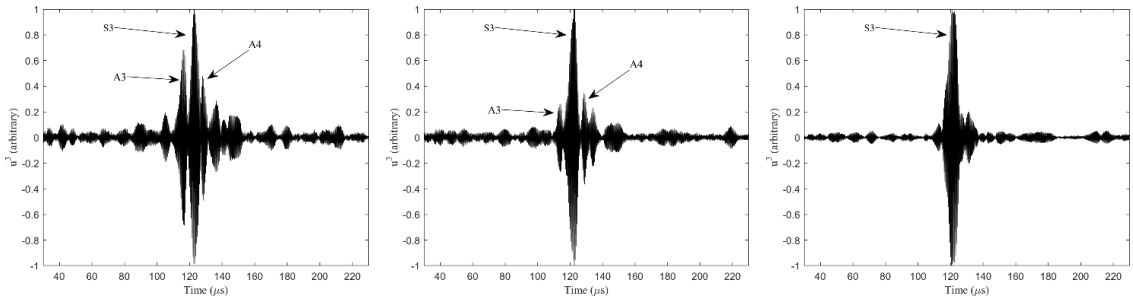

(a) (b) (c)

Figure 3.12. Example A-scans targeting mode S3 varying the number of elements. a) 32 elements were used; modes A3 and A4 are present. b) 64 elements were used; modes A3 and A4 are suppressed. c) 128 elements were used; mode S3 is dominant.

3.4.2. Experimental verification of the generation of grating lobes

Another set of experiments was conducted to examine the validity of conditions (3.20) and (3.24), which read $s < 2.27$ mm and $s < 0.84$ mm, respectively.

The 2DFFT in the forward direction for $s = 1.5, 2.25$ and 3 mm is shown in Figure 3.13 (a), (b) and (c). The data was obtained from the same FMC dataset by skipping one, two and three elements of the transmitter array. The active aperture was kept constant at 96 mm, and voltage amplitudes were uniform. Throughout the plots, the red line indicates an excitation beam. For $s = 1.5$ mm, condition (3.20) is satisfied and a single mode is generated in the forward direction, as no excitation beams intersect with the frequency spectrum and only $S3$ is excited, see Figure 3.13 (a). The response is very similar to the one presented in Figure 3.11(c). However, for $s = 2.25$ mm, an unwanted mode is generated, as shown in Figure 3.13 (b). The location of the unwanted mode is at the intersection of the frequency spectrum with an excitation beam (grating lobe), which can be found by substituting $m' = -1$ in (3.19). This means condition (3.20) is violated somewhat earlier in practice, which is expected, as both the frequency and the excitation beams are associated with finite bandwidths. The effect of the $m' = -1$ beam is present also for $s = 3$ mm, as shown in Figure 3.13 (c). The increase in pitch has shifted the beam

to the left; thus, compared to the previous case, a higher wavenumber unwanted mode is generated.

Next, the 2DFFT for guided wave propagation in the backward direction is presented in Figure 3.13 (d), (e) and (f), for $s = 1.5,\ 2.25$ and 3 mm, respectively. This time, the time delay law applied synthetically is given by $t_r = (N-1-r)\tau$, to mimic a beam propagating in the $-x$ direction. In what follows, the 0 dB value corresponds to the maximum amplitude of the forward propagating wave. For example, the 0 dB value in Figure 3.13 (d) corresponds to the maximum amplitude of Figure 3.13 (a). Note that for $s = 0.75$ mm condition (3.21) is satisfied and no energy higher than -18 dB was found to propagate in the backward direction, thus this result is not presented. For all three setups, condition (3.21) is violated and unwanted modes propagate. These are located at the intersection between the frequency spectrum and the excitation beams given by (3.23). Specifically, for $s = 1.5$ mm, the excitation beam for $m' = 1$ intersects the frequency spectrum, and two unwanted modes are generated, as shown in Figure 3.13 (d). Figure 3.13 (e) shows that for $s = 2.25$ mm, the excitation beam for $m' = 1$ does not activate any modes, but the beam for $m' = 2$ does. In Figure 3.13 (f), $s = 3$ mm, two excitation beams intersect with the frequency spectrum inside the modal region, causing lower and higher wavenumber modes to be excited. The above results are in striking agreement with the material developed in Section 3.3.2.

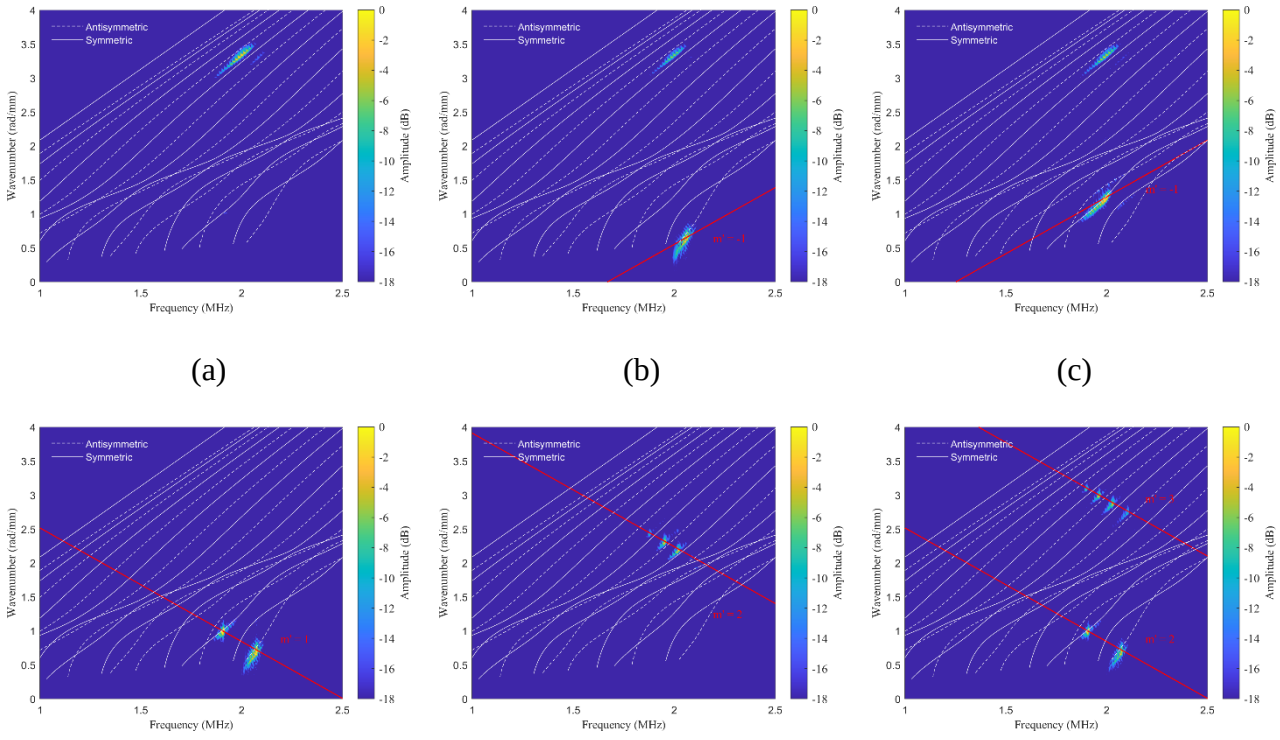

Figure 3.13. Top Row: 2DFFT in the forward direction, varying the pitch value (a) $s = 1.5$ mm. (b) $s = 2.25$ mm. (c) $s = 3$ mm. Bottom Row: 2DFFT in the backward direction, varying the pitch value. (d) $s = 1.5$ mm. (e) $s = 2.25$ mm. (f) $s = 3$ mm.

Similar results can be obtained if the elements of the array are grouped to simulate larger elements. For example, instead of skipping two elements, the array can be partitioned into groups of three elements, combining elements $0-2, 3-5, \ldots, 123-125$. The two approaches are equivalent in the sense that both give the same pitch value. However, the response of a single group is different from the single-element response shown in Figure 3.10, due to the larger width of the group. The 2DFFT of a group that consists of three elements is shown in Figure 3.14. The energy distribution to the higher wavenumber modes is below -18 dB. This makes targeting these modes more challenging, mainly for three reasons. First, even if condition (3.20) is satisfied and no grating lobes are present,

a small amount of energy may still be distributed to low-wavenumber modes, as the group element response enhances these modes significantly. Second, the energy of the high-wavenumber targeted mode is decreased compared to the case where the elements are not grouped, leading to a lower signal-to-noise ratio. Comparison of the 2DFFT result shown in Figure 3.15 (a) with Figure 3.11 (c) revealed that the amplitude of $S3$ was 10 times lower. Finally, if condition (3.20) is violated, the unwanted modes are expected to dominate the signal.

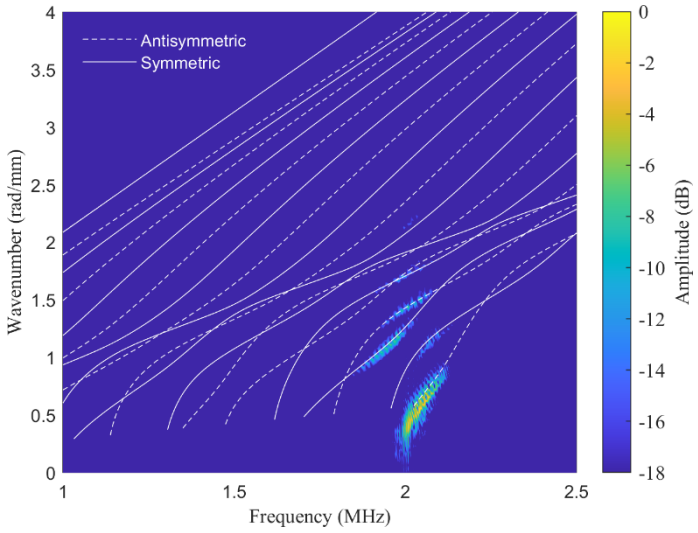

Figure 3.14. 2DFFT of a group of 3 elements. More energy is distributed to the low-wavenumber modes.

Figure 3.15 (a), (b) and (c) present 2DFFT results in the forward direction, grouping two, three and four elements, respectively. The red line on top of the graphs indicates an excitation beam. All remaining parameters were kept identical to the results already presented in Section 3.4.2. The 2DFFT for pitch value 1.5 mm is shown in Figure 3.15 (a). Similar to Figure 3.13 (a), most of the energy is focused on $S3$. However, in this case,

energy leakage toward low-wavenumber modes is present. Figure 3.15 (b) and (c) correspond to pitch values of 2.25 and 3 mm. Again, these are similar to Figure 3.13 (b) and (c), but with a sharp difference. Specifically, the energy of the targeted mode $S3$ is significantly lower compared to the energy level of the unwanted modes, which dominate wave propagation, being approximately 18 dB higher than S3. This is expected, as the single-group response amplifies low-wavenumber modes, see Figure 3.14. The results for propagation in the $-x$ direction are very similar to the ones already presented in Figure 3.13 (d), (e) and (f), and are therefore not repeated here.

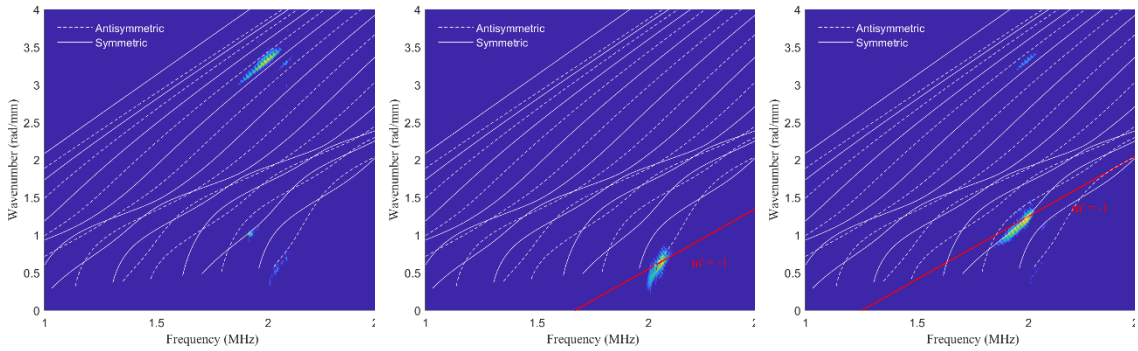

(a) (b) (c)

Figure 3.15. 2DFFT in the forward direction, varying the pitch value. (a) $s = 1.5$ mm. Mode S3 is dominant. (b) $s = 2.25$ mm, (c) s=3 mm.

3.4.3. Experimental assessment of apodisation

The experimental results presented so far assume uniform voltage amplitudes across the elements of the array. This raises a natural question, whether an apodisation profile can improve the purity of the targeted mode. Here, three apodisation profiles are compared, namely uniform, Blackman window and optimised, as shown in Figure 3.16 (a). The optimised profile is the result of the optimisation problem described in Section 3.3.3,

where the points in the frequency-wavenumber domain to enhance and suppress are manually selected based on Figure 3.11 (c). In general, the definition of a suitable objective function is a subtle issue; different apodisation profiles result from different definitions. Here, the points to enhance and suppress are the points of maximum amplitude of $S3$ and $A4$, which in the frequency-phase velocity domain are given by $(f_{e,}\, c_{pe})$ and $(f_s, c_{ps}) = (2.08\ \text{MHz}, 3.956\ \text{m/ms})$. The effect of each of the three profiles on the phase velocity spectrum gated at 2 MHz is shown in Figure 3.16 (b), similar to Figure 3.4 (b) but plotted in dB scale. As expected, the Blackman window significantly reduces the amplitude of all side lobes; however, the width of the main lobe increases. On the contrary, the optimised profile's spectrum is very similar to the uniform spectrum, with one key difference: the second side lobe's amplitude is significantly reduced. The peak of this side lobe occurs at $c_p = 3.959$ m/ms, which is very close to c_{ps}. The amplitude of $A4$ at (f_s, c_{ps}) depends on the magnitude of the excitation spectrum at the same point. This means that the second side lobe is primarily responsible for the generation of $A4$, and it is exactly the same lobe that is suppressed by the optimised apodisation profile. Therefore, by reducing the magnitude of the second side lobe of the spectrum, the amplitude $A4$ is expected to decrease, which is beneficial to enhance the purity of mode S3.

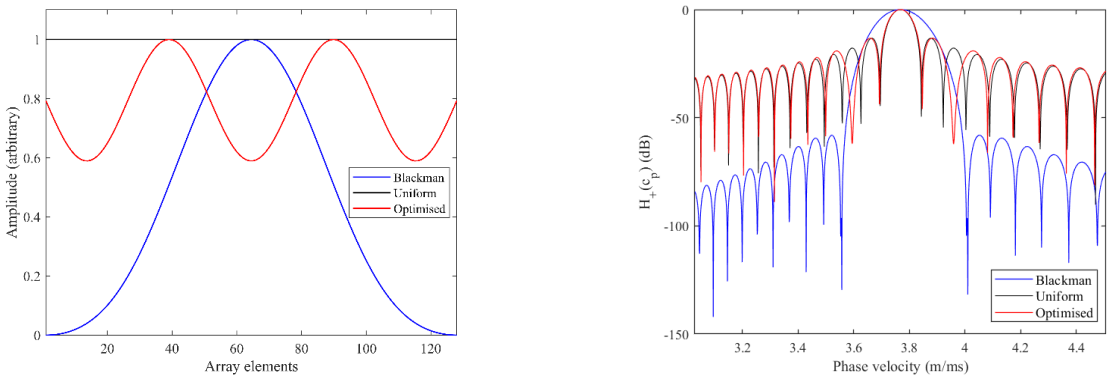

(a) (b)

Figure 3.16. (a) Uniform, Blackman and optimised apodisation profiles for a 128-element array. (b) The excitation spectra for each of these profiles are shown.

The effect of the selected profiles on guided wave excitation is further investigated. Specifically, an experimental 2DFFT for each amplitude profile is computed and shown in Figure 3.17. The overall improvement is visible in the 2DFFT graphs.

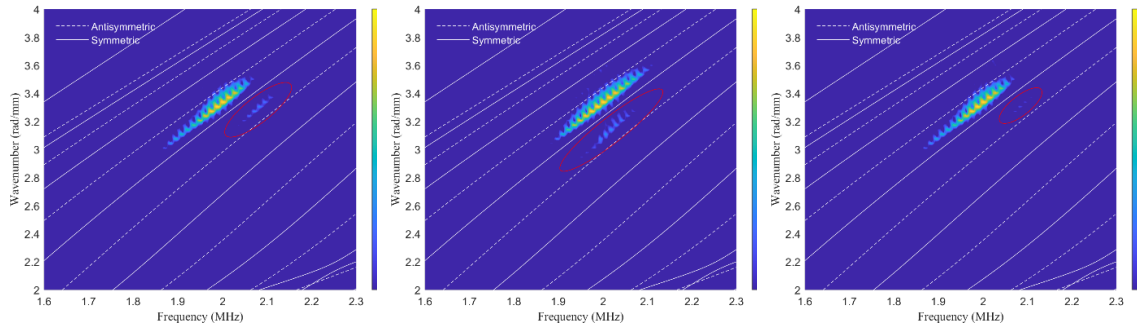

(a) (b) (c)

Figure 3.17. 2DFFT results for different apodisation profiles. The unwanted modes are encircled in red. (a) Uniform amplitudes, (b) Blackman window, (c) Optimised profile.

The performance of each profile is further measured with the definition of an objective function that is similar to (3.25), defined by

$$\Delta^E = \frac{\sum_{p'=0}^{3} A^E\left(f_{ep'}, k_{ep'}\right)}{\sum_{p''=0}^{14} A^E\left(f_{sp''}, k_{sp''}\right)},$$

but in this case $A^E\left(f_{ep'}, k_{ep'}\right)$, $A^E\left(f_{sp''}, k_{sp''}\right)$ represent amplitudes extracted manually from the experimental 2DFFT results. For this calculation, four points of $S3$ and fifteen points of $A4$ were selected around 2 MHz. Then, the amplitude (linear scale) of these points was extracted from the 2DFFT for the cases of uniform, Blackman and optimised apodisation profiles. The experimental objective function together with its numerator and denominator are shown in Figure 3.18. The amplitude of the target mode for uniform amplitude excitation was set to one and all others were scaled accordingly. As expected, the optimised apodisation profile performs better among the selected three, suggesting it is the most appropriate choice for single-mode excitation.

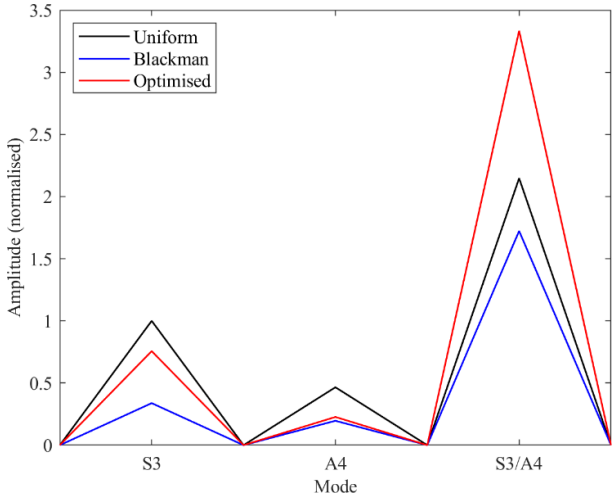

Figure 3.18. Amplitude comparison between uniform, Blackman and optimised profiles.

Next, the possibility of further improving single-mode excitation using apodisation is investigated for more higher order modes, namely $A4$ and $S4$.

Figure 3.19 displays 2DFFT maps in the frequency-wavenumber domain. Uniform voltage amplitudes were employed. At 2 MHz, the wavenumber values of $A4$ and $S4$ read 3.109 rad/mm and 2.814 rad/mm, thus the required time delay constant is 185 ns and 167 ns, respectively. However, since the sampling period is 20 ns, the applied time delays need to be rounded to the closest multiple of 20, leading to 180 ns and 160 ns. This introduces an error of 5 ns and 7 ns. To bypass this issue, the excitation frequency for mode $A4$ was shifted to 1.94 MHz. This way, energy is centred at $(f_{A4}, k_{A4}) = (1.94\ MHz, 2.95\ rad/mm)$, as shown in Figure 3.19 (a). Targeting this point requires a time delay constant $\tau_{A4} \approx 180$ ns. Most of the energy is focused on $A4$, while some energy leakage is observed at modes $S4$ and $S5$. A similar frequency shift may be employed to excite $S4$ at 160 ns. However, to illustrate the effect of applying a time delay law slightly different from the nominal one, mode $S4$ was excited at 2MHz. The maximum energy was found at point $(f_{S4}, k_{S4}) = (1.93\ MHz, 2.58\ rad/mm)$, see Figure 3.19 (b). Although the target mode is excited, in this case, mode $A5$ is significantly excited, spanning a wide range of frequencies, from 1.95 to 2.15 MHz.

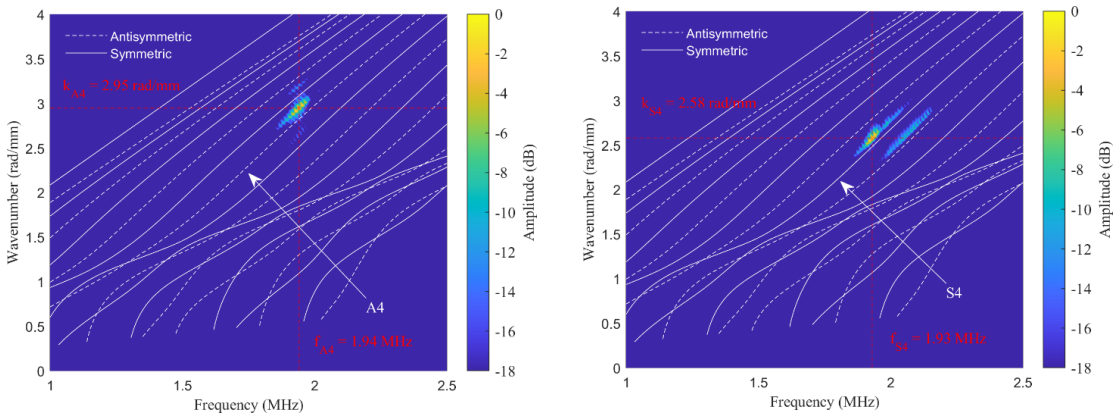

(a) (b)

Figure 3.19. 2DFFT in the frequency-wavenumber domain using uniform amplitudes and targeting modes (a) A4 and (b) S4.

The performance of uniform, Blackman and optimised profiles is tested on the selected modes. The optimised profile for mode $A4$ is shown in Figure 3.20 (a). An objective function according to (3.25) was defined. The point to enhance was selected as the point of maximum amplitude of $A4$. The points to suppress were selected as the maxima of the first three side lobes of the excitation spectrum at 1.94 MHz. Figure 3.20 (b) shows the optimised profile for mode $S4$. Again, the point to enhance was selected as the point of maximum amplitude of the targeted mode. The maxima of the first five side lobes at the same frequency were suppressed. These maxima occur at

$c_p = 4.88, 5.01, 5.15, 5.30\ and\ 5.46$ m/ms.

All these side lobes contribute to the excitation of the unwanted mode $A5$, as it spans a wide frequency range, approximately from 1.94 to 2.6 MHz at -18 dB. In this case, the Blackman window is expected to yield satisfactory results, as it effectively suppresses all side lobes.

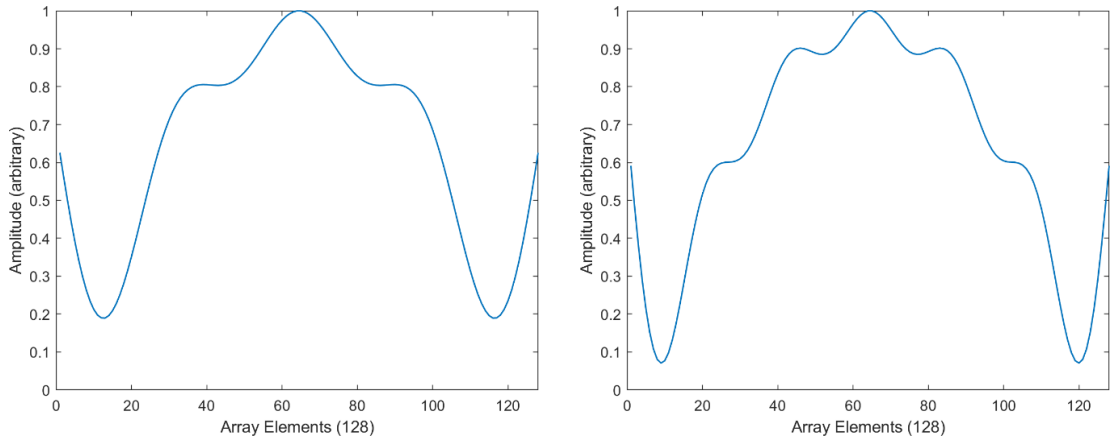

(a) (b)

Figure 3.20. Optimised apodisation profiles for A4 and S4 modes. (a) Apodisation profile targeting A4. (b) Apodisation profile targeting S4.

Figure 3.21 (a), (b) and (c) present 2DFFT results for uniform, Blackman and optimised apodisation profiles when the target mode is $A4$. Visual examination reveals that the optimised profile performs best, see Figure 3.21 (c), while the uniform and Blackman window have similar behaviour. However, this is not true when targeting mode $S4$, see Figure 3.21 (d), (e) and (f). In this case, the Blackman window yields better results, as shown in Figure 3.21 (e). This is not surprising, as the Blackman window suppresses all side lobes, and in this case, multiple sidelobes contribute to the generation of A5. The amplitude of the relevant modes extracted from the 2DFFT graphs is shown in Figure 3.22. The procedure followed was similar to the one described for Figure 3.18. Specifically, eight points along $A4$ and fifteen points along $S4$ and $S5$ around 1.94 MHz were selected for Figure 3.22 (a), while seven points along S4 and seventeen points along $A5$ around

1.93 MHz were selected to produce Figure 3.22 (b). The results agree with the previous observations.

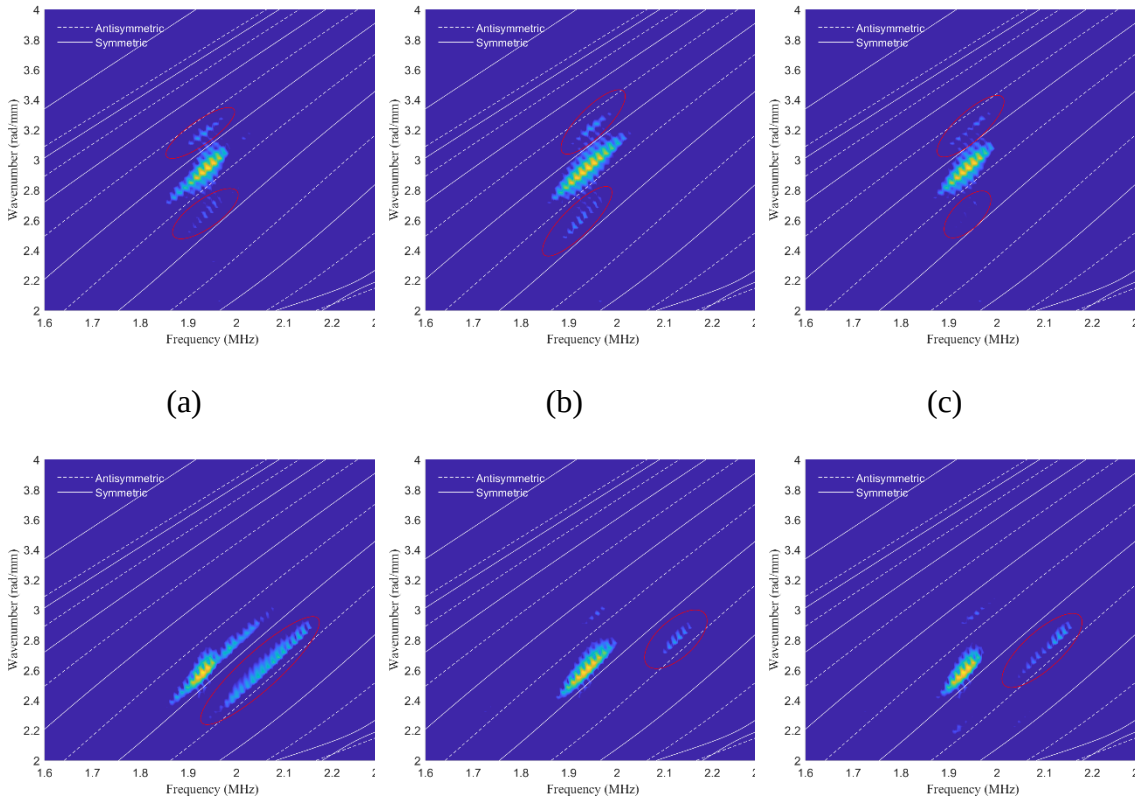

Figure 3.21. 2DFFT results for different apodisation profiles. Top Row (A4): (a) Uniform amplitudes. (b) Blackman window. (c) Optimised profile. Bottom Row (S4): (d) Uniform amplitudes. (e) Blackman window. (f) Optimised profile.

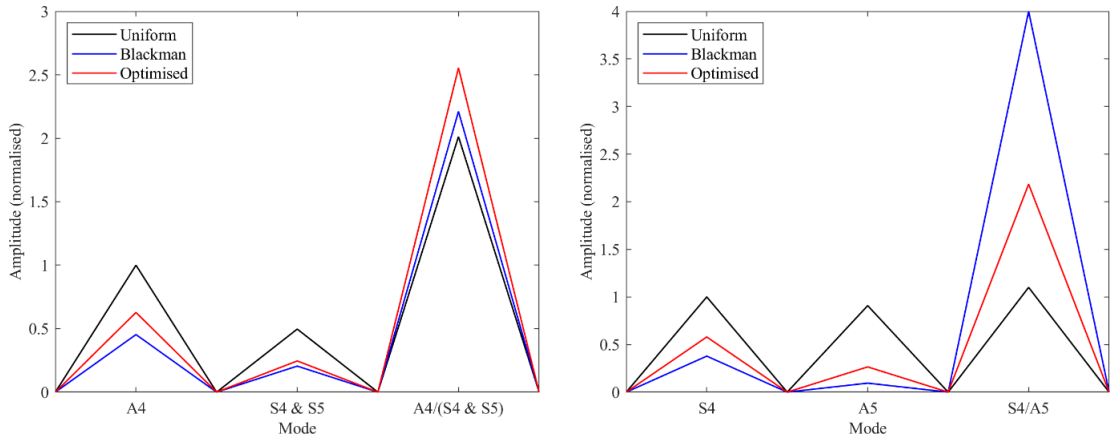

(a) (b)

Figure 3.22 Amplitude comparison between Uniform, Blackman and Optimised profiles. (a) Mode A4 is targeted. (b) Mode S4 is targeted.

3.5. Conclusion

This Chapter focused on the proper selection of key parameters for single-mode excitation in the higher order mode region with a conventional linear array. A linear array was modelled, and an important decomposition between the excitation spectrum and the response of a single element was made. Then, a set of conditions was derived, see Table 3.2. These can be seen as guidelines for the proper selection of the number of elements, pitch and apodisation profile. The first condition determines the phase velocity bandwidth and provided a pitch value decides the number of elements. The second and third conditions are related to eliminating grating lobes in the forward and backward directions, respectively. Violation of the second condition will lead to the propagation of unwanted modes since a grating lobe will intersect with the frequency spectrum, generating low-wavenumber modes. However, satisfaction of the same requirement does not ensure single-mode excitation; for example, unwanted neighbouring modes might be generated

due to the small aperture length of the array. This means this condition is only necessary. On the contrary, the third condition is also sufficient since it ensures unidirectional propagation. This condition is stricter than the necessary condition, in the sense that if it is satisfied, the necessary condition is satisfied as well. Therefore, it can be used to determine the pitch of the array. More specifically, the pitch should be small enough to satisfy this requirement, but large enough to increase the total length of the array and thus decrease the excitation spectrum's bandwidth. Finally, the apodisation profile was optimised, to possibly enhance the purity of the targeted mode. The exact form of the objective function is defined online, after performing a 2DFFT analysis. This can be seen as a calibration process, tuning each voltage amplitude to improve guided wave excitation and propagation.

An experimental FMC dataset was obtained to validate the above theoretical results. This allowed different numbers of elements and pitch values to be evaluated after post processing the same raw data signals. The agreement between the theoretical and experimental results was strong. Emphasis was placed on exciting $S3$, although modes $A4$ and $S4$ were targeted as well. The performance of different apodisation profiles was evaluated for each of these modes. The suitability of the apodised window depended on the energy distribution of the unwanted modes in the 2DFFT map. When they spanned a narrow frequency range, the optimised profile gave better results compared to the uniform amplitudes and Blackman window. However, when the unwanted mode spanned a wider frequency range, multiple side lobes needed to be suppressed. In this case, the Blackman window was found to perform best.

Table 3.2. Conditions for single-mode excitation

Condition No.	Condition	Description
1	$N > \frac{2\lambda_e}{\Delta c_p^{m-} s} c_{pe}$	Suppression of neighbouring modes of targeted mode
2	$s < \frac{\lambda_e}{1 - \frac{c_{\text{phase}}}{c_{\text{cut-off}}}}$	No grating lobes in $+x$ direction
3	$s < \frac{\lambda_e}{1 + \frac{c_{\text{phase}}}{c_R}}$	No grating lobes in $-x$ direction (unidirectional propagation)
4	$\max(\Delta)$	Further enhancement of the purity of the targeted mode

Chapter 4

Medium-range through-thickness focusing using Lamb waves

4.1. Introduction

Although a fair body of work is committed to the development of MR-GWT, there are still important considerations that limit the wide application of the technique. Specifically, while in Chapter 3 it has been shown that a single guided wave mode can be generated and received, it is difficult to size indications reliably and determine the severity of damage using purely the amplitude of the reflection of the received modes. The scattering behaviour of ultrasonic waves is complex and depends on defect size, orientation, and geometry. Moreover, the variation in energy distribution across modes means there is no consistency in the reflectivity from different flaws.

In Chapter 3, an array probe was used to selectively excite a single higher order Lamb wave mode. In this Chapter, an array is used to focus on medium-range distances using Lamb waves. The array is mounted on a wedge to excite and receive modes that require

an incident wave at high angles [43]. Multiple higher order modes are selectively excited and time delayed to arrive simultaneously at a selected cross section, say x_{cs}, as shown in Figure 4.1. The modes are then weighted and superimposed so that energy is focused on a specific point at (x_{cs}, z_f). By altering the modal weights, the focal point can be swept across the thickness of the plate.

The structure of this Chapter is as follows. First, in Section 4.2, Lamb wave focusing is presented, and analytical results are outlined. Next, in Section 4.3, simulation results are presented, testing the technique against various defects. Then, in Section 4.4, experimental results are illustrated and discussed. Finally, in Section 4.5, key conclusions are drawn.

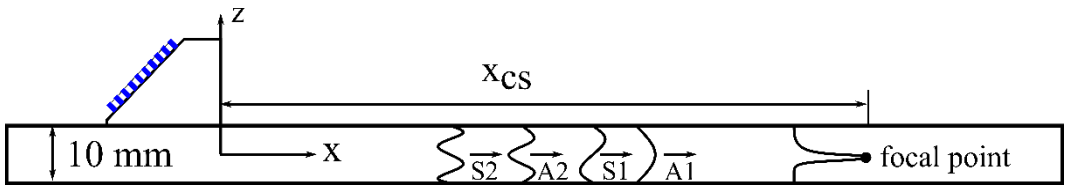

Figure 4.1. Schematic showing Lamb wave focusing approach. Multiple guided wave modes are combined to focus the energy at a specific cross section x_{cs} and depth.

4.2. Theory

In this section, the fundamental theory for Lamb wave focusing is outlined. The excitation of Lamb waves at high frequency-thickness products is discussed in Section 4.2.1. In Section 4.2.2, the details of the method are presented. A sensitivity analysis is performed in Section 4.2.3, to study how various parameters affect focusing.

4.2.1. Single mode excitation at high frequency-thickness products

At high frequency-thickness products, around 20 MHz·mm, the first few higher order modes exhibit little dispersion and have small wavelengths. These properties make them attractive for medium-range NDT applications.

Figure 4.2 displays the through-thickness compressional σ_{11} and shear σ_{13} stress components of the first four higher order modes for a 10 mm thick plate. Mode A1 has a dominant shear stress component, as shown in Figure 4.2 (a). Energy is concentrated at the middle of the plate. Figure 4.2 (b) illustrates the stress profiles of mode S2. The shear wave stress is still dominant, maximising at ¼ and ¾ of the plate thickness. Modes A2 and S2 have both stress fields dominant, as shown in Figure 4.2 (c) and (d), respectively. These four modes are individually excited and superimposed to form a new desired energy distribution. Since all modes have a dominant shear stress profile, this is selected for Lamb wave focusing. To simplify the notation, in what follows, $\sigma \coloneqq \sigma_{13}$.

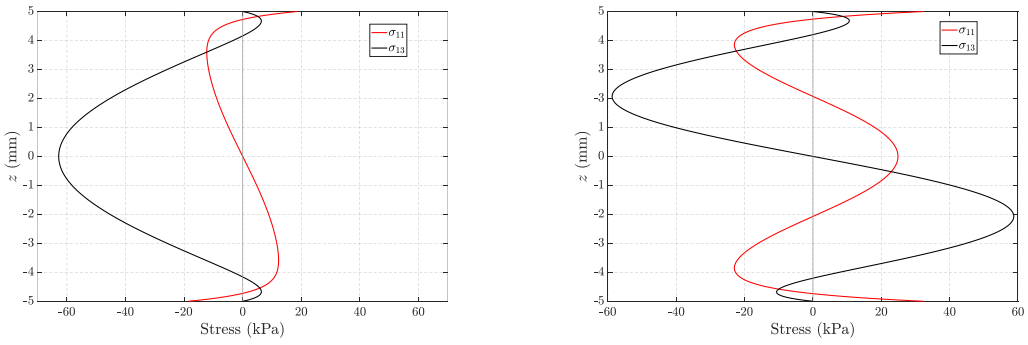

(a) (b)

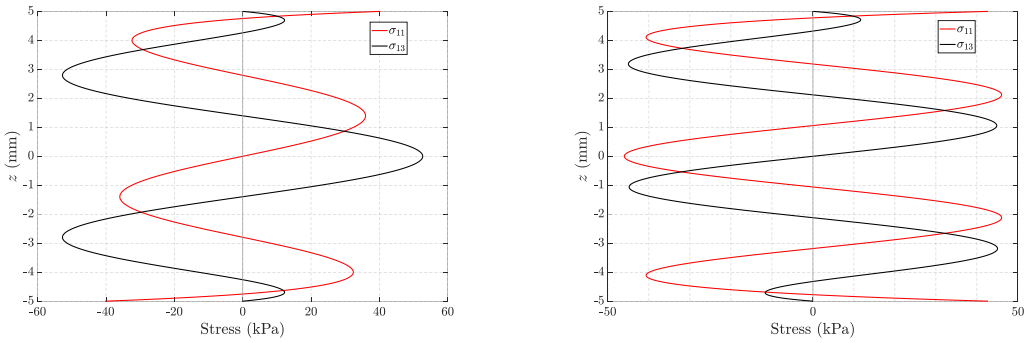

(c) (d)

Figure 4.2. Stress profiles along the thickness direction of mode: (a) A1, (b) S1, (c) A2 and (d) S2.

Consider an array probe mounted on a wedge of angle θ_w, as shown schematically in Figure 4.3. The aperture length of the array is $D \approx Ns$. Applying a linear time delay law, ultrasonic waves are steered at an angle θ_s with respect to the wedge angle. Therefore, by varying θ_s, the angle of incidence, given by

$$\theta = \theta_w + \theta_s$$

can be selected to dynamically target more than one guided wave mode. The plot of frequency versus coincidence angle is shown in Figure 4.4. The first four higher order modes are densely packed around 20 MHz·mm. Unless care is taken, multiple modes are generated simultaneously and propagate in the sample.

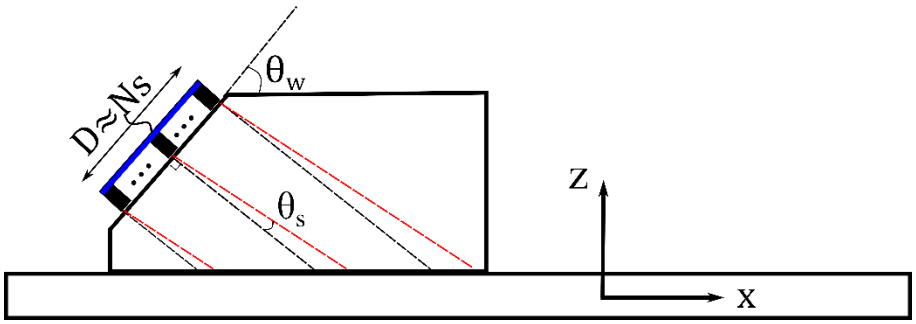

Figure 4.3. Schematic of an array probe mounted on an angled wedge.

The excitation spectrum of a single element probe mounted on an angled wedge is given by Rose [96]. In the case of an array probe, the spectrum appears in the more general form,

$$H_w\left(c_p,\omega\,;N,s,\theta_w,\theta_s\right)=2\frac{\sin\left(0.5Nscos\theta_s\left(\left(\omega/c_w\right)\tan\theta-\omega/c_p cos\theta\right)\right)}{\left(\omega/c_w\right)\sin\theta-\omega/c_p} \qquad (4.1)$$

where c_w is the velocity of the wedge. If no time delays are applied, $\theta_s = 0$, and the spectrum is identical to the single-element transducer case. The plot of equation (4.1) in the frequency-phase velocity domain is shown in Figure 4.5. At high frequencies, the spectrum appears as a horizontal line and has a phase velocity bandwidth. The phase velocity bandwidth of H at -9 dB reads

$$\Delta c_p\left(N,s,\theta_s,\theta_w\right)=\frac{\frac{K}{\pi}\frac{\lambda_e}{D'}}{1-\left(\frac{K}{2\pi}\right)^2\left(\frac{\lambda_e}{D'}\right)^2}$$

where $D'=\frac{Nscos\theta_s}{cos\theta}$ $K = 4.398$ [96]. For a 32-element array with a 1 mm pitch and targeting mode $A1$ at 1.9 MHz, $\lambda_e = 1.7$ mm and thus $\Delta c_p = 0.051$ mm/s. The phase velocity separation between modes A1 and S1 can be found from the dispersion curves to

be $\Delta c_p^{S1-A1} = 3.296 - 3.243 = 0.053$ mm/s. Thus, since $\frac{\Delta c_p}{2} < \Delta c_p^{A1-S1}$, mode A1 can be targeted and solely excited. Since the rest of the higher order modes are greatly separated, it follows that these modes can be excited individually.

Besides the excitation spectrum, excitation of a single mode in a high frequency-thickness product region, around 20 MHz·mm, requires a narrow frequency bandwidth. In practice, this requires a temporal excitation with a relatively large number of cycles. The effect of the frequency bandwidth on the excitation of a single mode is studied experimentally and presented later in Section 4.4.1.

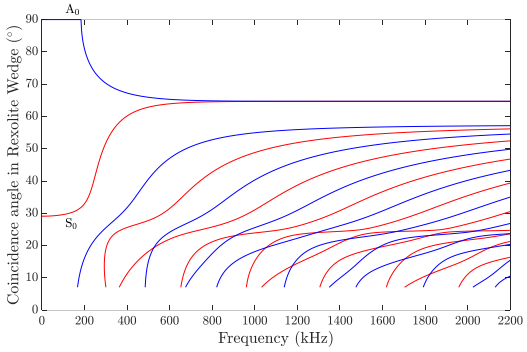

Figure 4.4. Frequency vs. coincidence angle of Rexolite® wedge on a 10 mm thick aluminum plate.

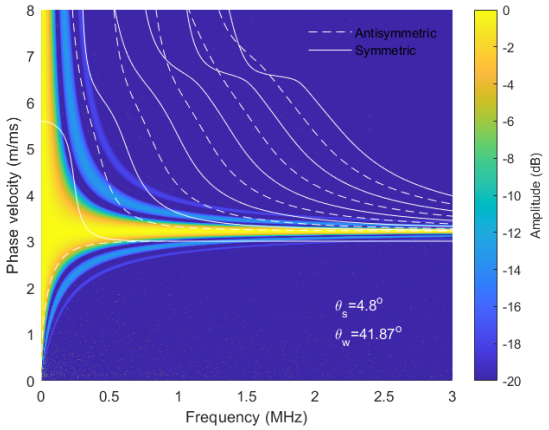

Figure 4.5. Excitation spectrum of an array mounted on an angle wedge in the frequency-phase velocity domain.

4.2.2. Through-thickness multi-modal focusing

To focus the acoustic energy at a specific point along the thickness direction, multiple modes are utilised. Each mode has a different shear stress distribution, denoted $\sigma^a(z)$. The modes can be superimposed to create a new modal profile,

$$\bar{\sigma}(z) = \sum_{a=1}^{Q} w_a \sigma^a(z) \tag{4.2}$$

where w_a is a weight associated with mode a. Obviously, different weight values generate different stress profiles. Therefore, the weights need to be appropriately selected to match a desired profile, say

$$\hat{\sigma}(z; z_f, \sigma_f) = \exp\left(-\frac{(z - z_f)^2}{2\sigma_f^2}\right) \tag{4.3}$$

where z_f is the focal point and σ_f is the width of the focal point at -3.3dB. Indeed, it is straightforward to determine the weights after discretisation along the z-axis and using the Gram-Schmidt process. Figure 4.6 shows the absolute value of the desired and obtained stress profiles after implementation of the Gram-Schmidt algorithm using the first six higher order modes, namely A1, S1, …, S3. The focal point width was set to $\sigma_f = 1$mm. Smaller focal widths yield poorer focusing profiles, thus a focal width of 1 mm was used. The results indicate energy is successfully concentrated for z_f 0, -2 and -3 mm. However, when focusing closer to the bottom surface of the plate, namely at $z_f = -4$ mm, the

agreement between the obtained and the desired profiles is poor. Therefore, the technique has a 'dead zone' close to the bottom surface. The depth of the dead zone is approximately 1.5 mm. Since the focusing results are symmetric along the z axis, an identical dead zone appears close to the top surface. Although the Rayleigh wave can be potentially used for inspection of the top surface of the plate, it cannot be used with a conventional wedge as it is damped by the wedge [43].

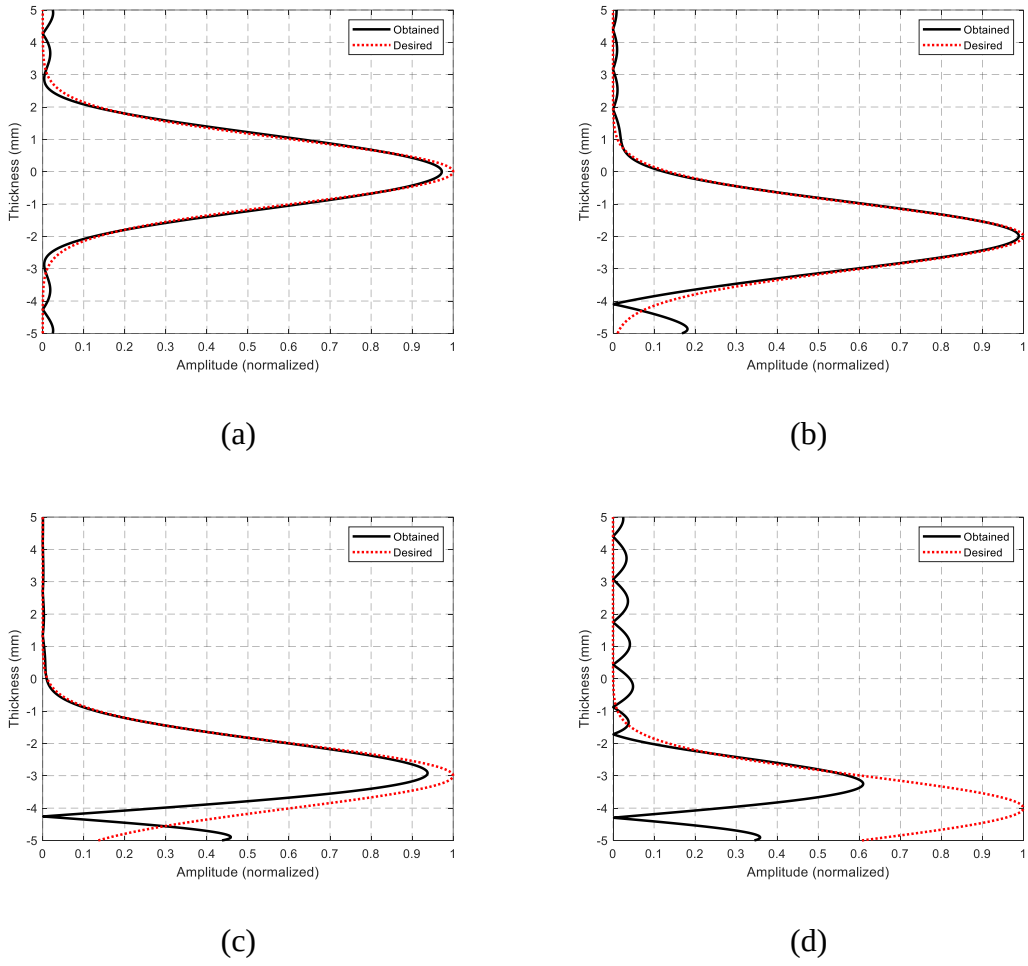

Figure 4.6. Desired vs. Obtained focusing profiles for $\sigma_f = 1$ mm and: (a) $z_f = 0$ mm, (b) $z_f = -2$ mm, (c) $z_f = -3$ mm, (d) $z_f = -4$ mm.

To decide the performance of different modal combinations on focusing, a similarity metric is derived,

$$simm = \frac{\int_{-h}^{h}\int_{-h}^{-h} \bar{\sigma}\left(z, z_f\right)\hat{\sigma}\left(z, z_f\right) dz dz_f}{\int_{-h}^{h}\int_{-h}^{-h} \hat{\sigma}\left(z, z_f\right)\hat{\sigma}\left(z, z_f\right) dz dz_f}.$$

Assuming a perfect match between the desired and obtained profiles at all focal points z_f, the similarity metric equals to one. The metric varies between 0 and 1, giving a score for each combination of modes. The result of the similarity metric for combinations of different modes is shown in Figure 4.7. The result indicates low focusing resolution when using only two modes, A1 and S1. When four modes are considered, namely A1, S1, A2 and S2, the focusing resolution is significantly improved. Superimposing six modes slightly improves the result. Using eight modes barely improves the result. Since adding more modes makes the experimental analysis more involved, practically adding more than four modes does not improve focusing.

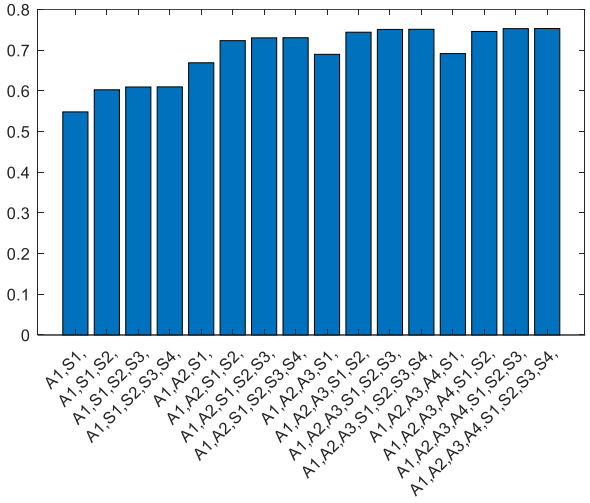

Figure 4.7. Similarity metric value for different modal combinations.

Next, the distribution of stress along the x-axis is investigated. Consider the time-harmonic case of equation (4.2),

$$\bar{\sigma}\left(x,z,t;z_f,\sigma_f\right)=\sum_{a=1}^{Q}\sigma^a\left(z\right)w_a(z_f,\sigma_f)\exp\left(i\left(k^a x-\omega t+\psi^a\right)\right). \tag{4.4}$$

Assuming that the total phase is zero at (t_{cs}, x_{cs}),

$$\phi^a=k^a x_{cs}-\omega\, t_{cs}+\psi^a=0, \tag{4.5}$$

the phase at a distance $\bar{x}$ away from x_{cs} reads

$$\phi^a=k^a(x_{cs}+\bar{x})-\omega t_{cs}+\psi^a=2\pi\frac{\bar{x}}{\lambda^a}. \tag{4.6}$$

Equation (4.6) shows that for $\bar{x}\neq 0,$ phase angles contribute to the sum of (4.4). Figure 4.8 shows the energy distribution along the x-z plane for focusing at four different depths, namely $z_f=0,-1,-2$ and -3 mm. Modes A1, S1, A2 and S2 were utilised using equation (4.4). Note that although the waves are time harmonic and extend infinitely along the x-axis, the energy drops further away from x_{cs}. The reason is that each mode has a different wavelength; thus at distances far from x_{cs}, the modes are not in phase and can cancel each other. In practice, the excitation signal is not time-harmonic and has a non-zero frequency bandwidth. Therefore, the axial length of the wave packet is limited due to the finite duration of the excitation toneburst.

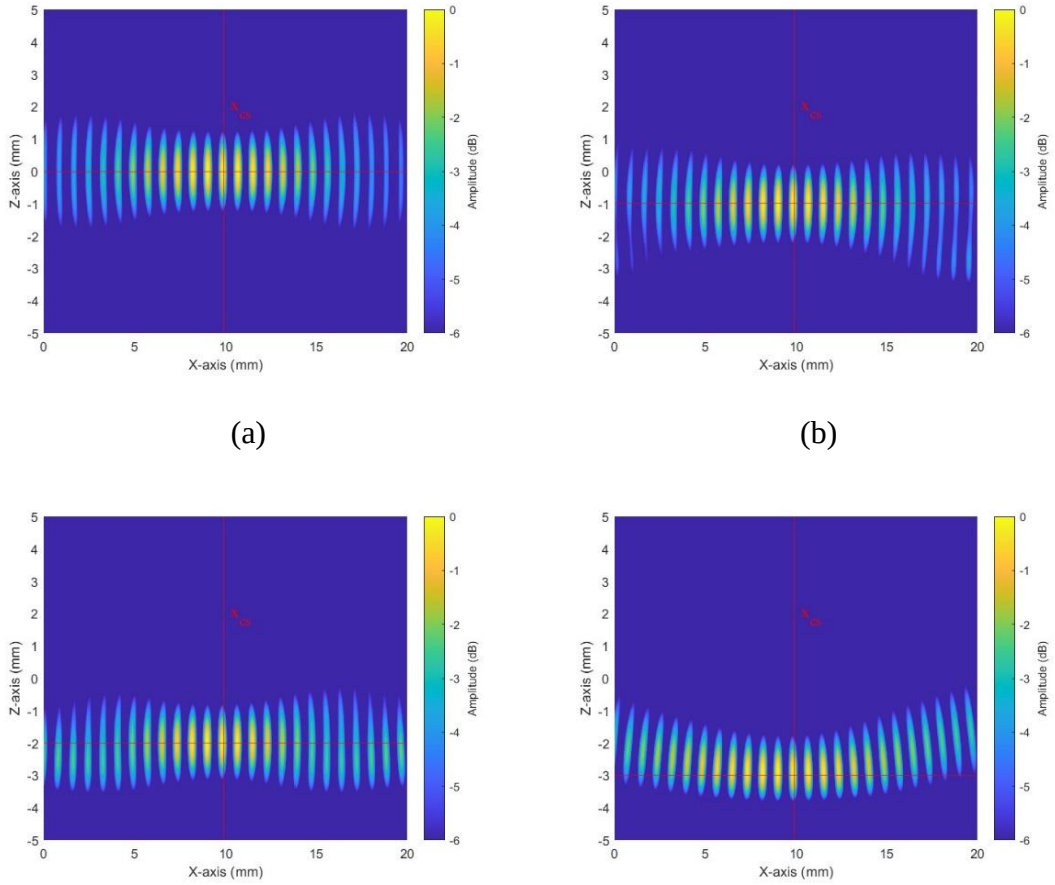

Figure 4.8. Energy distribution at x-z plane after superposition of time-harmonic guided waves at $x = x_{cs} = 10$ mm and $t = t_{cr} = 4.34\ \mu s$, using the first 4 modes.

4.2.3. Sensitivity

4.2.3.1. Sensitivity to phase

So far, it is assumed that all modes are in phase at a desired cross-section, say x_{cs}. In practice, this can be achieved by time shifting the modes to arrive simultaneously at the same cross section. This is performed in simulation and experiments sections as a preliminary step. However, the process of determining the time delays is error prone, which leads to errors in focusing. Consider again the time-harmonic case using modes A1,

S1, A2 and S2. The focusing profile is given by equation (4.4). The phase angle ψ^a can be expressed as

$$\psi^a = \psi_0^a + \psi_1^a,$$

where ψ_0^a is an arbitrary phase angle and ψ_1^a is a phase shift. The phase shift is selected so that all modes arrive simultaneously at $x = x_{cs}$,

$$\phi^a = 0 \rightarrow \psi_1^a = -k^a x_{cs} + \omega\, t_{cs} - \psi_0^a.$$

However, small errors in phase shifts might occur, thus

$$\psi_1^a = \psi_1^a + \psi_{er}^a,$$

and

$$\phi^a = k^a x_{cs} - \omega\, t_{cs} + \psi_0^a + \psi_1^a + \psi_{er}^a = \psi_{er}^a.$$

If the phase error ψ_{er}^a reaches 90°, the contribution of the mode m to the focused profile becomes zero. Moreover, in the case where $\psi_{er}^a = 180°$, the inverted profile contributes to the sum of equation (4.4). This is equivalent to multiplying the mode with a negative weight value and has undesirable results.

Figure 4.9 displays the sensitivity of the similarity metric to phase changes of a given mode. Each curve is obtained by increasing the phase error of only the corresponding mode, whereas all other modes are assumed to be in phase. For example, the curve corresponding to mode A1 (in blue) is obtained by keeping $\psi_{err}^a = 0, a = 2,3,4$ and varying ψ_{err}^1 from 0° to 360°. When the phase error is zero, all modes are in phase and

the similarity metric is about 0.7. As phase changes are introduced, the similarity metric decreases, reaching its minimum value at 180°, when the modes are out of phase. As the phase error further increases, the similarity metric also increases, until it reaches its maximum value at 360°. All modes show the same pattern; however the similarity metric is most sensitive to phase changes of mode A1. This implies mode A1 has a significant contribution to equation (4.4). As modal order increases, the similarity metric is less sensitive to phase errors. The similarity metric is above 0.65 when the phase error is below 35°. At 2 MHz, the corresponding time delay error is $t_{error} = \frac{0.6109}{2\pi f} = 48.6$ ns.

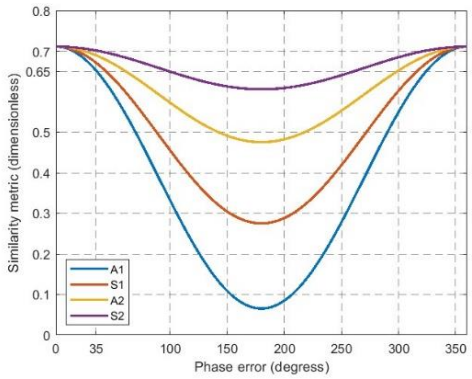

Figure 4.9. Sensitivity with respect to phase error of modes A1, S1, A2 and S2.

4.2.3.2. Sensitivity to small thickness variations

Consider a plate-like structure with a nominal thickness of 10 mm and a small smooth local thickness variation, as shown in Figure 4.10. The wall thickness of a 10 mm thick plate reads

$$d(x) = 10 - \Psi(x),$$

where the indentation function Ψ can be put in the following form

$$\Psi(x)=\begin{cases}\dfrac{\alpha}{e^{-1}}\exp\left(\dfrac{-1}{1-(x/\beta)^2}\right) & x\in(-\beta,\beta)\\ 0, & \text{otherwise}\end{cases}$$

where α is the height and 2β is the length of the indentation.

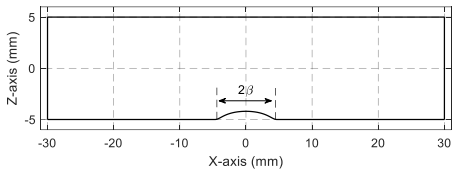

Figure 4.10. Plate with an indentation of 1 *mm extending for* 10 *mm.*

As guided waves propagate through the indentation region, their operating frequency-thickness product slightly changes. Therefore, the propagation speed also changes, and this can lead to phase errors. Assuming time-harmonic waves, the travel time through the wall loss is

$$t_{ind}=\int_0^{2\beta}\frac{1}{c_p\left(d(x)\right)}dx,$$

where the time required to travel a distance of l when the plate is intact is simply

$$t_{int}=\frac{2\beta}{c_p}.$$

Therefore, the phase difference between the two cases can be written in the following form,

$$\phi_{shift}=\omega\left(t_{int}-t_{ind}\right). \tag{4.7}$$

The plot of equation (4.7) with respect to indentation length is shown in Figure 4.11 (a). As expected, in the absence of the indentation, the phase difference is zero. As the indentation length increases, the difference in phase increases linearly. Mode $A1$ exhibits the smallest slope as is the least dispersive amongst the four modes. This is beneficial, as focusing is mostly sensitive to phase changes in mode A1 (see Figure 4.9.) The plot of indentation length vs. the similarity metric is given in Figure 4.11 (b). For lengths smaller than 15 mm, the similarity metric is above 0.65. This means that small thickness variations with a length less than or equal to approximately $9\lambda_{A1}$ (15 mm), do not significantly affect the technique.

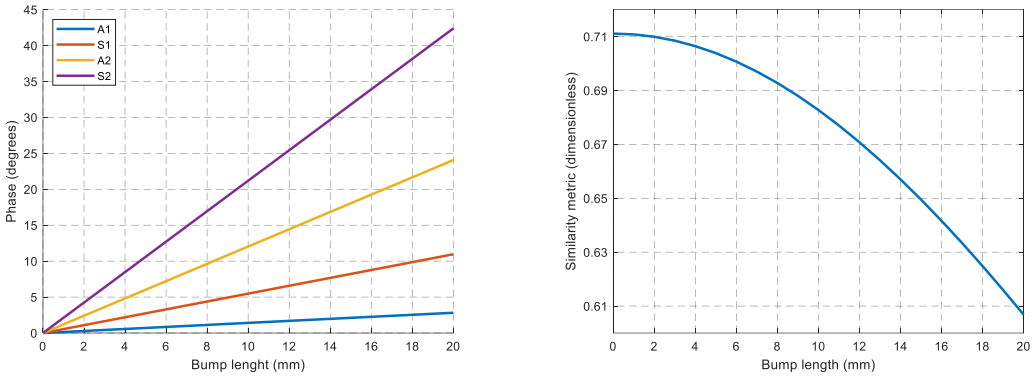

(a) (b)

Figure 4.11. Indentation length vs.: (a) phase change of each mode, (b) similarity metric.

4.3. Simulations

To capture the fundamental physics and speed up simulation time, 2D finite element simulations [97] were developed using OnScale [98]. The mesh size was set to 0.05 mm, which resulted in more than 20 nodes per wavelength [99]. The timestep was set to 5 ns,

which is lower than the time required for the fastest wave to travel through an element of the given size [100].

In Section 4.3.1, a preliminary set of simulations was performed on an intact plate. In Section 4.3.2, focusing simulations were performed on a series of different notches to evaluate the sensitivity and resolution of the technique. Focusing was performed using the first four higher order modes, namely A1, S1, A2 and S2.

Table 4.1. Simulation parameters

Parameters	Wedge Velocity	Wedge Angle	Plate thickness	Plate long. Velocity	Plate shear velocity	Plate density	Array elements	Array pitch	Array element width	Excitation signal centre frequency	Excitation signal number of cycles
	2343 m/s	41.69°	10 mm	6473 m/s	3226 m/s	2700 kg/m^3	32	1 mm	0.75 mm	1.9 MHz	5-A1 15-S1,A2,S2

4.3.1. Extraction of time of arrival and stress profiles on an intact plate

A schematic of the simulation set-up is shown in Figure 4.12. An angled wedge is located on top of a 10 mm thick plate. A 32-element array is mounted on top of the wedge. The array emits plane waves by applying a piston-like pressure load at the wedge-element interface. Using beam steering, guided wave modes are excited. Each mode is excited individually, thus requires a separate simulation. The simulation parameters are given in Table 4.1.

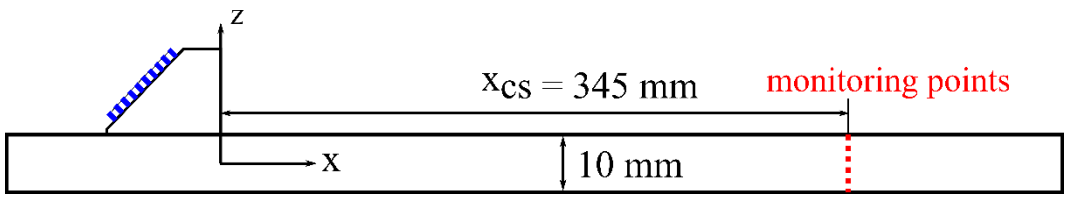

Figure 4.12. Schematic of simulation set-up.

Four simulations were performed to determine the time of arrival t^a and stress profile σ^a of each mode across the cross section at x_{cs}. The time of arrival is defined here as the time when the stress σ^a maximizes. Extracting the time of arrival allows time shifting the modes to arrive simultaneously at x_{cs}. Modes A1, S1, A2 and S2 were generated and received using a vertical monitoring line located at x_{cs}. To keep the results general, x_{cs} was arbitrary selected 345 mm away from the front face of the wedge. The time of arrival of each mode is shown in Table 4.2. The stress profile σ^a along the z-direction was also recorded. This profile is essentially identical to that of Figure 4.2, so it is not repeated here.

Table 4.2. Time of arrival at cross section 345 mm away from the wedge

Mode	A1	S1	A2	S2
Time of arrival (μs)	132.6	138.0	142.0	147.5

4.3.2. Lamb wave focusing

Next, Lamb wave focusing is evaluated against different notches. The length, depth, and position of the notch are varied to evaluate the sensitivity of the technique to different types of flaws. Short and deep notches are simple models of a crack or sharp pit, whereas larger and shallower notches may be used to model a corrosion patch. Unless otherwise stated, all parameters in the simulations are identical to the ones used in Section 4.3.1.

4.3.2.1. Focusing at a notch

The simulation set-up is shown in Figure 4.13. A notch of length ℓ_{notch} and depth d_{notch} is modeled. The notch is located 345 mm away from the front face of the wedge, as in Section 4.3.1. Modes A1, S1, A2 and S2 are excited separately and received independently by all array elements, thus operating in pulse echo mode.

Focusing is performed in post-processing at the front (insonified) face of the notch. The focal points lie at (x_{cs}, z_f) and their number depends on the step of discretisation, which was selected 0.25 mm. First, the received signals are phased according to Table 4.2. Then, for each focal point, guided wave modes are weighted and summed, according to equation (4.2). This leads to the construction of a matrix of the form $[z_f \times R_x \times t]$. Next, for each focal point (x_{cs}, z_f), the signals are beamformed and the reflection amplitude $R(z_f)$ is calculated. It is expected that $R(z_f)$ is large when a reflector is present and small in the absence of a reflector. The beamforming is semi-synthetic, as Lamb waves are physically propagating, but they are superimposed and focused synthetically.

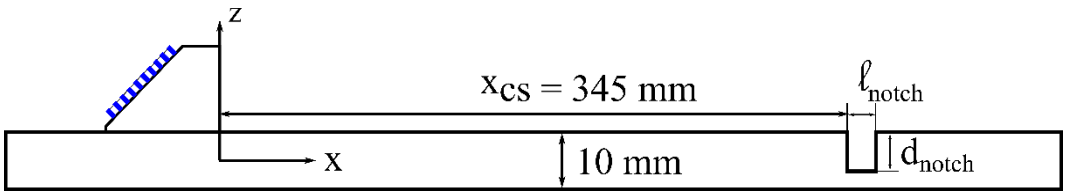

Figure 4.13. Schematic of simulation set-up to image a vertical notch.

Effect of notch length

Three different notches with varying lengths were simulated. The lengths of the notches were chosen to be $\frac{\ell_{notch}=\lambda_{A1}}{4}$, λ_{A1} and $5\lambda_{A1}$, where λ_{A1} is the wavelength of mode A1 and

equals 1.7 mm. The depth of the notches was kept constant at 50% thickness. The beamforming, by combination of the different modes, is as per the methodology outlined in equation (4.3) and this is used to step the focus throughout the thickness. Specifically, the focal point z_f was swept from -3.5 to 3.5 mm and the focal width was set to $\sigma_f = 1$ mm. For $z > 3.5$ and $z < -3.5$, i.e. close to the top and bottom surfaces of the plate, the technique has no focusing ability (see Figure 4.6). Figure 4.14 illustrates the reflection amplitude $R_{notch}(z_f)$ against z_f. The 0 dB value is common for all three cases. Little change is observed between the three cases, meaning the technique is insensitive to length variations, even for lengths smaller than the wavelength. The 0 dB value is common for all three cases. Moreover, the depth of the notch can be accurately estimated. Specifically, a strong reflection is obtained when focusing along the face of the notch. The reflection amplitude is around 0 dB, with a variation of around 1.5 dB. When focusing on depths below the notch, the reflection amplitude drops by 8 dB, with a variation of around 1.5 dB. The depth of the notch can be estimated at

$$R_{call} = \frac{\max R_{notch} + \min R_{notch}}{2} \tag{4.8}$$

where $maxR_{notch}$ and $minR_{notch}$ are the maximum and minimum of the reflection amplitude, respectively. The call line is shown as a horizontal line at $z = -0.15$ mm. The estimated depth is thus 51.5%.

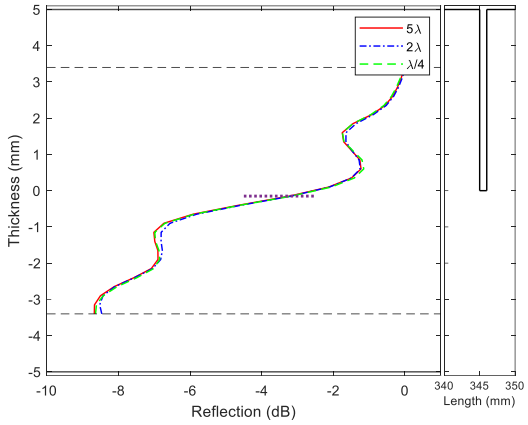

Figure 4.14. Focusing reflection of a 50% deep notch of length $5\lambda_{A1}, 2\lambda_{A1}$ and $\frac{\lambda_{A1}}{4}$.

Effect of notch depth

The effect of notch depth is studied. Three top surface notches were simulated at corresponding depths of 35%, 50% and 70%. The length was kept equal to λ_{A1}. Figure 4.15 illustrates the reflection amplitude for each case. The reflection from the 35% deep notch is shown in red. As expected, the reflection amplitude is approximately constant when focusing along the face of the defect; however it drops significantly when focusing below the notch. The same pattern is observed for the 50% and 70% notches, shown in blue and green, respectively. These results indicate the depth of the notch can be accurately obtained using equation (4.8). Moreover, three bottom surface notches were simulated. The reflection amplitude vs. focal point is shown in Figure 4.16. Again, the reflection amplitude drops when focusing away from the defect face. Nevertheless, the reflection locally peaks at some unwanted locations, for example, around $z = 1.5$ mm for the 50% deep notch. This could be due to the size of the focal point, which is around 1 mm, but in any case, the increase in reflection amplitude is small and local.

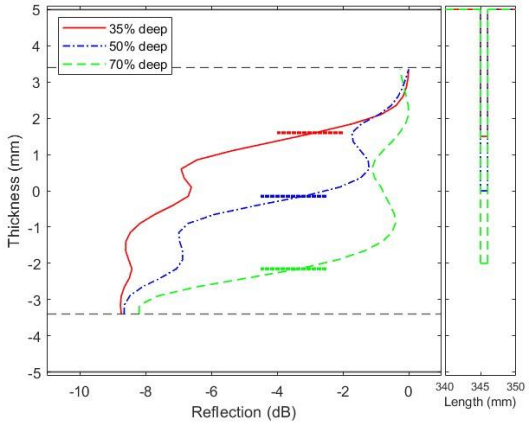

Figure 4.15. Focusing reflection varying the depth of a top surface notch.

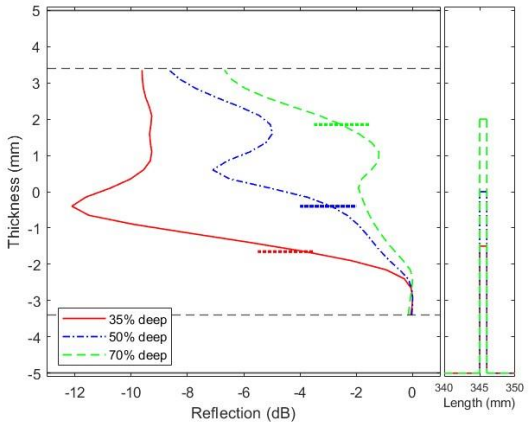

Figure 4.16. Focusing reflection varying the depth of a bottom surface notch.

4.3.2.2. Focusing at internal notches

To further test the technique, focusing was performed at internal crack-like notches. Four notches were simulated, with a vertical length of $\frac{\sigma_f}{2}, \sigma_f, 2\sigma_f$ and $4\sigma_f$. The centre of all notches was at $z = 0$ mm. The reflection amplitude along the thickness direction is shown in Figure 4.17. Although in all cases the highest reflection is obtained at the crack face, accurate estimation of the crack's vertical length using equation (4.8) is possible for crack lengths larger than the focal width. Specifically, cracks with vertical length equal to

$2\sigma_f, 4\sigma_f$ were overestimated with an error of 13% and 15%, respectively, whereas cracks with vertical length equal to $\frac{\sigma_f}{2}, \sigma_f$ were overestimated with 81% and 54% error. The reflection amplitude for the first three notches is very similar.

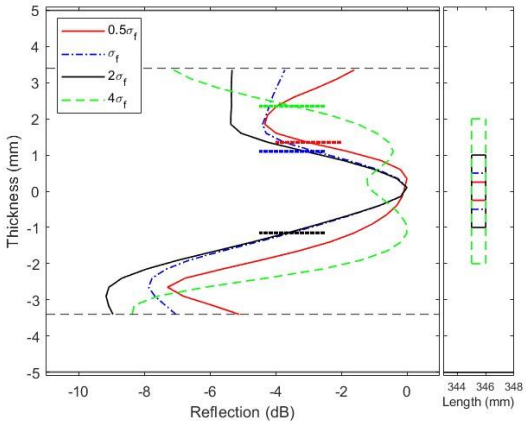

Figure 4.17. Focusing on a crack-like notch of depth $\frac{\sigma_f}{2}, \sigma_f, 2\sigma_f$ and $4\sigma_f$.

4.4. Experimental results

4.4.1. Influence of steering angle and frequency bandwidth

4.4.1.1. Effect of steering angle

The SANR (signal-to-ambient-noise ratio) angle is defined as the angle that maximizes the energy dissipated in the targeted mode. The SANR angle is determined experimentally and should coincide with the theoretical steering angle. The steering angle vs. signal amplitude for the first six higher order modes is shown in Figure 4.18. To extract the amplitude, at each angle, the Hilbert envelope of the signal is obtained, and the maximum of the Hilbert envelope is plotted. For each mode, the amplitude peaks at the SANR angle.

As expected, as the modal order increases, the SANR angles are further separated from each other.

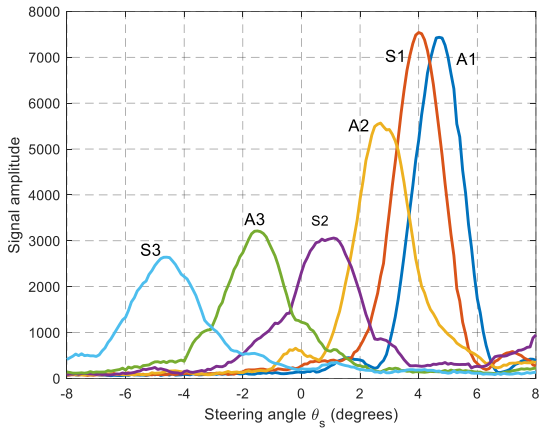

Figure 4.18. Steering angle vs. signal amplitude. The SANR angle is where amplitude peaks.

For single-mode excitation, it is usually beneficial to select an excitation angle slightly different from the SANR angle. The SMNR (signal-to-modal-noise ratio) angle is defined as the angle that maximizes the SMNR,

$$R_{opt} = \frac{M_e}{M_s},$$

where M_e is a mode to enhance and M_s are the selected modes to suppress, which are usually the neighboring modes of M_e. The SMNR angle is not necessarily equal to the SANR angle. However, both angles must have similar values, because if not, the SANR drops significantly, and the excitation is suboptimal. For this reason, the SMNR angle is not allowed to cause an amplitude drop of less than -2.5 dB.

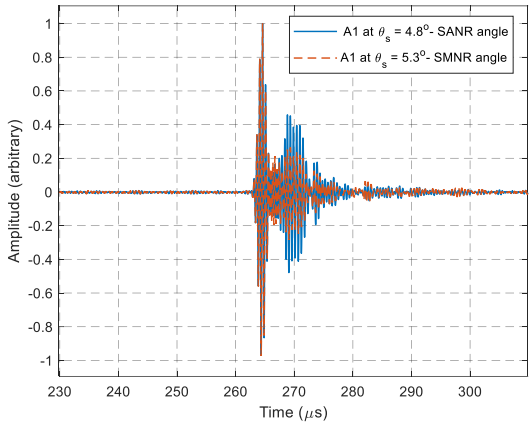

Figure 4.19. A-scan comparing the ratio between mode A1 (targeted) and S1 (unwanted) for different steering angles.

Consider for example mode A1. In contrast to other modes, mode A1 has a single neighbor in the dispersion diagram, namely mode S1 (neglecting the Rayleigh wave). It can be shown that the amplitude ratio A1/S1 is monotonically increasing as the angle of incidence exceeds the SANR angle. However, the overall energy dissipated to mode A1 decreases, and there is a trade-off between single-mode excitation and energy dissipation. A good compromise was found at 5.3 degrees, where the amplitude drop of mode A1 is -2.5 dB and the A1/S1 ratio is significantly improved, as shown in Figure 4.19. A similar analysis was conducted for all modes. The SANR and SMNR angles are given in Table 4.3.

Table 4.3. SANR and SMNR angles and for four modes.

Steering angle \Mode	A1	S1	A2	S2
SANR (deg.)	4.8	4.0	2.7	0.9
SMNR (deg.)	5.3	3.7	2.5	0.9

4.4.1.2. Effect of frequency bandwidth

The frequency bandwidth is a critical factor for guided wave excitation. The centre frequency was kept fixed at 1.9 MHz, thus the bandwidth depends only the number of cycles, see equation (3.6). As shown in Figure 4.19, mode A1 is successfully excited using 3 cycles. However, this is not the case for other higher order modes.

To clarify the ideas that follow, mode S3 is studied. Similar results are obtained by studying A3, A2 or S2. The A-scan of mode S3 is shown in Figure 4.20 (a). Several echoes appear in the signal, with two dominant echoes of approximately equal amplitude. The 2DFFT result is shown in Figure 4.20 (b). Multiple guided wave modes are observed, and two modes are dominant, namely A3 and S3. Initially, it might seem like each mode depicted in the 2DFFT corresponds to a distinct echo in the A-scan. However, this is not accurate, as clarified by the time-frequency graph presented in Figure 4.20 (c). According to the time-frequency plot, all echoes span the same frequency range. Therefore, an echo does not correspond to a mode, since each mode is dominant in a distinct frequency range. In fact, each echo that appears in the A-scan is a combination of all modes. The signal corresponds to a bulk-wave bouncing at the top and bottom surfaces of the plate. These types of waves are used in the M-skip method [23].

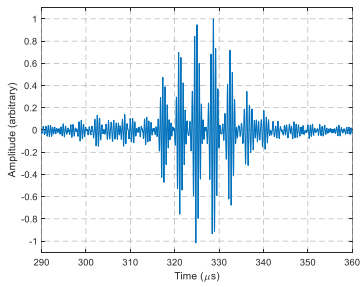

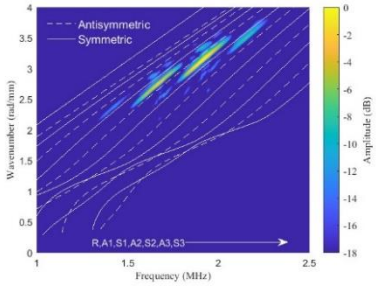

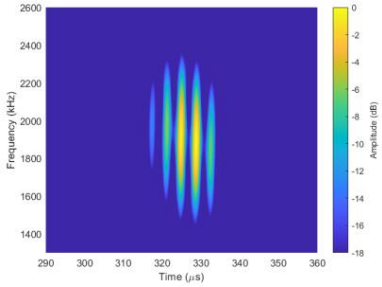

(a) (b) (c)

Figure 4.20. Mode S3 excited with a 3-cycle toneburst centred at 1.9 MHz: a) A-scan b) 2DFFT c) spectrogram.

As the number of cycles increases, the frequency bandwidth becomes narrower, thus only the targeted mode is excited. The spectrogram of mode S3 at 3, 10 and 15 cycles is shown in Figure 4.21. The corresponding bandwidths are 1.27, 0.38 and 0.25 MHz, respectively. As the frequency bandwidth decreases, the excitation becomes single-mode.

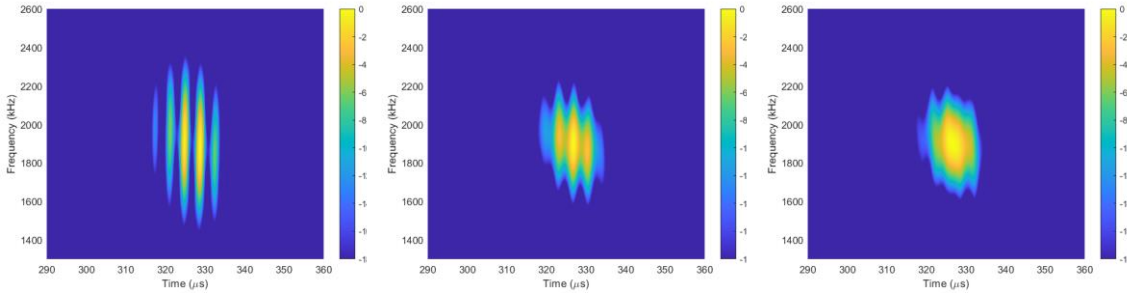

(a) (b) (c)

Figure 4.21. Spectrogram of mode S3 excited with: (a) 3, (b) 10 and (c) 15 cycles.

4.4.2. Experimental determination of the through thickness profiles

To determine experimentally the through-thickness profiles of the modes and time of arrival, a first experiment was conducted in pitch-catch configuration. More specifically, a wedge-mounted 32 element, 1 mm pitch array with a nominal frequency of 2.25 MHz emits plane waves, and these are received by a second 128 element 0.75 mm pitch array mounted at the edge of the 10 mm plate. Only the first 13 elements of the latter array are

in contact with the sample and so only these are used as receivers. A schematic of the experimental set-up is shown in Figure 4.22.

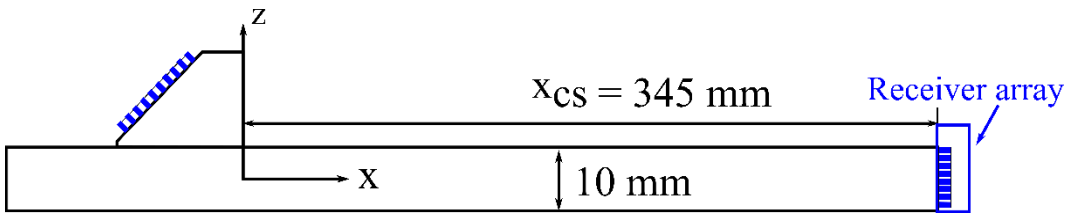

Figure 4.22. Pitch-catch configuration set-up.

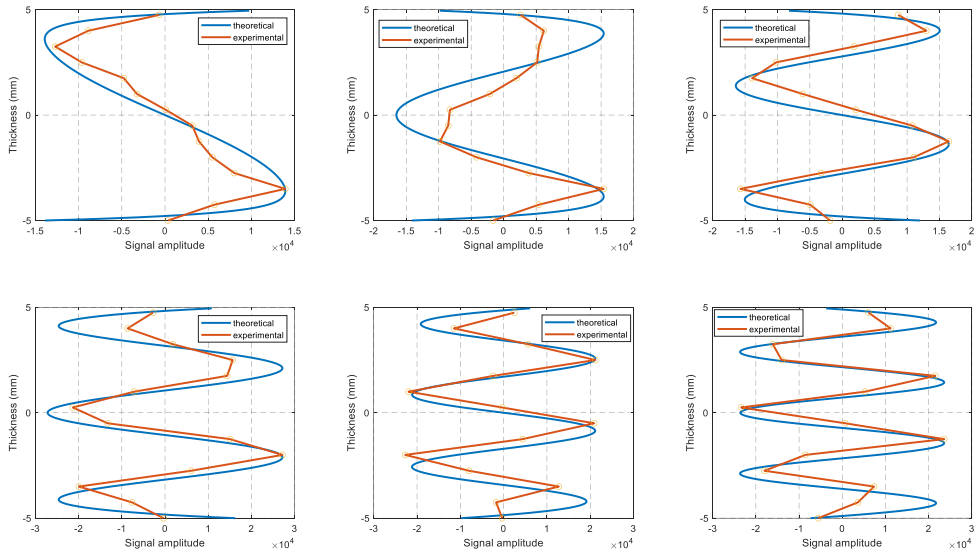

Figure 4.23. Experimental vs. theoretical through-thickness compressional stress profiles.

Figure 4.23 presents the experimental vs. theoretical through-thickness profiles. Note that due to a non-viscous couplant layer between the plate and the receiver, the shear components cannot propagate and so these profiles correspond to the σ_{11} profile. As can be seen, there is very good agreement for all modes. This validates the generation of the targeted modes.

The profile $\sigma_{11}(x_{cs}, z, t)$ is obtained experimentally for each mode. Using σ_{11} and the theoretical ratio of $\frac{\sigma_{11}}{\sigma_{13}}$, the σ_{13} profile is obtained. The time of arrival of each mode at the edge is extracted manually. Specifically, the time of arrival is selected at the time where σ_{11} maximizes. The shear and compressional stress profiles are phased by $\frac{\pi}{4}$, thus this phase difference is added to obtain the time of arrival of σ_{13}.

In contrast to simulations, in this case, the edge of the plate was used to extract the amplitude and time of arrival of each mode. To validate the approach, two separate sets of simulations were conducted to generate parameters that are more easily measured experimentally. Specifically, the displacement fields were extracted at the edge of the material. The distance between the edge and the front face of the wedge was 345 mm. The displacement fields were used instead of stress as σ_{11} vanishes at the edge. Then, the displacement fields were extracted at the bulk of the material at the same distance. Direct comparison of the displacement fields showed no phase distortion above 7 degrees was observed in the waveforms for modes A1, S1, A2 and S2. Modes A3 and S3 showed a phase shift of -39 and -90 degrees, respectively. This means that the estimated time of arrival of the first six modes is sufficiently accurate.

4.4.3. Imaging defects

The experimental set-up for imaging a notch 345 mm away from the front face of the wedge is shown in Figure 4.24. Data was received and acquired with a phased array controller with 64 transmitter and 64 receiver channels. Data was streamed and stored in

a personal computer (PC) for further processing. All experimental parameters match those in Table 4.1.

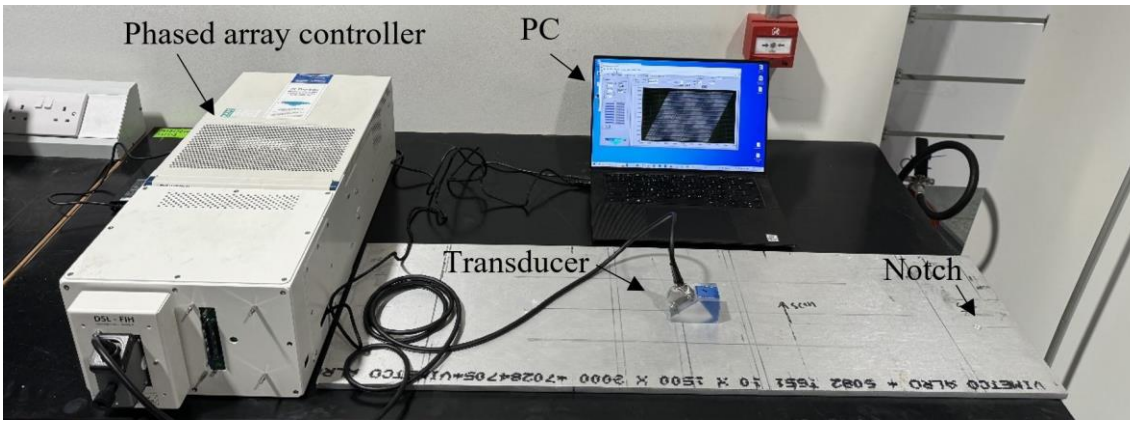

Figure 4.24 Experimental set-up for imaging a vertical notch.

Figure 4.25 (a) illustrates the reflection amplitude when focusing at a 55% deep top surface notch. The length of the notch was kept to approximately $5\lambda_{A1}$. The reflection amplitude is close to 0 dB at the face of the notch. Although the amplitude drops away from the notch, a local peak right below the notch is present, thus the depth of the defect is overestimated with 20% error using equation (4.8). Figure 4.25 (b) shows the reflection amplitude for a 55% deep bottom surface notch. In this case, the amplitude starts dropping slightly earlier. The defect size is underestimated with an error of 7%. To evaluate the effect of adding two higher order modes to the technique, modes $A3$ and $S3$ were added to the sum of equation (4.2). The result is shown in Figure 4.25 (c) and (d). The results are very similar to those in Figure 4.25. This validates experimentally that no significant contribution is gained by adding modes A3 and S3.

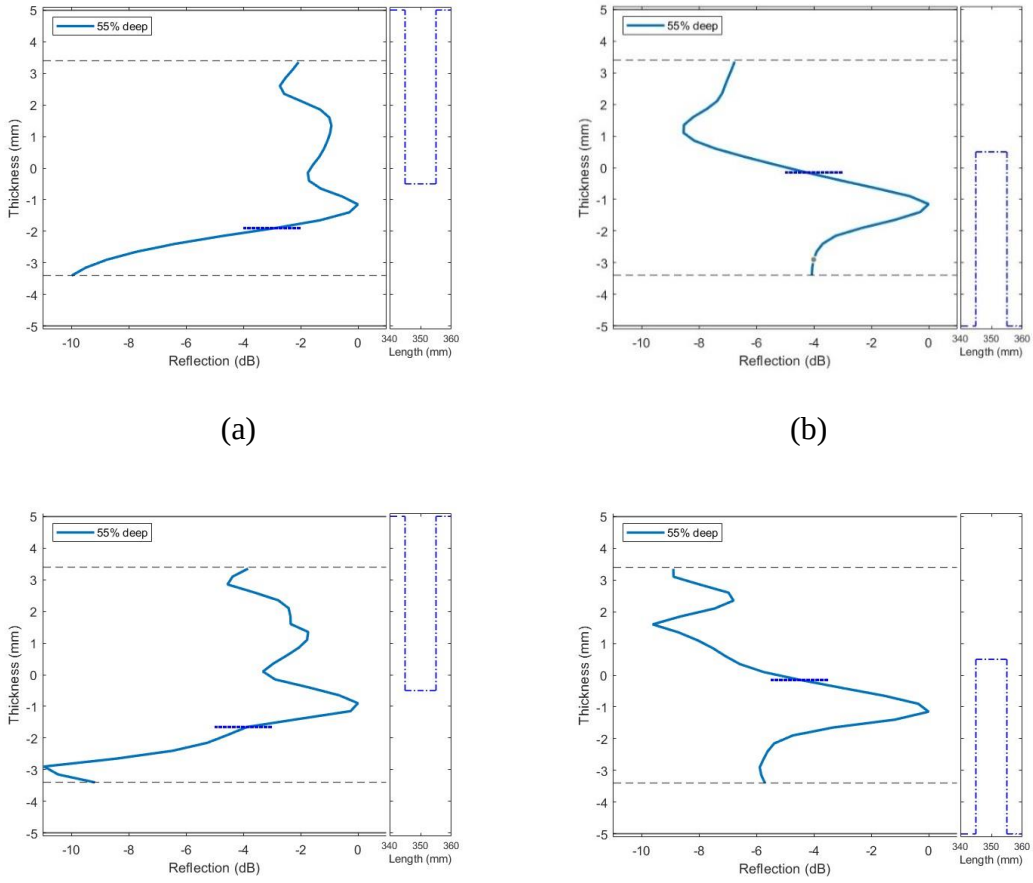

Figure 4.25. Experimental results from through-thickness focusing at a 5.5 mm deep 10 mm diameter (a) top surface notch using 4 modes, (b) bottom surface notch using 4 modes, (c) top surface notch using 6 modes and (d) bottom surface notch using 6 modes.

Compared to simulation results, the error in depth estimation exhibits a slight increase, which can be attributed to various contributing factors. Firstly, small variations in the thickness of the plate may introduce small errors in the estimation of the time of arrival for each mode. Additionally, in contrast to simulations, the time of arrival was determined using the edge of the plate. This introduces small phase shifts in each mode that can affect focusing. Furthermore, positioning discrepancies in the probe between the pitch-catch (see Figure 4.22) and pulse echo (see Figure 4.24) experiments might contribute to issues in

focusing. Also, errors can be introduced in the calculation of the weight functions. The weights are calculated using the analytical through-thickness profiles. Although these agree well with the experimental ones (see Figure 4.23), small differences might lead to errors in the derivation of the weight functions. While these error sources may be individually small, their cumulative impact may either mitigate or amplify the overall error in depth estimation. Overall, the experimental results are in good agreement with simulations.

4.5. Conclusion

A focusing technique using guided waves was developed to image the volume of plate-like structures at locations up to 2-3 m away from the probe. First, emphasis was placed on single-mode guided wave excitation at high frequency-thickness products. Specifically, it was shown that multiple modes can be solely excited using an array probe, provided that both the excitation and frequency spectrums are narrowband. Then, guided wave modes were superimposed to focus on a single point at a specified distance from the transducer and at a desired depth. By weighting the modes, the focal point was swept across the thickness of the plate. It was found that the first four higher order modes yield good focusing results, and adding more modes does not significantly improve the focusing resolution. Analytical computations showed that the focusing ability decreases as the focal point approaches the top or bottom surfaces of the plate. Effectively, a 1.5 mm ‘dead zone’ starts from both the top and bottom surfaces. Inside this region, focusing is not possible. Additionally, thickness variations did not affect focusing, as long as they did not extend significantly, i.e., less than 9 wavelengths for a 1 mm wall loss anomaly. However, the

results indicate that if general corrosion is significant and the general condition of the component is poor, phase errors will result in poorer focusing. Next, simulations were performed. A variety of notches with varying lengths and depths were modelled. Their depth was accurately estimated, provided it was larger than the focal width. Notch length did not affect depth estimation, even for lengths shorter than the wavelength. Finally, experiments were conducted using two 55% deep notches, one on the top surface and the other on the bottom surface. As expected, a high reflection amplitude was obtained when focusing on the face of the notch, whereas focusing on the intact region of the sample led to a drop in amplitude. The error was slightly higher compared to simulation results, but the overall performance was in good agreement with theoretical and numerical results.

Chapter 5

Shear horizontal phased array steering with an EMAT array

5.1. Introduction

In this Chapter, a novel excitation technique for remnant wall thickness quantification is proposed. Specifically, mode SH1 is excited using an array transducer over a wide frequency-wavelength range, namely from 200 kHz-25 mm to 500 kHz-6.5 mm, on a 10 mm thick plate. The elements of an array probe capable of generating shear horizontal forces are phased appropriately to selectively excite mode SH1 without having to alter the transducer configuration. The advantages of the technique follow:

- A wide frequency-wavelength range can be covered using steering, allowing for quantification of deeper defects.
- A feasible transducer size is maintained, around ~75 mm.
- Using electronic steering to phase the array elements, rapid scanning can be achieved.

Although practical, the design and manufacture of a prototype EMAT phased array are beyond the scope of this work. Recent studies [101,102] have shown it is possible to build such an array. To demonstrate the concept of shear horizontal phased array steering experimentally, data was acquired by robotically translating a pair of magnets on top of a racetrack coil, and mode SH1 was constructed synthetically. Nevertheless, a standard array configuration was modelled in simulation, as this was straightforward to implement.

The organisation of this Chapter is as follows. In Section 5.2, shear horizontal phased array steering is examined, and the influence of key parameters on excitation is determined. Simulations are performed in Section 5.3. Mode SH1 is excited on an intact plate across a wide frequency-wavelength range using shear horizontal steering. The directionality of the propagating mode is also examined. Experimental results are presented in Section 5.4. Conclusions are drawn in Section 5.5.

5.2. Shear horizontal mode excitation

In this section, an analytical model of an array generating SH waves is developed, and the principle of steering is extended to shear horizontal. The impact of mode excitability, element width, array pitch, and number of elements on the excitation is studied.

To excite SH guided waves on a sample, a PPM EMAT array is employed. Each array element is modelled as a shear horizontal surface load (parallel to y-axis), as shown in Figure 5.1.

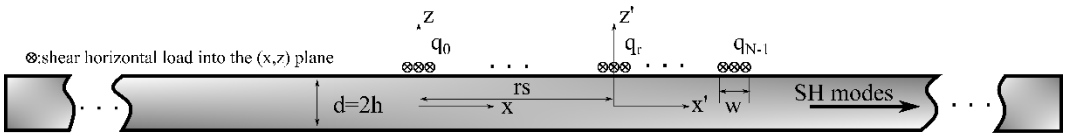

Figure 5.1. N-element array with pitch s and width w on top of a plate with thickness $d = 2h$.

The surface loads represent Lorentz forces applied by the PPM EMAT on the plate. The shear horizontal load exerted by the array on the surface of the plate is expressed according to

$$\underline{F}_{SH}(x,z,t) = \sum_{r=0}^{N-1} \underline{q}_r,\ \underline{q}_r = \left(0, q_r \delta_D(z-h), 0\right)^T.$$

Like the procedure presented in section 3.2, first, the solution for an arbitrary element r of the array is obtained. The r^{th} element is modeled as a shear horizontal surface load q_r of width equal to the magnet width. The shear horizontal load exerted by the element is given by

$$q_r = A_r \hat{g}(x'; w)\hat{h}(t'; M).$$

Projection of $\underline{q}_r$ on a shear horizontal mode m using (2.13), and substitution of (2.14), (2.15) and (2.16) into (2.17) yields the shear horizontal displacement at the top surface of the plate in the following form,

$$u_r^2(x', h, t') = A_s A_r exp\left(i\left(kx' \mp \omega t' \mp \varphi'\right)\right).$$

Similar to the solution for Lamb wave excitation, term $A_s(\omega, k)$ can be decomposed into the product of the excitability function, frequency spectrum and single-element excitation spectrum. The excitability function of the SH modes is given by

$$E^{SH} = \frac{1}{2\omega} \frac{X^2(z=h)^2}{\bar{g}^{SH}(\underline{X}, \underline{X})}.$$

Through combination of equations (2.10) and (2.12), the excitability function appears in the form

$$E^{SH}(\omega; b, h, \rho) = \begin{cases} \frac{1}{2\omega} \frac{1}{\rho b d}, & a = 0 \\ \frac{1}{\omega} \frac{1}{\rho b d}, & a = 1, 2, 3, \ldots \end{cases} \tag{5.1}$$

This means that at the same frequency, the excitability function is constant for all SH modes, except for mode SH0, which has half the excitability of the higher order modes. This is explained in more detail in Appendix B. This is a sharp contrast compared to Lamb wave excitation, where the excitability varies significantly between different modes (see Figure 3.2). The frequency spectrum is identical to that provided in equation (3.5). Moreover, the single-element excitation spectrum is identical to equation (3.7), and assuming a piston-like shear load distribution [103], it turns out that

$$H_{SE}(\lambda, w) = \left| \lambda \frac{\sin(\pi \frac{w}{\lambda})}{\pi} \right|. \tag{5.2}$$

For a fixed width value, $w = w_0$, the single-element excitation spectrum vs. wavelength is illustrated in Figure 5.2 (a). The graph reveals the presence of multiple local minima and maxima within the range $\lambda \in [0, w_0]$. As the wavelength exceeds the element width significantly, $\lambda \gg w_0$, H_{SE} asymptotically approaches w_0. Figure 5.2 (b) shows the excitation spectrum against element width assuming a fixed wavelength value λ_0. This graph can guide the selection of an optimal element width based on a desired wavelength value λ_0. Simple examination reveals that the maxima and minima values of (5.2) occur by setting $w = \lambda_0 \left(n' - \frac{1}{2}\right)$ and $w = \lambda_0 n'$, $n' = 1,2, \ldots \infty$, respectively. For instance, choosing $w = \frac{\lambda_0}{2}$ is an optimal choice, whereas $w = \lambda_0$ leads to poor excitation. In this work, mode SH1 is excited across the wavelength range from 6 to 25 mm. The effect of element width on H_{SE} for $w_0 = 2, 4, 6$ mm is shown in Figure 5.2(c). As expected, selecting $w_0 = 6$ mm significantly attenuates wavelengths around 6 mm. On the contrary, for $w_0 = 2$ mm, H_{SE} is approximately constant across the targeted wavelength range. This behavior is desirable as it ensures an even distribution of energy across wavelengths. An element width of 4 mm yields also acceptable sensitivity across the desired wavelength range. Since 4 mm wide magnets were readily available, this width value was selected in the simulation and experimental sections of this work.

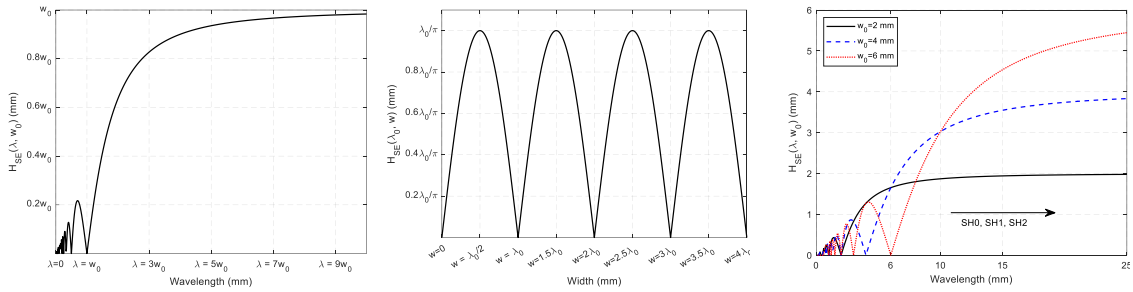

(a) (b) (c)

Figure 5.2. Single-element excitation spectrum vs. (a) wavelength, (b) element width and (c) wavelength for elements widths of 2, 4 and 6 mm.

The total solution is the sum of the local solution of each element after these are expressed in the global frame,

$$u^2 = \sum_{r=0}^{N-1} u_r^2 = A_s A_r e^{j\left(k(x-rs)\mp\omega(t-t_r)\mp\varphi'\right)} = N\mathrm{E}^{SH}\mathrm{FH}_{SE}H_{\pm}e^{j(kx-\omega t\mp\varphi'-\phi')},$$

and assuming uniform amplitudes $A_r = 1$ (since in a phased array EMAT the force pattern does not need to alternating [101]) and a linear time delay law, the excitation spectrum $H_{\pm}$ can be expressed in a form identical to that of (3.10). Therefore, the conditions provided in Table 3.2 related to the number of elements and pitch, apply also for shear horizontal steering with slight modifications. Moving forward, the determination of the time delay constant, number of elements, and pitch for shear horizontal steering is discussed.

To enhance a SH mode, corresponding to a point (ω_e, k_e) in the angular frequency-wavenumber domain, the time delay constant can be set according to (3.11). If excitation at constant phase velocity is employed, equation (3.11) simplifies to

$$\tau = s / c_{pe}. \tag{5.3}$$

Then, a linear time delay law can be applied,

$$t_r = r\tau, \tag{5.4}$$

or

$$t_r = \left(N - 1 - r\right)\tau, \tag{5.5}$$

to steer the forward propagating wave towards the $+x$ or $-x$ axes, respectively. In what follows, a forward propagating wave is defined as one that travels in the steering direction, whereas a backward wave travels in the opposite direction. For instance, using the time delay law (5.5), the forward wave travels in the negative x-direction with respect to Figure 5.1. The x and y axes are selected to be parallel to the wave propagation path and parallel to the shear horizontal direction, respectively.

The selection of the number of elements plays an important role in the purity of the targeted mode. Traditionally, generating a single mode is considered important as it makes signal interpretation and inspection easier [73]. If more than one mode needs to be generated, these can be excited sequentially and analysed independently. The critical parameter for single-mode excitation is the bandwidth of the excitation spectrum [43], which depends on the length of the active aperture of the array. Given a pitch value, the length of the array is primarily determined by the number of elements. The minimum number of elements required for single-mode excitation at -13.5 dB is given by

$$N > \frac{f_e \lambda_e^2}{\Delta c_p^{a-} s}, \tag{5.6}$$

Considering the excitation of SH1, the phase velocity difference between SH1 and SH0 reads

$$\Delta c_p^{SH1-} = c_{pe} - c_T = c_T \left(\frac{2 f_e d}{\sqrt{4 \left(f_e d \right)^2 - c_T^2}} - 1 \right).$$

Taking into account that SH1 is twice as excitable as SH0, condition (5.6) can be halved,

$$N > \frac{f_e \lambda_e^2}{2 c_T \left(\frac{2 f_e d}{\sqrt{4 \left(f_e d \right)^2 - c_T^2}} - 1 \right) s}.$$

The plot of frequency vs. minimum required number of elements to selectively excite SH1 is shown in Figure 5.3. The required transducer length is also shown on the right y-axis. A 5 mm pitch array and a 10 mm aluminum plate with shear velocity 3.1 m/ms were assumed to produce the plot. The relationship is approximately linear above 200 kHz and as frequency increases, single-mode excitation requires more elements.

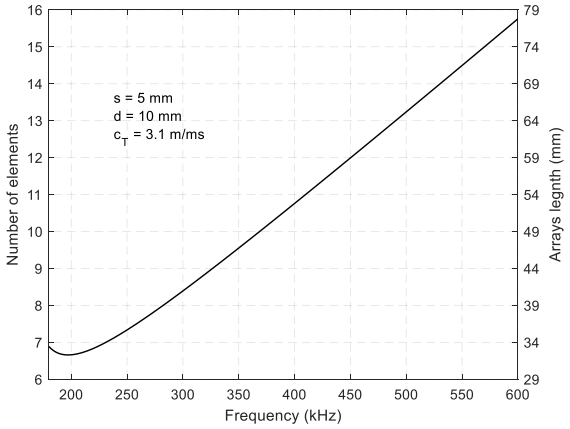

Figure 5.3. Plot of frequency vs. minimum number of elements required to selectively excite SH1 (left y axis) and transducer length (right y axis) for a 5 mm pitch array on a 10 mm thick sample.

Another important parameter for guided wave generation is the pitch value, which determines the directionality of the propagating mode. Unidirectional propagation is desired as signal interpretation becomes easier, especially in plate structures where edge or weld reflections might be misinterpreted. Specifically, to eliminate the backward-travelling wave, condition 3 of Table 3.2 reads

$$s < \frac{\lambda_e}{1 + c_{pe} / c_T}. \tag{5.7}$$

For example, when mode SH1 is targeted in the range of 300-500 kHz, $c_{pe}/c_T \approx 1$ and thus $s \lesssim \lambda_e/2$.

Conditions (5.3), (5.6) and (5.7) arise directly from the properties of the excitation spectrum, thus they do not depend on element width. Although counter-intuitive, this means condition (5.7) is valid even if $w \geq s$.

5.3. Finite element simulations on an intact plate

Finite element simulations were developed using OnScale in a 2D domain. The mesh size was set to 0.1 mm, which resulted in more than 10 nodes per wavelength when the smallest wavelength in the model is considered [99]. The timestep was set to 10 ns, which is lower than the time required for the fastest wave to travel through an element of the given size [100].

The simulation setup for the excitation of SH1 on an intact plate is shown in Figure 5.4. Specifically, the middle cross-section of a 10 mm thick aluminium plate was modelled, whereas a 15-element array with a 5 mm pitch was placed on the top surface. For simplicity, the array elements are illustrated as rectangular blocks (in blue colour). They exert shear horizontal loads in the direction perpendicular to the (x, z) plane, similar to Figure 5.1. Shear horizontal wave propagation on a 2D model is possible in OnScale by applying the 'grid sh' command to the 2D grid. The elements were 4 mm wide, as this was the width of the magnets used in the experimental setup. A 120 mm monitoring line was placed at the top surface, approximately 0.5 m from the last array element. The surface velocity in the shear horizontal direction was recorded, as this is the field sampled by an EMAT. The model was 1.5 m long to avoid edge reflection echoes.

Each array element generated a piston-like shear horizontal load. The array elements were phased appropriately to enhance SH1 mode. The excitation signal $h(t; M)$ was an M-cycle sinusoid. Multiple simulations were conducted, varying the centre frequency of the excitation signal from 200 kHz up to 500 kHz with a 25 kHz step. The number of cycles

is given by $t_b = M / f_e$ and was determined based on the frequency bandwidth of the signal, see equation (3.6). Specifically, the cycles were determined so that the main lobe width of the frequency spectrum is around 100 kHz, to have sufficient overlapping in the frequency domain between excitations. The number of cycles is shown in Table 5.1. All cycles were rounded to integers, as the function generator used in the experimental setup did not allow for half-cycle excitation.

At each simulation, SH1 was targeted at (f_e, c_{pe}) and the time delay constant was determined according to equation (5.3). Element 1 was initially fired to steer the ultrasonic beam in the positive direction of the x-axis.

The simulated array had an aperture length of 74 mm, which is above the minimum required length for single-mode excitation in the range of $200 - 500$ kHz (see Figure 5.3). Adding more elements should further enhance the purity of SH1, but at the cost of having a larger size probe.

Table 5.1. Sinusoidal excitation signals at varying frequencies and cycle numbers to maintain constant bandwidth between excitations

No. Cycles	4	4	5	5	6	6	7	7	8	8	9	9	10
Centre frequency (kHz)	200	225	250	275	300	325	350	375	400	425	450	475	500
Bandwidth (kHz)	100	113	100	110	100	108	100	107	100	106	100	105	100

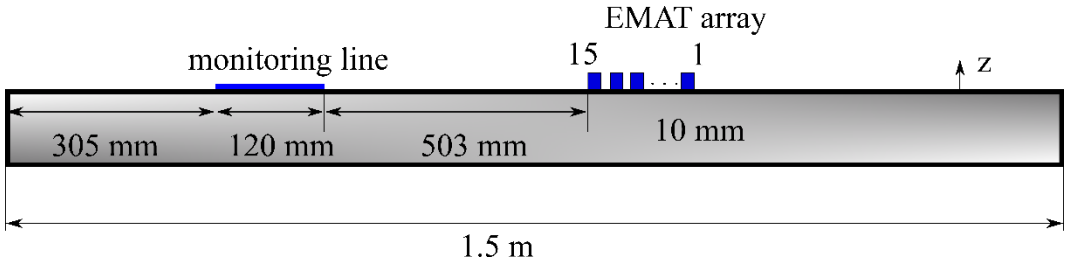

Figure 5.4. 2D simulation model. A 5 mm pitch 15-element array is simulated on top of a 10 mm thick aluminium plate.

Figure 5.5 presents 2DFFT [91] maps when targeting mode SH1 at four different frequencies, namely 200, 300, 400, and 500 kHz. In all cases, energy is centred at SH1 around the excitation frequency. The results show that with a proper selection of the array's length, it is possible to selectively excite SH1 over a wide range of frequencies using shear horizontal steering. 2DFFT maps at intermediate frequencies are similar. Note that although emphasis was placed on generating SH1, other modes could also be targeted, such as SH0 or SH2, using the appropriate time delay law (5.3) ensuring that the excitation length is sufficient.

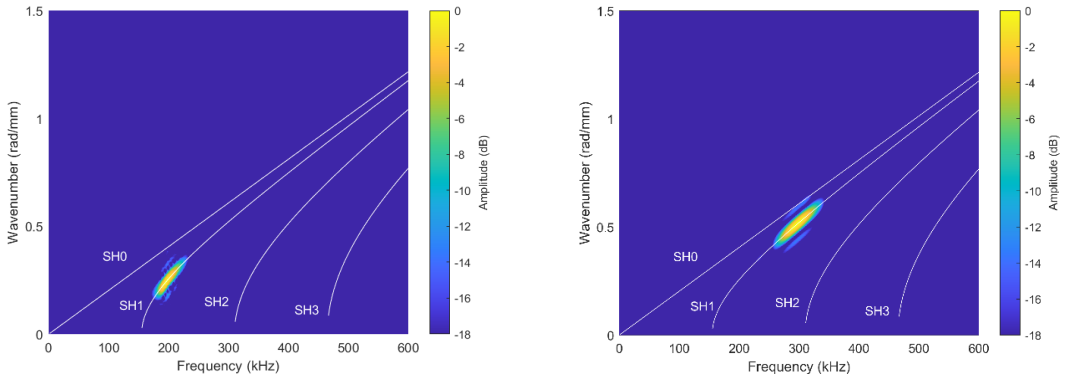

(a) (b)

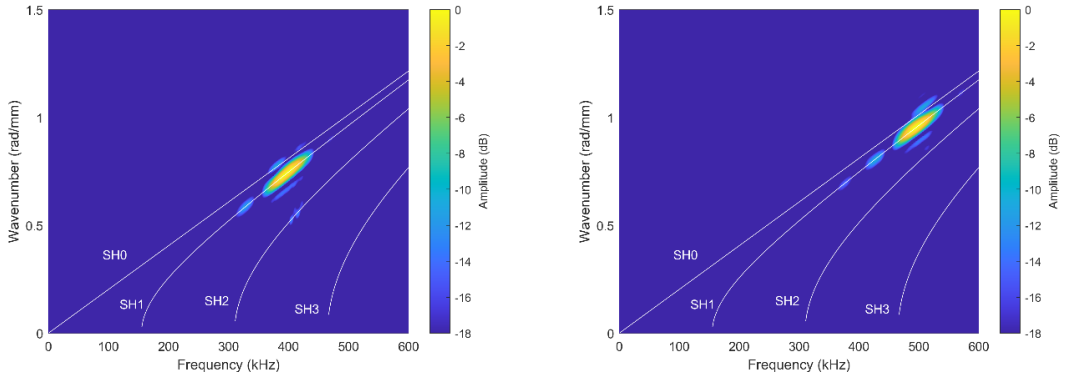

(c) (d)

Figure 5.5. 2DFFT maps of signals obtained from simulation using a 15-element 5 mm pitch array targeting SH1 at: (a) 200 kHz, (b) 300 kHz, (c) 400 kHz, (d) 500 kHz. The dispersion curves of a 10 mm thick aluminium plate are shown in white.

In practical applications, it is common to use a single-element transducer for signal reception, and thus a 2DFFT analysis is not possible. In these cases, wall loss quantification is performed after post-processing the acquired data to produce a spectrogram [59,61]. This way, data from multiple acquisitions can be represented in a single time-frequency plot. Figure 5.6 displays the spectrogram result composing all excitation configurations. To produce the spectrogram map, A-scans were captured by a monitoring point 575 mm away from the centre of the first element of the array. The short time Fourier transform [13] was employed to obtain the sub-spectrogram for each A-scan. Each entry (time-frequency point) of the final spectrogram was selected as the maximum of the corresponding entries in the sub-spectrograms. The spectrogram before amplitude normalisation of the A-scans is shown in Figure 5.6 (a). Although mode SH1 is selectively excited at the desired frequency range, more energy is distributed around $250 - 350$ kHz. This can be attributed to different properties of mode SH1 across the examined frequency-wavelength range, such as excitability, dispersion, and the effect of the single-element

excitation spectrum. Figure 5.6 (b) displays the spectrogram after amplitude normalisation, such that the peak of the A-scans is set to 1. Energy is uniformly distributed across the desired frequency range. Due to the large range of frequencies covered by the new excitation technique, wall loss defects up to 65% can be quantified rapidly.

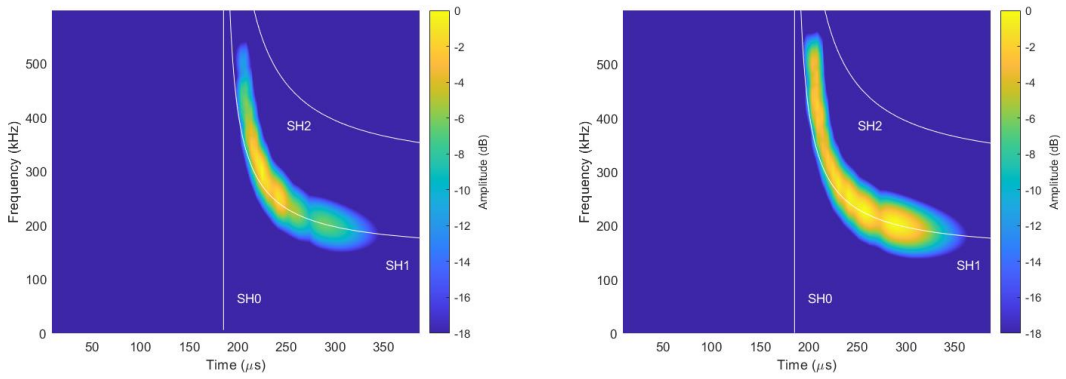

(a) (b)

Figure 5.6. Spectrogram showing the generation of SH1 in a wide frequency-wavelength range, from 200 kHz-24.5 mm to 500 kHz-6.5 mm: (a) before amplitude normalisation, (b) after amplitude normalisation. The time-of-flight-frequency curves at a distance of 575 mm are displayed in white.

Next, the directionality of mode SH1 is examined. For this purpose, a separate set of simulations was conducted. The setup remained identical to the previous simulations, with the exception that the last element (element 15) of the array was fired first. This way, the backward-travelling (with respect to the steering direction) wave is captured by the monitoring line. The four excitation cases discussed in Figure 5.5 are also considered here. These correspond to travelling waves with centre frequency-wavelength values of 200 kHz-24.53 mm, 300 kHz –12.07 mm, 400 kHz-8.41 mm, and 500 kHz-6.52 mm. Therefore, condition (5.7) reads

$$s < 9.5,\ 5.55,\ 4.03 \text{ and } 3.18 \text{ mm},$$

respectively. This indicates that the excitation of SH1 at 200 and 300 kHz will be unidirectional with a 5 mm pitch array. However, unidirectionality at 400 and 500 kHz requires a pitch value of around 3 mm. Note that the unidirectionality of the propagating mode is particularly important not only for remnant wall thickness quantification but also in robot localisation studies [83,104,105] using EMATs.

Figure 5.7 illustrates 2DFFT maps when steering in the $-x$ direction (see Figure 5.4). The 0 dB reference value is consistent with that of Figure 5.5. As expected, no significant energy is observed to propagate at 200 and 300 kHz, as depicted in Figure 5.7 (a) and (b), respectively. However, at higher frequencies, specifically at 400 and 500 kHz, wave propagation is bidirectional, as modes SH2 and SH3 propagate in the $+x$ direction, as seen in Figure 5.7 (c) and (d), respectively. The results are in good agreement with condition (5.7).

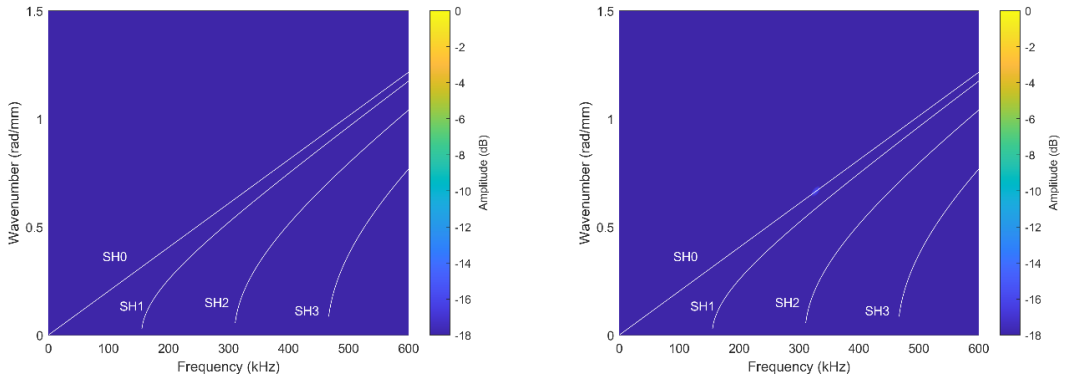

(a) (b)

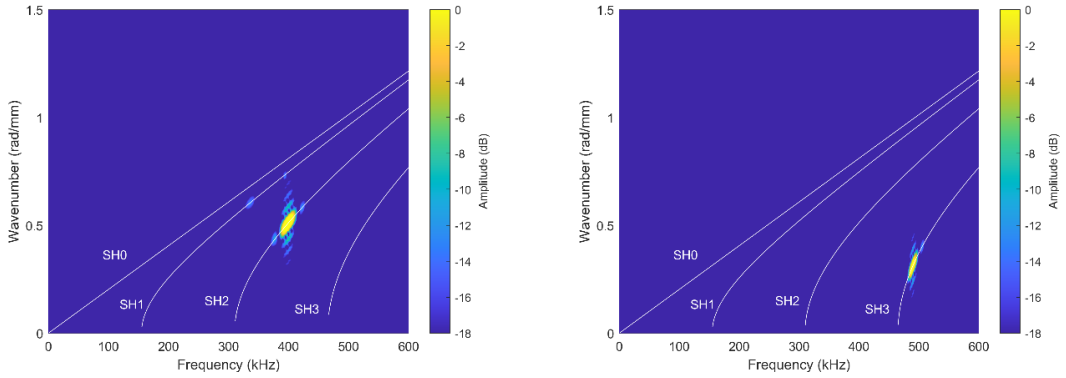

(c) (d)

Figure 5.7. 2DFFT maps of signals obtained from simulation using a 15-element 5 mm pitch array when steering in the $-x$ direction at: (a) 200 kHz, (b) 300 kHz, (c) 400 kHz, (d) 500 kHz. The dispersion curves of a 10 mm thick aluminum plate are shown in white.

5.4. Experimental generation of SH1 on an intact plate

In this section, experimental results are presented. Specifically, to validate the discussed improved excitation technique, SH1 is swept in the range of $200 - 500$ kHz on an intact plate.

A proof-of-concept system was built, as shown in Figure 5.8 (a). Data was acquired on the intact portion of a 10 mm thick aluminium plate (grade 6082-T6). Two Lorentz force EMATs [106] were used in a pitch-catch configuration. Specifically, two identical PCB coils were used for reception and transmission. The coils are positioned so that the eddy current $\underline{J_e}$ induced by them flows along the x-direction. A 2x6 3D printed frame was placed on top of each coil, and two magnets were placed in a single row, whereas all other rows remained empty, as shown in Figure 5.8 (b). The magnet width is 4 mm and the static magnetic field $\underline{B}$ generated by the magnets is along the z-direction. The exact coil

and magnet dimensions are given in Table 5.2. The receiver's frame was glued to the sample at a distance around 180 mm from the left edge. The receiver was a single-element transducer with an element width of 4 mm. The transmitter's frame was mounted at the end tool of a Meca500 Six-axis robot arm [107], 557 mm away from the receiver (centre-to-centre distance of the receiver-transmitter magnets). The transmitter generated Lorentz forces,

$$\underline{F}_L = \underline{J}_e \times \underline{B},$$

parallel to the y-direction. The frame was robotically translated towards $+x$-axis along the coil for 74 mm with a 5 mm increment, to mimic a 15-element 5 mm pitch array. At each increment step (15 in total), 13 excitation signals were generated and received (see Table 5.1). This way, the full matrix (15 Tx / 1 Rx) was acquired at each frequency. Excitation signals were generated with a RITEC RPC-4000 [108]. The received signals were fed into the same hardware where a $100 - 600$ kHz bandpass filter was applied to reduce noise, and after pre-amplification, the signals were digitised using a PicoScope 5000a series [109], which was triggered by the RITEC. Signals were averaged 64 times to improve the signal-to-noise ratio. Although translating a single magnet row was time consuming and done for the purposes of this experiment, such an approach may be practical under certain circumstances, for example if the dragging force due to a full-magnet EMAT must be reduced. All measuring equipment, including the robotic arm, was controlled using LabVIEW.

Table 5.2. Dimensions of racetrack coil and permanent magnets

Coil total region	Coil linear region	Coil number of turns	PCB thickness	Magnet width	Magnet length	Magnet thickness
116 mm x 41 mm	74 mm x 41 mm	23	0.25 mm	4 mm	20 mm	6 mm

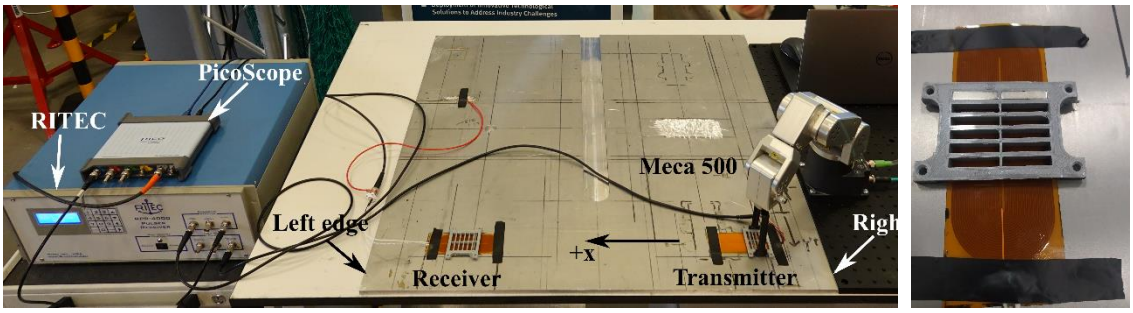

(a) (b)

Figure 5.8. Experimental set up: (a) pitch-catch configuration, (b) single-row EMAT.

The acquired data was synthetically post-processed to construct mode SH1. Specifically, the received signals were time-shifted and added. For instance, consider an excitation toneburst with a centre frequency of 350 kHz (see Table 5.1). As the transmitter frame is translated, 15 signals are captured by the single-element receiver. To construct mode SH1, the time delay constant is determined according to equation (5.3),

$$\tau = \frac{5mm}{3457\,m/s} = 1.45\ \mu s.$$

To steer mode SH1 towards the $+x$ or $-x$ directions, the raw signals are shifted according to equations (5.4) or (5.5), respectively, and then added.

Figure 5.9 shows schematically the possible wave propagation paths. These are labeled ‘D’, ‘LE’, ‘RE’ and ‘RLE’ to describe the direct, left-edge reflection, right-edge reflection, and right-left-edge paths, respectively. In what follows, echoes are labelled by the mode and propagation path they followed. For example, SH1-RE denotes an SH1 wave that travels in the $-x$ direction and reflects at the right edge to reach the receiver.

Figure 5.9. Schematic illustration showing wave propagation paths in pitch-catch configuration.

Figure 5.10 displays the received post-processed A-scans when targeting SH1 at centre frequencies of 200, 300, 400, and 500 kHz. The ultrasonic beam was steered in the $+x$ direction, and the time axis limits were set to show the direct and left edge reflection echoes. Figure 5.10 (a) shows the A-scan when targeting SH1 at 200 kHz. The spreading of wave-packets SH1-D and SH1-LE due to dispersion is visible. Mode SH0 is also present, but the amplitude difference is around -17 dB. Figure 5.10 (b) and (c) display A-scans targeting the same mode at 300 kHz and 400 kHz, respectively. SH1 is less dispersive, which is the expected behavior at higher frequencies. Mode SH0 is around -18 dB at 300 kHz and -13 dB at 400 kHz. The difference in drop amplitude of SH0 is due to the higher modal density exhibited at higher frequencies. Figure 5.10 (d) shows the A-scan when targeting SH1 at 500 kHz. Although similar to the previous A-scans, these echoes have a somewhat irregular shape. This signal is actually a cluster [6,82] of modes SH1 and SH0. These modes have very similar group velocities and thus cannot be

distinguished at the examined propagation length. To shed light on this matter, a simulation was conducted where two monitoring points captured the shear horizontal velocity component 557 mm and 1.26 m away from the first element of the array probe. The centre frequency and number of cycles were set to 500 kHz and 10 to replicate experimental conditions. The resulting A-scans are shown in Figure 5.11. As expected, at 557 mm, the two modes are indistinguishable. As the propagation distance increases to 1.26 m, two distinct wave-packets are visible. Although mode SH0 is present, SH1 mode is 13 dB higher; therefore, in the following analysis, the influence of mode SH0 is neglected, and the excitation is considered single-mode.

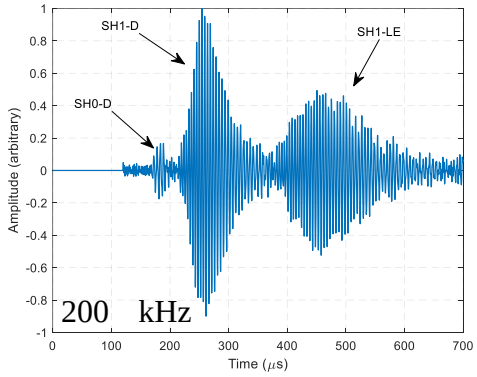

(a)

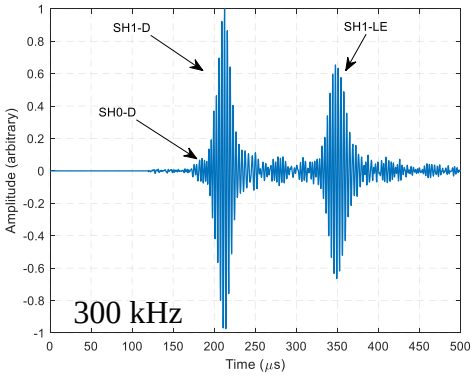

(b)

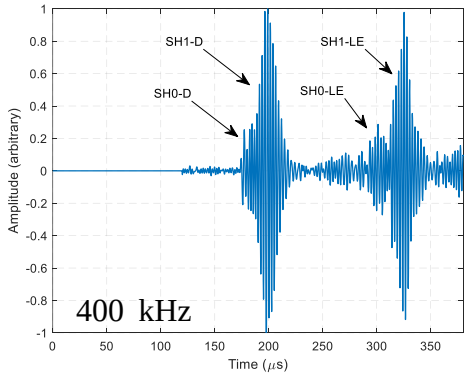

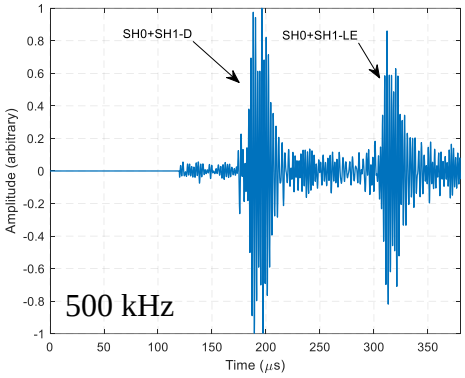

(c) (d)

Figure 5.10. Experimental A-scans using synthetic steering. SH1 is targeted at: (a) 200 kHz, (b) 300 kHz, (c) 400 kHz, (d) 500 kHz. The first echo and the reflection from the left edge are visible.

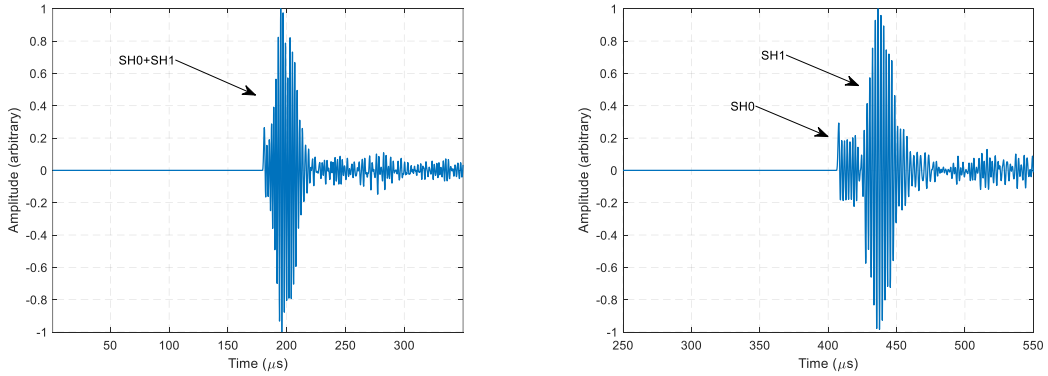

(a) (b)

Figure 5.11. A-scan of simulated data at a distance of: (a) 557 mm; modes SH0 and SH1 are superimposed, (b) 1.26 m; modes SH0 and SH1 are separated.

The spectrogram utilising all acquired data is shown in Figure 5.12. The processing was identical to the one described in Figure 5.6. Note that although mode SH0 is present in Figure 5.10, it is not visible in the spectrogram since signal energy instead of signal amplitude is plotted. The reflected echo was removed for better observation. This result proves experimentally that mode SH1 can be selectively excited in a frequency range from 200 to 500 kHz on a 10 mm thick plate using the present approach. This is key to the successful application of the technique.

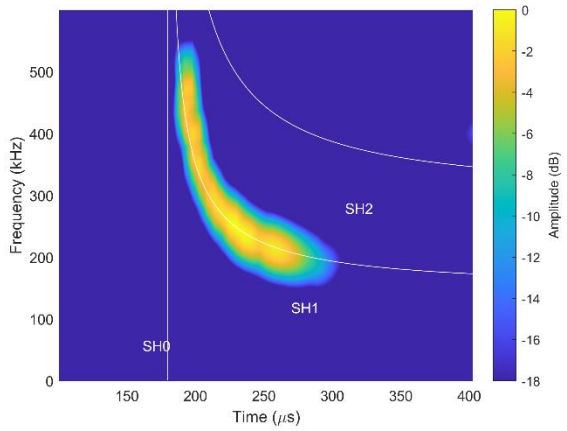

Figure 5.12. Experimental spectrogram showing the generation of SH1 over the frequency range 200-500 kHz.

Next, the directionality of SH1 for the four cases discussed in Figure 5.7 is examined. To gain a better understanding of the effect of pitch value on wave propagation, an additional experiment was conducted. Specifically, the transmitter magnet was translated by a smaller step, namely 3 mm. This means that the pitch value was smaller than element width, which is uncommon in arrays due to geometry constraints. Nevertheless, such a choice is valid, since there is no physical constraint requiring $s > w$. In fact, condition (5.7) is independent of element width. The total excitation length was maintained at 74 mm. Synthetic steering in the positive (towards the receiver) and negative directions was performed, by phasing the r^{th} element of the array according to equations (5.4) and (5.5), respectively, where τ was selected according to (5.3) to target mode SH1. At 200 and 300 kHz, the propagation is unidirectional for both pitch values, namely 5 and 3 mm, thus these results are not presented. However, at 400 kHz and 500 kHz, condition (5.7) is satisfied only when a 3 mm array is employed.

Figure 5.13 presents the synthetically reconstructed A-scans when exciting at centre frequencies of 400 and 500 kHz and using two arrays with different pitch values, namely 5 and 3 mm. At all times, mode SH1 was targeted. Figure 5.13 (a) shows the received signals at 400 kHz for a 3 mm pitch array. In this case, condition (5.7) is satisfied, and propagation is unidirectional. As expected, when steering in the $+x$ direction, the direct and left edge reflection echoes are visible. Note that no reflection from the right edge appears, as no significant energy dissipates in the $-x$ direction. Two echoes are also visible when steering in the opposite direction. These echoes result from the forward travelling wave-packet, which reflects first at the right and then at the left boundary. The discussed four echoes are present in all sub-figures. Figure 5.13 (b) illustrates the effect of increasing the pitch of the array to 5 mm. In this case, wave propagation is bidirectional, and mode SH2 (see Figure 5.7 (c)) is excited in the backward direction. For example, when steering in the $+x$ direction, more than two echoes appear in the (blue) signal, from the right and right-left edge reflections of SH2. Figure 5.13 (c) shows results when exciting at 500 kHz using a 3 mm pitch array. As expected, wave propagation is unidirectional. However, this changes when employing a 5 mm pitch array, see Figure 5.13 (d). Specifically, when steering towards the $-x$-axis, mode SH3 (see Figure 5.7 (d)) is excited and travels in the $+x$ direction, thus is directly captured by the receiver probe. The mode is highly dispersive and has a low group velocity, around 1.14 m/ms, thus it arrives later than the right and left reflections of the forward travelling wave, which travel at 2.95 m/ms. The discussed results are in good agreement with condition (5.7).

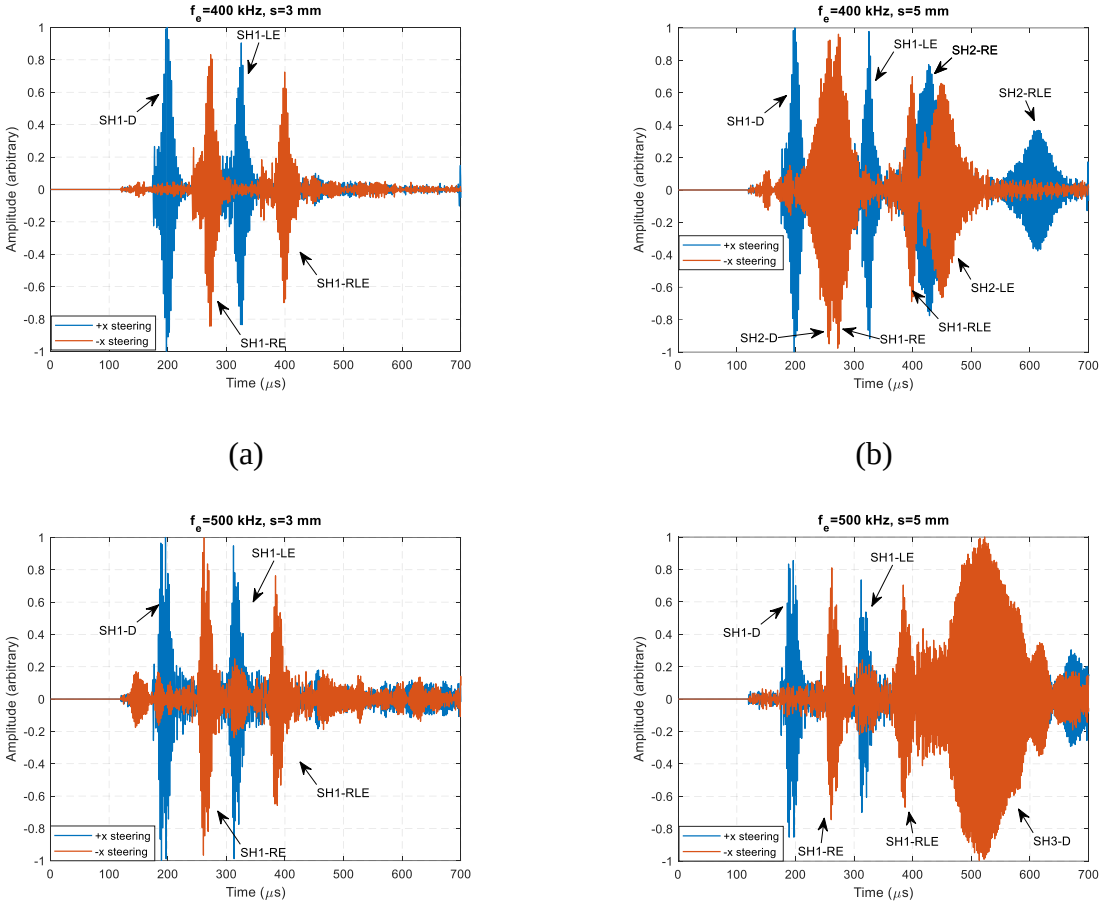

Figure 5.13. Experimental A-scans when steering synthetically in the $+x$ (in blue) and $-x$ (in red) directions. (a)-(c): A 3 mm pitch array is utilised, targeting SH1 mode at: (a) 400 kHz, (c) 500 kHz. Wave propagation is unidirectional (b)-(d): A 5 mm pitch array is utilised, targeting SH1 mode at: (b) 400 kHz, (d) 500 kHz. Wave propagation is bidirectional.

5.5. Conclusion

First, to understand the influence of key parameters on shear horizontal phased array steering, an analytical model was derived. It was found that the array's length, pitch, and element width have the same effect on shear horizontal steering as they do on Lamb wave steering. However, in contrast to Lamb wave modes, the excitability function is constant

for all SH modes at the same frequency, except for mode SH0, which has half the excitability of the higher order modes. The lower excitability of SH0 is advantageous, as mode SH1 can be selectively excited with a smaller aperture size. Then, the generation of SH1 in an intact area was examined. Using an array with an element width of 4 mm and a 74 mm aperture length, mode SH1 was solely excited over a wide frequency-wavelength range, namely from 200 kHz-25 mm to 500 kHz-6.5 mm, both in simulation and experiment. Finally, the unidirectionality of the generated wave-packet was investigated, and it was shown that unidirectionality at higher frequencies requires an array with a pitch equal to or smaller than 3 mm. This was in accordance with the analytically derived condition (5.7).

Chapter 6

An excitation technique for remnant wall thickness quantification using SH modes

6.1. Introduction

Recently, wall thickness quantification using a frequency-based analysis has attracted the attention of the research community [54,59,61]. The technique uses guided waves, utilising the cut-off frequency of higher order modes. More specifically, a higher order mode is generated, travelling circumferentially in pipes or along a straight line in plates. The mode is excited over a frequency-wavelength range, which depends on the nominal thickness of the test sample and the capability of the transmitter and receiver probes. A split frequency occurs between the reflected and transmitted waves from the maximum wall loss area, allowing the cut-off frequency and wall thickness to be determined. If multiple wall thinning defects are present along the propagation path of the mode, the technique reports the most severe wall loss [59]. To reduce mode conversion, it is preferable to operate in a region with few modes [61]. Therefore, usually the first higher

order mode is selected, namely A1 for Lamb waves or SH1 for SH waves. Commonly, SH1 is preferred, as it does not leak into non-viscous fluids that may be in contact with the sample [10]. The mode can be excited using piezoelectric transduction [110–112] or EMATs [113]. Although piezoelectric transducers are recognised for their efficiency and high signal-to-noise ratio, EMATs are often the preferred choice as they are non-contact.

In this Chapter, wall loss quantification is performed using the cut-off principle of SH1. In Section 6.2, wall thickness quantification using a frequency-based analysis is briefly discussed. In Section 6.3, finite element simulations to quantify the minimum remaining wall thickness of a series of smooth wall thinning defects are performed. Experimental results on a machine defect representative of corrosion with 65% maximum wall loss are shown in Section 6.4. In Section 6.5, key conclusions are drawn.

6.2. Minimum remaining wall thickness quantification

In this section, the fundamental principle for wall thickness quantification using the cut-off frequency of higher order SH modes is outlined. Since this topic is explained in detail in [61], only the key principle of operation is discussed briefly.

Among many properties, i.e., phase velocity, group velocity, wavelength, etc., a higher order mode exhibits a cut-off frequency-thickness product, i.e., a minimum frequency-thickness value, below which the mode does not exist. Given a thickness value d, the cut-off frequency of an SH mode can be calculated according to

$$f_{cut\text{-}off} = nC_T / 2d. \quad (6.1)$$

Moreover, given a frequency value f, the cut-off thickness of a mode is given by

$$d_{cut\text{-}off} = nC_T/2f \tag{6.2}$$

Figure 6.1 shows a 10 mm thick plate with a wall thinning defect. The minimum remaining wall thickness is 3.5 mm; thus, using equation (6.1), the cut-off frequency of mode SH1 at the wall thinning region is 440 kHz. This means components of mode SH1 with frequency below 440 kHz cannot propagate through the defect area and are thus reflected. Given that the defect depth is not known beforehand, the process of quantifying the minimum remaining wall thickness is based on exciting SH1 at a wide range of frequencies, using multiple [59] or a single [61] capture. Once the cut-off frequency is determined, the remaining wall thickness can be obtained using equation (6.2).

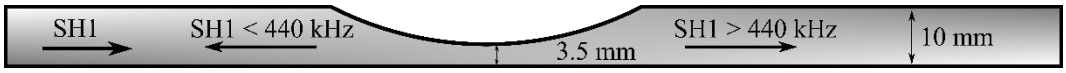

Figure 6.1. Wall loss quantification using the cut-off principle of SH1 mode. A gradual 6.5 mm wall thinning defect on a 10 mm thick plate is schematically illustrated. Only frequencies above the cut-off propagate through the defect, whereas lower frequencies are reflected.

The preceding analysis has certain preconditions that must be fulfilled. First, no abrupt thickness changes must occur [57,58], so that mode conversion effects can be disregarded. If the defect has tapered edges, the success of the method depends on the slope of the tapered region [57]. Specifically, assuming a defect with step edges (90° slope) and remaining wall thickness below the cut-off thickness, mode SH1 converts to SH0 when entering the defect region and back to SH1 as it leaves the defect, whereas only a small fraction of energy is reflected. On the contrary, when defect edges are gradually inclined, mode conversion effects are reduced. For example, when edges are inclined by 30° and

5°, mode conversion is restricted to around one-third and near zero of the energy of the incident wave, respectively, so the technique can be applied [57]. Next, the defect size in the shear horizontal direction (width) must be several wavelengths larger than the beam width [59], making the technique mostly appropriate for the detection of relatively large corrosion patches. Last, in certain cases, operation at elevated temperatures is required, for example, in pipelines carrying high temperature steam. EMATs can be designed to tolerate high temperatures, even up to 500℃ [114]. However, wall loss quantification becomes more challenging in such cases due to the decrease in shear wave velocity with increasing temperature [115]. Nevertheless, since the distance between the transmitter and receiver pair is known, mode SH0 can be first emitted to estimate the shear wave velocity value on an intact sample region.

6.3. Finite element simulations

The interaction of SH1 with three defects with 65%, 40% and 20% wall loss is presented in what follows. The simulation parameters are identical to the ones presented in section 4.3.

A 2D model featuring a smooth surface defect profile was created and is shown in Figure 6.2. This model can be understood as the cross-section of a full 3D model, with the defect extending sufficiently long in the y-direction. Since phased array steering offers excitation of SH1 in a wide frequency-wavelength range, a 65 % wall thinning defect was simulated. The defect profile exhibits a circular shape with a total length of 76 mm. The remaining wall thickness was 3.5 mm, leading to the cut-off frequency of SH1 at 440 kHz. Two

points, one before and one after the defect, recorded the shear horizontal velocity components of the reflected and transmitted waves, respectively. The plate was 1.3 m long. All other parameters used in the simulation remained consistent with those outlined in Section 5.3.

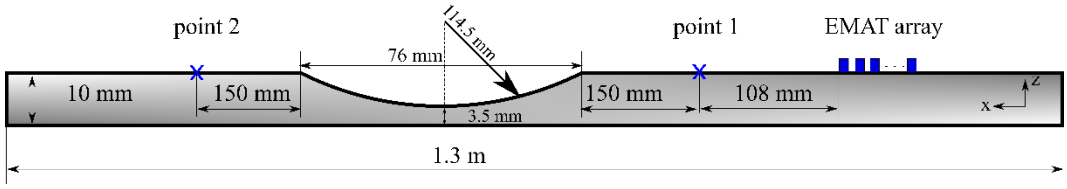

Figure 6.2. 2D simulation model of a 15-element 5 mm pitch array and a 6.5 mm deep defect. Two points captured the reflection (point 1) and transmission (point 2) of SH1.

Figure 6.3 illustrates the spectrogram results acquired by the two monitoring points. Figure 6.3 (a) pertains to data collected by point 1 (see Figure 6.2). As expected, only frequencies below 440 kHz are reflected. The first echo is also visible, as the wave passes point 1 before it encounters the defect. Figure 6.3 (b) relates to the data obtained by point 2 (see Figure 6.2). Only frequencies above the SH1 cut-off pass through the defect area. The spectrograms were calibrated so that the energy of a spectrogram captured on an intact area at the same propagation distance is equally distributed across all frequencies (see Figure 5.6). By analysing these results, the cut-off frequency can be determined, which in turn allows the calculation of the remaining wall thickness using equation (6.2). The present result shows it is possible to accurately quantify the thickness of a 65% wall thinning defect using mode SH1. In fact, defects closer to 70% wall loss may be quantified; however, as the cut-off frequency approaches 500 kHz, the transmitted waves cover a shorter frequency range, making determination of the split frequency more difficult.

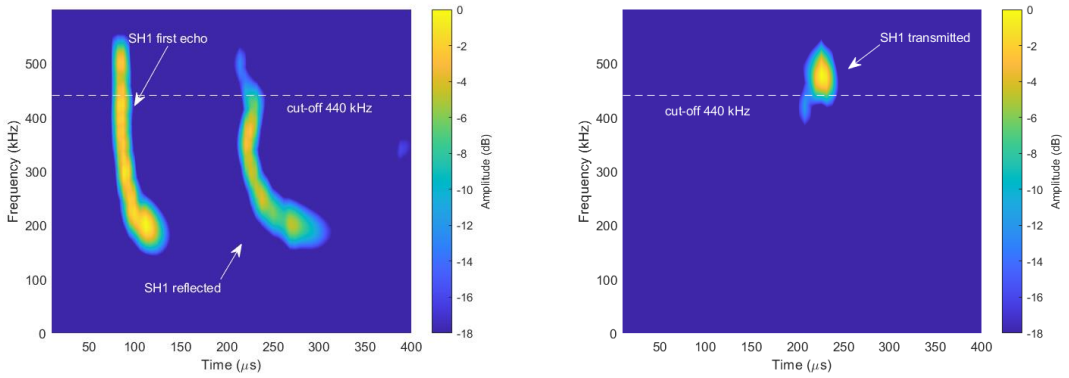

(a) (b)

Figure 6.3. Spectrogram result of received signals at: (a) point 1 (reflected wave), (b) point 2 (transmitted wave). The frequency content between the reflected and transmitted waves is separated by the cut-off frequency line at 440 kHz.

To further validate the approach, two more wall thinning defects were simulated. The set-up was identical to that of Figure 6.2, however, the minimum remaining wall thickness of the defects was chosen at 6 mm (40% wall loss) and 7.5 mm (25% wall loss), thus the length of the defect was 60 mm and 48 mm, respectively. The reflected and transmitted spectrogram maps related to the 40% wall loss defect are shown in Figure 6.4 (a) and (b). For better observation, the first echo received by point 1 is not shown in Figure 6.4 (a). The cut-off frequency is at 258 kHz, separating the reflected and transmitted waves in the frequency domain. Similar results are shown for the 25% wall loss defect, as shown in Figure 6.4 (c) and (d). In this case, the cut-off frequency is at 206 kHz, close to the lower frequency limit, but the reflected and transmitted frequencies are still well-separated. In both cases, accurate wall loss quantification is possible.

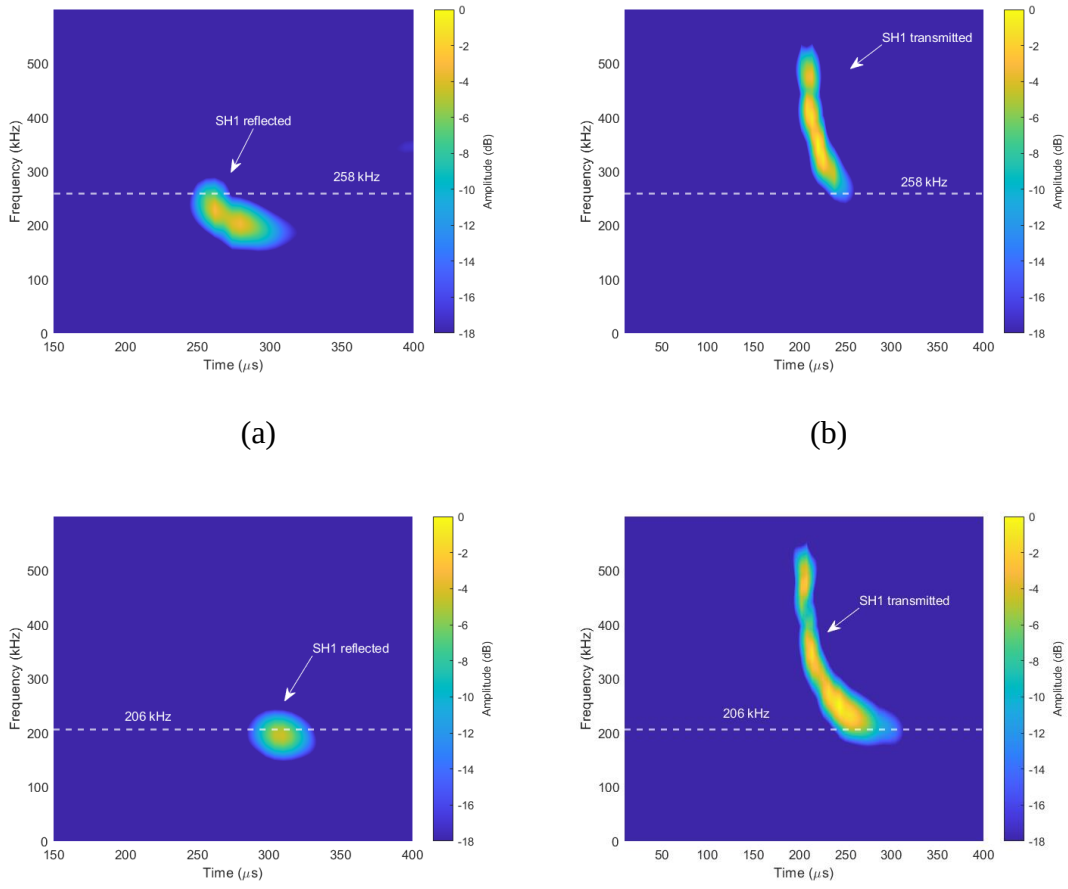

Figure 6.4. Spectrogram maps of: (a) reflected waves at 40% wall loss, (b) transmitted waves at 40% wall loss, (c) reflected waves at 25% wall loss, (d) transmitted waves at 25% wall loss.

6.4. Experimental results

In this section, experimental results are presented. The interaction of SH1 with a corrosion-like defect is presented. This is done mainly for completeness purposes. In fact, the interaction of SH1 with corrosion like defects is a well investigated topic. Specifically, it is known that wall loss quantification using the cut-off principle of mode SH1 is accurate when tested against gradual thinning defects but does not yield precise results in the

presence of sharp pits, which introduce abrupt thickness changes. A review of published experimental work testing the approach is presented in Table 6.1. Note that in all studies wall loss defects are up to 50%.

Table 6.1. A summary of publications related to the interaction of SH1 with wall thinning defects

Defect type	Wall loss quantification utilising the cut-off property of SH1	Ref.
Machined- smooth tapered edge defect	✓	[57]
Machined- steep tapered edge defect (abrupt thickness change)	✗	
Machined-dish shaped- 2 defects	✓	[61]
Corrosion under pipe support- laboratory trial	✓	[59]
Corrosion under pipe support- blind trial-6 defects	✓	

6.4.1. Wall loss quantification

Further laboratory experiments were conducted to determine the minimum remaining wall thickness of a machined defect. Unless otherwise stated, all parameters to generate and receive data were identical to the ones provided in Section 5.4.

First, a surface defect was machined. Given that the interaction of SH1 with smooth wall thinning flaws is well understood and has been studied experimentally [61], in an effort to test the technique against more realistic corrosion patches [116,117], a non-smooth defect was made. The defect was manually machined using a plasma arc gauging technique and trimmed using a cut-off wheel mounted on a power rotary tool. The defect is 60 mm long and 120 mm wide. The minimum remaining wall thickness was difficult to control precisely during the machining of the defect. After laser scanning [118], it was found to be 2.5 mm. This wall thickness reduction was caused by a very localised thickness change that extended less than 1 mm along the y-axis. The wall loss that extended sufficiently [59] along the y-axis, approximately for 80 mm, was found to be 6 mm. Figure 6.5 (a) displays the defect profile in a section parallel to the y-axis passing through the centre of the defect. Figure 6.5 (b) displays the profile of the defect in a section parallel to the x-axis, again passing through the centre of the defect.

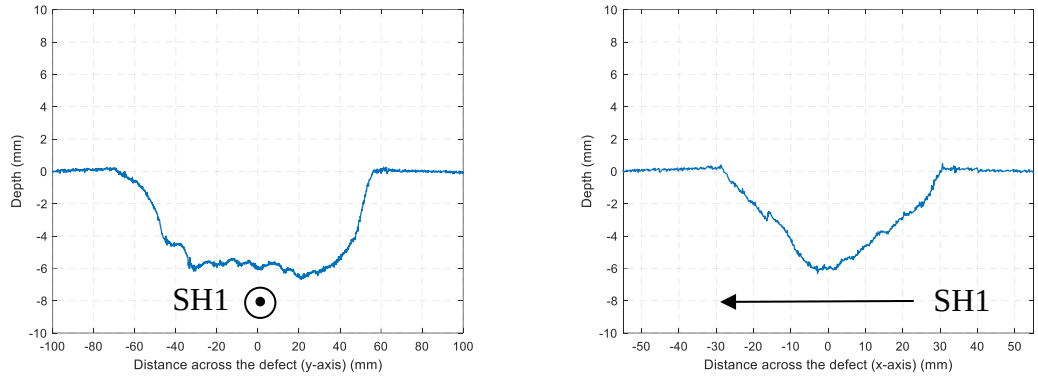

(a) (b)

Figure 6.5. Defect cross section along: (a) y-axis (normal to propagation direction) and (b) x-axis (parallel to propagation direction).

Next, data in pitch-catch and pseudo pulse-echo configurations was acquired, as shown in Figure 6.6. In both cases, the initial position of the robotic arm located the transmitter magnets around 132 mm away from the centre of the defect. This position corresponds to the first element of the array. The rest of the array elements were realised as the arm moved towards the defect. At each configuration, two datasets were obtained, mimicking a 3 and 5 mm pitch array. Figure 6.6 (a) illustrates the configuration of the experimental setup used to monitor transmitted waves. The receiver is approximately 316 mm away from the first element of the array. Steering was performed in the $-x$ direction, so that the length of the propagation path of mode SH1 is around 930 mm. This is similar to the path length mode SH1 traveled in the experiment described in Section 5.4, when path 'LE' is considered. The reconstructed A-scans related to the defect case were calibrated (using the peak amplitude of 'SH1-LE' intact case signals) as explained in Figure 6.3. Therefore, if no defect was present, energy would be uniformly distributed across the 200-500 kHz frequency range in the spectrogram maps. A pseudo pulse-echo configuration to monitor

waves reflected from the defect is shown in Figure 6.6 (b). The receiver was placed behind the transmitter, 176 mm away from the first array element. Steering was performed in the $+x$ direction, and data was calibrated based on intact signals corresponding to propagation path SH1-D.

In Figure 6.7, three different propagation paths related to pseudo pulse-echo configuration are illustrated. The defect reflection and defect-right edge reflection paths are called 'DR' and 'DRR', respectively. The direct patch from the transmitter to the receiver probe is called 'D' (as in Figure 5.9), which can occur even when steering towards the $+x$ direction if wave propagation is bidirectional. The propagation paths related to Figure 6.6 (a) are as given in Figure 5.9.

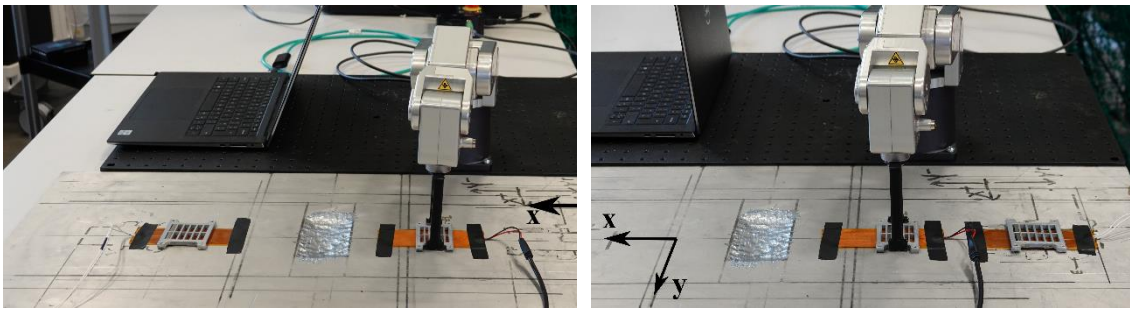

(a) (b)

Figure 6.6. Experimental set up: (a) pitch-catch configuration, (b) pseudo pulse-echo configuration

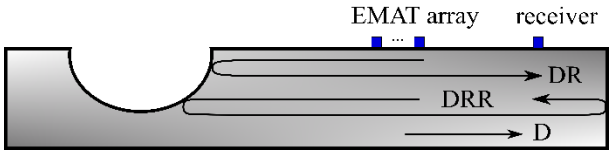

Figure 6.7. Schematic illustration showing wave propagation paths in pseudo pulse-echo configuration.

Finally, after post-processing, spectrogram results were obtained. These maps were produced from reconstructed A-scan signals, as described in Section 6.3. The spectrogram utilising a 3 mm pitch array is shown in Figure 6.8. Figure 6.8 (a) shows the time-frequency content of waves reflected from the defect. The reflection from the right edge is also visible. Figure 6.8 (b) displays the spectrogram of the transmitted waves. Direct comparison of the two graphs makes it clear there exists a split frequency around 440 kHz. The split frequency was determined manually. Figure 6.9 displays spectrogram maps when a 5 mm pitch array is utilised. Figure 6.9 (a) shows the spectrogram of the pseudo pulse-echo configuration. Modes SH3 and SH2 are directly transmitted to the receiver around 500 and 400 kHz, respectively, as wave propagation is bidirectional at these frequencies. In fact, mode SH3 completely masks the useful characteristics of the signal at -18 dB. For this reason, the reflection is plotted at a -40 dB threshold, to make mode SH1 visible. The presence of unwanted modes makes it difficult to determine the cut-off frequency. This emphasizes the importance of unidirectional propagation, especially in cases where the receiver is located behind the transmitter or when inspecting in areas close to large reflectors, such as plate edges. Figure 6.9 (b) presents the spectrogram of the transmitted waves and is similar to Figure 6.8 (b). This is expected, as the cut-off frequency of SH2 and SH3 at 3.5 mm is 885 kHz and 1.3 MHz, respectively, which means these modes cannot pass through the defect at the $200 - 500$ kHz operating frequency range.

Using the cut-off frequency value that was obtained after analysis of Figure 6.8 and equation (6.2), the minimum remaining wall thickness can be estimated at 3.5 mm. The

error in quantification is 1 mm. This is expected, as the minimum remaining wall thickness (2.5 mm) occurs due to a very localised thickness change, extending less than 1 mm along the y-axis, thus it cannot be detected by the developed technique [59]. The defect sufficiently extends along the y-axis with a remaining wall thickness of 4 mm (see Figure 6.5 (a)). The error with respect to this value is 0.5 mm, or 5%, which is within the technique's expected error range [59].

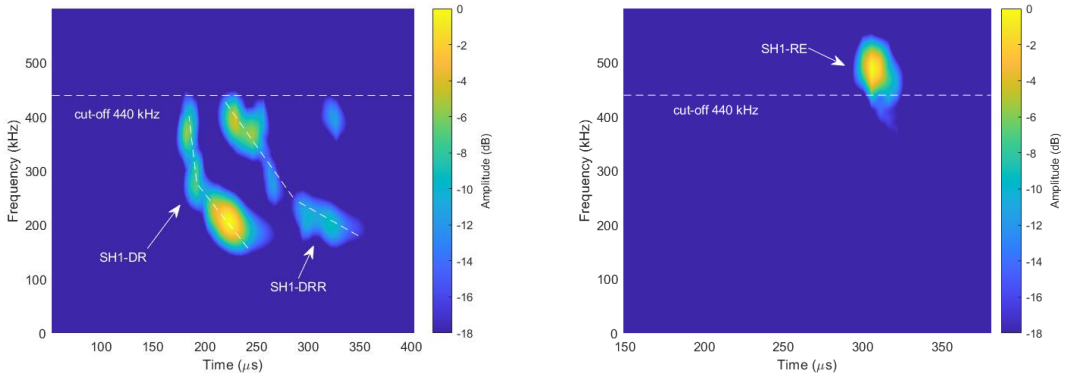

(a) (b)

Figure 6.8. Experimental spectrogram utilising a 3 mm pitch array: (a) reflected SH1 waves below 440 kHz, (b) transmitted SH1 waves above 440 kHz.

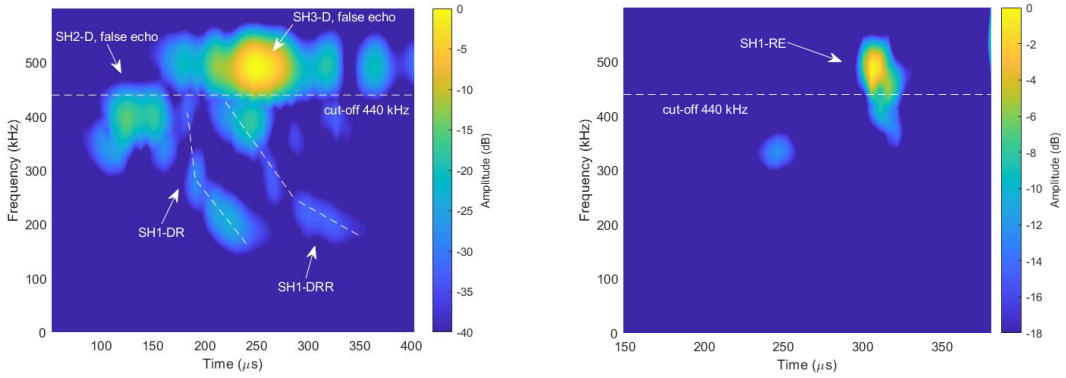

(a) (b)

Figure 6.9. Experimental spectrogram utilising a 5 mm pitch array: (a) reflected SH1 waves below 440 kHz and modal noise due to loss of unidirectionality, (b) transmitted SH1 waves above 440 kHz.

6.5. Conclusion

An improved excitation technique for minimum remaining wall thickness quantification was presented. The approach utilised a transmitter array to sweep mode SH1 across a wide range of frequencies. A 65% wall thinning defect was successfully quantified in simulation, whereas further experiments with a more realistic corrosion-like defect validated the approach. This illustrates that the present technique allows quantification of deep defects, while maintaining a feasible transducer size. The quality of the acquired spectrograms utilising a 3 mm array allowed the split frequency to be determined manually with good accuracy both in simulation and experiments. However, in certain cases, determining the cut-off frequency can be challenging, and thus a more robust way of determining the split frequency is required.

Chapter 7

Conclusion and Future Work

7.1. Conclusion

This thesis has proposed advanced techniques for inspection at inaccessible locations using medium-range guided waves, shedding light on their applications, limitations, and potential avenues for improvement. Instead of single-element probes, linear arrays were used to emit and receive ultrasonic waves, which allowed the implementation of sophisticated processing algorithms and enabled accurate sizing of defects.

First, emphasis was placed on the development of a theoretical framework for guided wave excitation in plates and plate-like structures. A set of conditions were derived, acting as guidelines for the proper selection of the number of elements and pitch. Specifically, satisfaction of conditions (3.24) and (5.7) ensure unidirectional propagation for Lamb wave and SH modes, respectively. These conditions determine the pitch of the array and are similar to the conditions derived for bulk wave steering to ensure the elimination of grating lobes. Next, given the pitch value, condition (5.6) decides the minimum required number of elements for single mode excitation. Note also that the element width is

physically constrained to be smaller than the pitch value. Therefore, these conditions can assist in the design of arrays optimised for guided wave generation.

Next, an imaging technique was developed, termed Lamb wave focusing, to accurately size sharp defects, such as pitting. Specifically, a 2.25 MHz linear array probe was mounted on an angled wedge to selectively excite modes A1, A2, S1 and S2 using phased array steering. The modes were weighted and superimposed to focus the ultrasonic energy at a specific depth. By altering the weights, the focusing depth was swept throughout the thickness of the structure. Upon interaction with the defect, the reflected ultrasonic waves are received by the same probe, and the amplitude of the reflection coefficient is recorded.

Using the technique, the depth of a series of vertical notches in simulation and experiment was accurately quantified. The technique loses its focusing ability when the focusing depth is very close to the top or bottom surfaces. In fact, for a 10 mm thick plate, a 1.5 mm dead zone occurs close to the surfaces of the component. This means defects can be classified into three categories: $< 15\%$, $15 - 85\%$, and $> 85\%$ deep. A defect shallower than 15% can be detected but cannot be sized. Nevertheless, such defects are usually a minor threat and are not an immediate risk for structural failure. A defect with a depth in the range 15-85% can be accurately sized. Moreover, a defect deeper than 85% would be classified as a $> 85\%$ defect; however, its precise depth cannot be accurately determined. Nevertheless, defects above 85% are severe, and action is required regardless of their exact depth.

Compared to existing techniques, which can detect defects but struggle to quantify depth information accurately, Lamb wave focusing offers the unique advantage in providing

depth size capabilities. This distinguishing feature positions the technique as a valuable advancement, offering a more comprehensive understanding of structural integrity by seamlessly combining defect detection with accurate depth quantification.

Despite its promising attributes, Lamb wave focusing is not without challenges. Specifically, small thickness variations from the nominal value can introduce inaccuracies in estimating the time of arrival, thereby influencing the effectiveness of the focusing process. This means that the technique is not expected to work well for components that are corroded to a large extent. Indeed, it is assumed that the general condition of the component under inspection is good. Moreover, the technique can size only pitting or pitting-like defects. If the pit is located inside a wall thinning area, the accuracy of the method depends on the extent of the corrosion. Moreover, the technique assumes a that single pit defect is present. The performance of the algorithm when multiple pits aligned with the probe is not investigated. Nevertheless, note that in all the above cases defect detection is possible, yet sizing accuracy is poor.

Finally, a frequency-based technique was developed to quantify the minimum remaining wall thickness of gradual wall thinning corrosion defects, such as localized gradual wall loss corrosion. An EMAT array was used to emit mode SH1 over a wide frequency range, namely from 200 to 500 kHz, with a 25 kHz frequency step. At each frequency, a separate excitation was performed, and mode SH1 propagated towards the corrosion area and interacted with the corrosion defect. The defect acts like a frequency filter, passing only frequency components above the cut-off frequency. Therefore, a pitch-catch configuration is used, and the frequency content of the reflected and transmitted waves is monitored.

The range of defect depth that can be quantified depends on the ability of the technique to sweep over a wide frequency range. For the 200-500 kHz range achieved in this thesis, gradual wall thinning defects can be classified into three categories: $< 25\%$, $25 - 65\%$, and $> 65\%$ maximum wall loss. Defects shallower than 25% (minor defects) cannot be detected. Defects with a maximum wall loss of 25-65% can be accurately quantified. A defect with a maximum wall loss of more than 65% would be classified as a $> 65\%$ defect, but wall loss cannot be quantified. The 65% limit can be increased by increasing the maximum excitation frequency. For instance, a 200-600 kHz sweep would uplift the maximum wall loss limit approximately to 75%. However, single-mode excitation of SH1 at 600 kHz would require a larger active aperture and a smaller pitch value.

Utilising an array instead of a single-channel EMAT offers several advantages. Using beam steering, the upper frequency limit can be increased. Single-channel frequency-based techniques can detect gradual wall thinning defects with a maximum wall loss of about 50%. Moreover, these techniques do not have the ability to excite a unidirectional SH wave. Unidirectional propagation simplifies signal interpretation, especially if edges are presented, in which case edge reflections from the opposite side of the transducer may arrive at the same time as the quantification signal and complicate signal interpretation.

For the technique to work well, wall loss corrosion defects are assumed to be gradual and pitting-free. If pitting is present, it cannot be detected or measured. In this case, a combination of both frequency and amplitude-based methods could potentially improve the probability of detection and the accuracy of the remaining wall thickness estimation.

7.2. Future Work

Future work aims to make the developed techniques more robust and mature. This requires further studies on each technique individually as well as a proposal on how these supplementary techniques can be combined to offer a holistic inspection plan for the inspection of hidden corrosion.

Lamb wave focusing would benefit from the following. First, the presence of multiple defects aligned with the probe needs to be addressed. For instance, if two vertical pits are aligned with the probe, currently only the first can be accurately estimated. Potentially, an algorithm that compensates for the presence of the first defect and can accurately size other defects is possible to implement. Moreover, a study on the effect of defect width would be beneficial, employing full 3D simulations and the manufacture of more defects. Finally, the technique can be extended to different guided waves, such as SH modes.

Minimum remaining wall thickness estimation with an EMAT array can also benefit from two main advancements. First, remnant wall thickness quantification depends on the accurate estimation of the cut-off frequency, which could be interpreted by a trained technician; however, this would be error prone. Therefore, the development of a signal processing algorithm for robust cut-off frequency estimation is significant. Second, manufacturing of a prototype phased array PPM EMAT to demonstrate the approach using an array driver is crucial, since the proposed cut-off frequency technique requires the use of an array. In this thesis, a single element was used, which was robotically translated with a specific pitch to mimic a physical array probe. This way, each robot position corresponds

to activating a different array element. Signals were recorded and post-processed synthetically. Although the procedure is valid, the acquisition is slow. An alternative is to use a PPM EMAT array to speed up the acquisition process.

The outcomes of this research open the way for the use of new advanced inspection techniques. Future endeavours will focus on enhancing their robustness and maturity. Specifically, the developed techniques will be trialled on industrial sites, and a detailed comparison between the developed and existing techniques will be made. An ambitious proposal is to integrate these advanced techniques into a holistic inspection plan. This holistic approach can enable the detection and mitigation of hidden corrosion, marking a significant stride towards ensuring the integrity of critical infrastructure.

Appendix A

Through-thickness displacement profiles of Lamb wave modes

The through-thickness displacement profile of the antisymmetric Lamb wave modes appears in the following form,

$$X^{1(a)}(z) = -i\left(\bar{a}_1 \sin(\bar{p}z) + \bar{a}_2 \sin(\bar{q}z)\right)$$
$$X^{3(a)}(z) = \left(\bar{a}_3 \cos(\bar{p}z) + \bar{a}_4 \cos(\bar{q}z)\right)$$

where

$$\bar{a}_1 = 2\sin(\bar{q}h),\ \bar{a}_2 = -\frac{k^2 - \bar{q}^2}{k^2}\sin(\bar{p}h)$$
$$\bar{a}_3 = 2\frac{\bar{p}}{k}\sin(\bar{q}h),\ \bar{a}_4 = \frac{k^2 - \bar{q}^2}{\bar{q}k}\sin(\bar{p}h).$$

For symmetric Lamb wave modes, the through-thickness displacement profile is given by

$$X^{1(s)}(z) = -i\left(\bar{s}_1 \cos(\bar{p}z) + \bar{s}_2 \cos(\bar{q}z)\right)$$
$$X^{3(s)}(z) = \left(\bar{s}_3 \sin(\bar{p}z) + \bar{s}_4 \sin(\bar{q}z)\right)$$

where

$$\bar{s}_1 = 2\cos(\bar{q}h),\ \bar{s}_2 = -\frac{k^2 - \bar{q}^2}{k^2}\cos(\bar{p}h)$$

$$\bar{s}_3 = -2\frac{\bar{p}}{k}\cos(\bar{q}h),\ \bar{s}_4 = -\frac{k^2 - \bar{q}^2}{\bar{q}k}\cos(\bar{p}h).$$

Appendix B

On the excitability of mode SH0 compared to higher order SH modes

In Section 5.2, it was stated that mode SH0 has half the excitability of the higher order SH mode. This statement is investigated in detail in what follows.

First, a finite element simulation was conducted where a single element of width $w = 0.1$ mm generated shear horizontal forces on top of a 10 mm thick plate. The element width was selected sufficiently small to reduce the effect of H_{SE}, as shown next. The excitation signal in time was a 20-cycle Hann-windowed toneburst at a centre frequency of 400 kHz. The shear horizontal displacement component at a cross section positioned 900 mm away from the single element was recorded, and modes SH0 and SH1 were monitored. The plate was sufficiently large, to avoid edge reflections.

Based on analytical results developed in Section 5.2, the surface displacement ratio of modes SH0 and SH1 can be expressed in the following form,

$$\frac{A_s\left(\omega_{SH0},\lambda_{SH0}\right)}{A_s\left(\omega_{SH1},\lambda_{SH1}\right)}=\frac{E^{SH}(\omega_{SH0})F\left(\omega_{SH0}\right)H_{SE}(\lambda_{SH0},w)}{E^{SH}(\omega_{SH1})F\left(\omega_{SH1}\right)H_{SE}(\lambda_{SH1},w)}.$$

Since both modes are excited using the same temporal excitation,

$$\frac{F\left(\omega_{SH0}\right)}{F\left(\omega_{SH1}\right)} = 1.$$

Since the element width is $w = 0.1$ mm, the ratio of the single-element excitation spectra is less than -0.01 dB across the relevant frequency range, thus

$$\frac{H_{SE}\left(\lambda_{SH0}, w\right)}{H_{SE}(\lambda_{SH1}, w)} \approx 1.$$

For instance, at 400 kHz, $\lambda_{SH0} = 7.75$ mm and $\lambda_{SH1} = 8.41$, hence $\frac{H_{SE}(\lambda_{SH0}, w)}{H_{SE}(\lambda_{SH1}, w)} = 1.00$. Therefore, changes in the amplitude ratio of the two modes are attributed to the excitability function E only.

The displacement component in the examined cross section is shown in Figure B. 1(a). The displacement at the cross-section is selected at the corresponding times where modes SH0 and SH1 peak. Although the same energy is attributed to each mode, the surface displacement of mode SH0 is approximately half that of mode SH1. The time domain signal at the top surface is presented in Figure B. 1 (b). This difference in surface amplitude is attributed to the fact that $\frac{E^{SH}(\omega_{SH0})}{E^{SH}(\omega_{SH1})} = \frac{1}{2}$, as shown in equation (5.1).

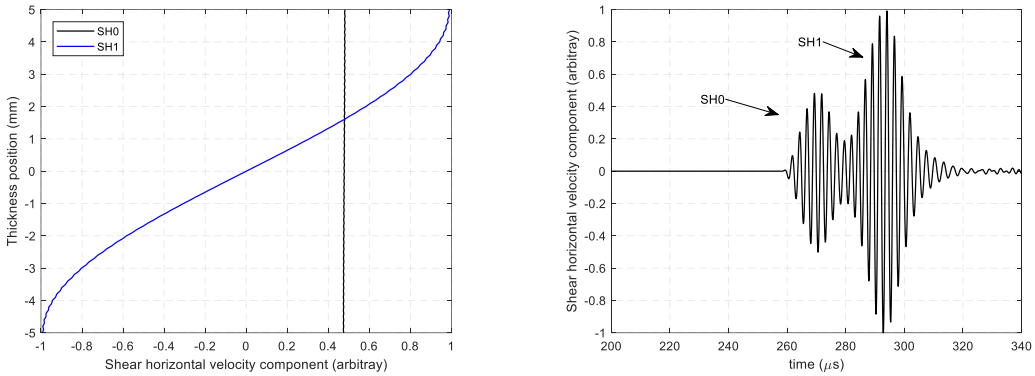

(a) (b)

Figure B. 1 Single element simulation: (a) Shear horizontal velocity component vs. through-thickness position of modes SH0 and SH1 and (b) A-scan signal at the top surface.

In the above analysis, the ratio $\frac{H_{SE}(\lambda_{SH0},\mathrm{w})}{H_{SE}(\lambda_{SH1},\mathrm{w})}$ is approximately one, thus the surface amplitude of each mode depends directly on the excitability function. However, this is not always true. For example, if a larger element width is used or the effects of dispersion are significant, calculation of the amplitude ratio becomes more complex.

References

[1] Holmes C, Drinkwater BW, Wilcox PD. Post-processing of the full matrix of ultrasonic transmit-receive array data for non-destructive evaluation. NDT E Int 2005;38:701–11. https://doi.org/10.1016/j.ndteint.2005.04.002.

[2] Le Duff A, Painchaud-April G. Phase Coherence Imaging for Flaw Detection. E-Journal Nondestruct Test 2022;27:1–12.

[3] Lewandowski M, Walczak M, Witek B, Steifer T. A GPU-based ultrasound Phased-Array research system for non-destructive testing. IEEE Int Ultrason Symp IUS 2016;2016-Novem:1–4. https://doi.org/10.1109/ULTSYM.2016.7728843.

[4] Alleyne DN, Pavlakovic B, Lowe MJS, Cawley P. Rapid, long range inspection of chemical plant pipework using guided waves. Key Eng Mater 2004;270–273:434–41. https://doi.org/10.4028/www.scientific.net/kem.270-273.434.

[5] Alleyne DN, Vogt T, Cawley P. The choice of torsional or longitudinal excitation in guided wave pipe inspection. Insight Non-Destructive Test Cond Monit 2009;51:373–7. https://doi.org/10.1784/insi.2009.51.7.373.

[6] Chandrasekaran J, Anto I, Balasubramaniam K, Venkataraman KS. Higher order modes cluster (HOMC) guided waves for online defect detection in annular plate region of above-ground storage tanks. Insight Non-Destructive Test Cond Monit 2009;51:606–11. https://doi.org/10.1784/insi.2009.51.11.606.

[7] K SHR, Rajagopal P, Balasubramaniam K, Hill S, Dixon S. Interaction of Higher

Order Modes Cluster (HOMC) guided waves with notch-like defects in plates Interaction of Higher Order Modes Cluster (HOMC) Guided Waves with Notch-like Defects in Plates 2017;030015. https://doi.org/10.1063/1.4974583.

[8] Harsha S, Reddy K, Vasudevan A, Rajagopal P, Balasubramaniam K. Scattering of Higher Order Mode Clusters (HOMC) from surface breaking notches in plates with application to higher temperature gradients. NDT E Int 2021;120:102441. https://doi.org/10.1016/j.ndteint.2021.102441.

[9] Shivaraj K, Balasubramaniam K, Krishnamurthy C V., Wadhwan R. Ultrasonic circumferential guided wave for pitting-type corrosion imaging at inaccessible pipe-support locations. J Press Vessel Technol Trans ASME 2008;130:0215021–12150211. https://doi.org/10.1115/1.2892031.

[10] Khalili P, Cawley P. The choice of ultrasonic inspection method for the detection of corrosion at inaccessible locations. NDT E Int 2018;99:80–92. https://doi.org/10.1016/j.ndteint.2018.06.003.

[11] https://www.inductosense.com/ n.d. https://www.inductosense.com/.

[12] Liu G, Qu J. Guided Circumferential Waves in a Circular Annulus. J Appl Mech 1998;65:424–430. https://doi.org/https://doi.org/10.1115/1.2789071.

[13] Rose JL. Ultrasonic Guided Waves in Solid Media. Cambridge University Press; 2014.

[14] Auld BA. Acoustic Fields and Waves in Solids, Volume 2. vol. 2. 2nd ed. R.E. Krieger; 1990.

[15] Achenbach JD. Wave Propagation in Elastic Solids. North-Holland Pub. Co; 1973.

[16] Graff KF. Wave Motion in Elastic Solids. Dover Publications; 1991.

[17] Lowe MJS, Alleyne DN, Cawley P. Defect detection in pipes using guided waves. vol. 36. 1998.

[18] Demma A, Cawley P, Lowe M, Roosenbrand AG, Pavlakovic B. The reflection of guided waves from notches in pipes: A guide for interpreting corrosion measurements. NDT E Int 2004;37:167–80. https://doi.org/10.1016/j.ndteint.2003.09.004.

[19] Leinov E, Lowe MJS, Cawley P. Ultrasonic isolation of buried pipes. J Sound Vib 2016;363:225–39. https://doi.org/10.1016/j.jsv.2015.10.018.

[20] Leinov E, Lowe MJS, Cawley P. Investigation of guided wave propagation and attenuation in pipe buried in sand. J Sound Vib 2015;347:96–114. https://doi.org/10.1016/j.jsv.2015.02.036.

[21] Nishino H, Masuda S, Mizobuchi Y, Asano T, Yoshida K. Long-range testing of welded elbow pipe using the T(0;1) mode ultrasonic guided wave. Jpn J Appl Phys 2010;49:0–6. https://doi.org/10.1143/JJAP.49.116602.

[22] Fiona Ravenscroft, Roger Hill CD& DB. CHIME- A New Ultrasonic Method for Rapid Screening of Pipe, Plate and Inaccessible Geometries. ECNDT'98—Proceedings Eur. Conf. Nondestruct. Test., Copenhagen: 1998.

[23] Burch SF, Collett NJ, Terpstra S, Hoekstra M V. M-skip: A quantitative technique

for the measurement of wall loss in inaccessible components. Insight Non-Destructive Test Cond Monit 2007;49:190–4. https://doi.org/10.1784/insi.2007.49.4.190.

[24] Sonomatic. CHIME ® Inspection n.d.

[25] LORENZ M, LEWANDOWSKI S. Ultrasonic Multi-Skip Inspection at Clamped Saddle Supports. 18th World Conf. NDT, 2012, p. 206.

[26] Holloway P, Ginzel R. PA-CAT TM : Measurement of Metal Loss at Pipe Supports Using an Innovative Phased Array Approach 2021:2–13.

[27] Holloway P, Jarv N, Ginzel E. Assessing Corrosion at Supports using PA-CAT n.d.:1–11.

[28] Wilcox P, Lowe M, Cawley P. Effect of dispersion on long-range inspection using ultrasonic guided waves. NDT E Int 2001;34:1–9. https://doi.org/10.1016/S0963-8695(00)00024-4.

[29] Alleyne DN, Cawley P. The Interaction of Lamb Waves with Defects. IEEE Trans Ultrason Ferroelectr Freq Control 1992;39:381–97. https://doi.org/10.1109/58.143172.

[30] Wang WD. ULTRASONIC LAMB WAVE TECHNIQUE FOR MEASUREMENT OF PIPE WALL THICKNESS AT PIPE SUPPORTS. 09/007,391, 1999.

[31] Lowe MJS, Diligent O. Low-frequency reflection characteristics of the s0 Lamb

wave from a rectangular notch in a plate. J Acoust Soc Am 2002;111:64–74. https://doi.org/10.1121/1.1424866.

[32] Jenot F, Ouaftouh M, Duquennoy M, Ourak M. Corrosion thickness gauging in plates using Lamb wave group velocity measurements. Meas Sci Technol 2001;12:1287–93. https://doi.org/10.1088/0957-0233/12/8/341.

[33] Dobie G, Gareth Pierce S, Hayward G. The feasibility of synthetic aperture guided wave imaging to a mobile sensor platform. NDT E Int 2013;58:10–7. https://doi.org/10.1016/j.ndteint.2013.04.002.

[34] Dobie G, Spencer A, Burnham K, Gareth Pierce S, Worden K, Galbraith W, et al. Simulation of ultrasonic lamb wave generation, propagation and detection for a reconfigurable air coupled scanner. Ultrasonics 2011;51:258–69. https://doi.org/10.1016/j.ultras.2010.10.004.

[35] Dobie G. Ultrasonic Sensor Platforms for Non-Destructive Evaluation. 2010.

[36] Ma J, Cawley P. Low-frequency pulse echo reflection of the fundamental shear horizontal mode from part-thickness elliptical defects in plates. J Acoust Soc Am 2010;127:3485–93. https://doi.org/10.1121/1.3409446.

[37] Hirao M, Ogi H. An SH-wave EMAT technique for gas pipeline inspection. NDT E Int 1999;32:127–32. https://doi.org/10.1016/S0963-8695(98)00062-0.

[38] Clough M, Fleming M, Dixon S. Circumferential guided wave EMAT system for pipeline screening using shear horizontal ultrasound. NDT E Int 2017;86:20–7. https://doi.org/10.1016/j.ndteint.2016.11.010.

[39] Andruschak N, Saletes I, Filleter T, Sinclair A. An NDT guided wave technique for the identification of corrosion defects at support locations. NDT E Int 2015;75:72–9. https://doi.org/10.1016/j.ndteint.2015.06.007.

[40] Trushkevych O, Dixon S, Tabatabaeipour M, Potter MDG, MacLeod C, Dobie G, et al. Calibration-free SH guided wave analysis for screening of wall thickness in steel with varying properties. NDT E Int 2023;135:102789. https://doi.org/10.1016/j.ndteint.2023.102789.

[41] Cirtautas D, Samaitis V, Mažeika L, Raišutis R, Žukauskas E. Selection of Higher Order Lamb Wave Mode for Assessment of Pipeline Corrosion. Metals (Basel) 2022;12. https://doi.org/10.3390/met12030503.

[42] Cirtautas D, Samaitis V, Mažeika L, Raišutis R. Detection and Classification of Uniform and Concentrated Wall-Thinning Defects Using High-Order Circumferential Guided Waves and Artificial Neural Networks. Sensors 2023;23. https://doi.org/10.3390/s23146505.

[43] Khalili P, Cawley P. Excitation of Single-Mode Lamb Waves at High-Frequency-Thickness Products. IEEE Trans Ultrason Ferroelectr Freq Control 2016;63:303–12. https://doi.org/10.1109/TUFFC.2015.2507443.

[44] Satyarnarayan L, Chandrasekaran J, Maxfield B, Balasubramaniam K. Circumferential higher order guided wave modes for the detection and sizing of cracks and pinholes in pipe support regions. NDT E Int 2008;41:32–43. https://doi.org/10.1016/j.ndteint.2007.07.004.

[45] Abbasi Z, Honarvar F. Contribution of Lamb wave modes in the formation of higher order modes cluster (HOMC) guided waves. Proc Inst Mech Eng Part C J Mech Eng Sci 2022;236:3595–605. https://doi.org/10.1177/09544062211042410.

[46] Reddy SHK, Vasudevan A, Rajagopal P, Balasubramaniam K. Scattering of Higher Order Mode Clusters (HOMC) from surface breaking notches in plates with application to higher temperature gradients. NDT E Int 2021;120:102441. https://doi.org/10.1016/j.ndteint.2021.102441.

[47] Chandrasekaran J, Krishnamurthy C V., Balasubramaniam K. Axial higher order modes cluster (A-HOMC) guided wave for pipe inspection. AIP Conf Proc 2010;1211:161–8. https://doi.org/10.1063/1.3362262.

[48] Harsha S, Reddy K, Vasudevan A, Rajagopal P, Balasubramaniam K, Reddy SHK, et al. Scattering of Higher Order Mode Clusters (HOMC) from surface breaking notches in plates with application to higher temperature gradients. NDT E Int 2021;120:102441. https://doi.org/10.1016/j.ndteint.2021.102441.

[49] Silva MZ, Gouyon R, Lepoutre F. Hidden corrosion detection in aircraft aluminum structures using laser ultrasonics and wavelet transform signal analysis. Ultrasonics 2003;41:301–5. https://doi.org/https://doi.org/10.1016/S0041-624X(02)00455-9.

[50] Rose JL, Barshinger J. Using Ultrasonic Guided Wave Mode Cutoff for Corrosion Detection and Classification. IEEE Ultrason. Symp., 1998.

[51] Zhu W, Rose JL, Barshinger JN, Agarwala VS. Ultrasonic Guided Wave NDT for Hidden Corrosion Detection. Res Nondestruct Eval 1998:205–25.

[52] Tuzzeo D, Scalea FL. Noncontact Air-Coupled Guided Wave Ultrasonics for Detection of Thinning Defects in Aluminum Plates Noncontact Air-Coupled Guided Wave Ultrasonics. Res Nondestruct Eval 2001. https://doi.org/10.1080/09349840109409687.

[53] Cao X, Zeng L, Lin J, Hua J. A Correlation-Based Approach to Corrosion Detection with Lamb Wave Mode Cutoff. J Nondestruct Eval 2019;38:1–16. https://doi.org/10.1007/s10921-019-0629-y.

[54] Suresh N, Balasubramaniam K. Remnant thickness quantification in small thickness structures utilising the cut-off property of A1 Lamb wave mode employing linear array elements. J Appl Phys 2022;131. https://doi.org/10.1063/5.0085102.

[55] Belanger P. High order shear horizontal modes for minimum remnant thickness. Ultrasonics 2014;54:1078–87. https://doi.org/10.1016/j.ultras.2013.12.013.

[56] Thon A, Bélanger P. EMAT design for minimum remnant thickness gauging using high order shear horizontal modes. Ultrasonics 2019;95:70–8. https://doi.org/10.1016/j.ultras.2019.03.006.

[57] Nurmalia, Nakamura N, Ogi H, Hirao M, Nakahata K. Mode conversion behavior of SH guided wave in a tapered plate. NDT E Int 2012;45:156–61. https://doi.org/10.1016/j.ndteint.2011.10.004.

[58] Nakamura N, Ogi H, Hirao M. Detection of Shear Horizontal Guided Waves Propagating in Aluminum Plate with Thinning Region. Jpn J Appl Phys

2011;50:07HC17. https://doi.org/10.1143/JJAP.50.07HC17.

[59] Pialucha T, Pavlakovic B, Alleyne D, Cawley P. Quantitative measurement of remnant thickness in corrosion under pipe supports. Insight - Non-Destructive Test Cond Monit 2020;62:642–8. https://doi.org/10.1784/insi.2020.62.11.642.

[60] Pialucha T. Determining a thickness of a region of wall- or plate- like structure. WO 2018/029445 A1, 2018.

[61] Suresh N, Balasubramaniam K. Quantifying the lowest remnant thickness using a novel broadband wavelength and frequency EMAT utilizing the cut-off property of guided waves. NDT E Int 2020;116:102313. https://doi.org/10.1016/j.ndteint.2020.102313.

[62] Miao H, Li F. Shear horizontal wave transducers for structural health monitoring and nondestructive testing: A review. Ultrasonics 2021;114:106355. https://doi.org/10.1016/j.ultras.2021.106355.

[63] Pialucha T. Transducer for guided wave inspection. GB 2552858, 2018.

[64] Frankel T. The Geometry of Physics. Cambridge University Press; 2011. https://doi.org/10.1017/CBO9781139061377.

[65] Krautkrämer J, Krautkrämer H. Ultrasonic Testing of Materials. Springer Berlin Heidelberg; 1990. https://doi.org/10.1007/978-3-662-10680-8.

[66] Auld BA, Kino GS. Normal Mode Theory for Acoustic Waves and its Application to the Interdigital Transducer. IEEE Trans Electron Devices 1971;18:898–908.

https://doi.org/10.1109/T-ED.1971.17303.

[67] Achenbach JD. Reciprocity in elastodynamics. Cambridge University Press; 2003.

[68] Craig RR. Structural Dynamics: An Introduction to Computer Methods. Wiley; 1981.

[69] Hagedorn P, DasGupta A. Vibrations and Waves in Continuous Mechanical Systems. Wiley; 2007. https://doi.org/10.1002/9780470518434.

[70] Koduru JP, Rose JL. Mode controlled guided wave tomography using annular array transducers for SHM of water loaded plate like structures. Smart Mater Struct 2013;22. https://doi.org/10.1088/0964-1726/22/12/125021.

[71] Alleyne DN, Cawley P. Optimization of lamb wave inspection techniques. NDT E Int 1992;25:11–22. https://doi.org/10.1016/0963-8695(92)90003-Y.

[72] Taheri H, Hassen AA. Nondestructive ultrasonic inspection of composite materials: A comparative advantage of phased array ultrasonic. Appl Sci 2019;9. https://doi.org/10.3390/app9081628.

[73] Cawley P, Alleyne D. The use of Lamb waves for the long range inspection of large structures. Ultrasonics 1996;34:287–90. https://doi.org/10.1016/0041-624X(96)00024-8.

[74] Kannajosyula H, Lissenden CJ, Rose JL. Analysis of annular phased array transducers for ultrasonic guided wave mode control. Smart Mater Struct 2013;22. https://doi.org/10.1088/0964-1726/22/8/085019.

[75] Veit G, Bélanger P. An ultrasonic guided wave excitation method at constant phase velocity using ultrasonic phased array probes. Ultrasonics 2020;102. https://doi.org/10.1016/j.ultras.2019.106039.

[76] Rose JL, Morrow P, Zhu Y. Ultrasonic Guided Wave Modal Analysis Technique (UMAT) for Defect Detection. Conf. Proc. Soc. Exp. Mech. Ser. , 2011.

[77] Koduru JP, Momeni S, Rose JL. Phased annular array transducers for omnidirectional guided wave mode control in isotropic plate like structures. Smart Mater Struct 2013;22. https://doi.org/10.1088/0964-1726/22/12/125022.

[78] Lee BC, Staszewski WJ. Lamb wave propagation modelling for damage detection: I. Two-dimensional analysis. Smart Mater Struct 2007;16:249–59. https://doi.org/10.1088/0964-1726/16/2/003.

[79] Faisal Haider M, Bhuiyan MY, Poddar B, Lin B, Giurgiutiu V. Analytical and experimental investigation of the interaction of Lamb waves in a stiffened aluminum plate with a horizontal crack at the root of the stiffener. J Sound Vib 2018;431:212–25. https://doi.org/10.1016/j.jsv.2018.06.018.

[80] Monkhouse RSC, Wilcox PD, Cawley P. Flexible interdigital PVDF transducers for the generation of Lamb waves in structures. Ultrasonics 1997;35:489–98. https://doi.org/10.1016/S0041-624X(97)00070-X.

[81] Gachagan A, Hayward G, Banks R. A flexible piezoelectric transducer design for efficient generation and reception of ultrasonic lamb waves. IEEE Trans Ultrason Ferroelectr Freq Control 2005;52:1175–82.

https://doi.org/10.1109/TUFFC.2005.1504004.

[82] Jayaraman C, Krishnamurthy C V., Balasubramaniam K. Higher order modes cluster (HOMC) guided waves - A new technique for ndt inspection. AIP Conf. Proc., vol. 1096, American Institute of Physics; 2009, p. 121–8. https://doi.org/10.1063/1.3114094.

[83] Tabatabaeipour M, Trushkevych O, Dobie G, Edwards RS, McMillan R, Macleod C, et al. Application of ultrasonic guided waves to robotic occupancy grid mapping. Mech Syst Signal Process 2022;163. https://doi.org/10.1016/j.ymssp.2021.108151.

[84] Rose JL, Pelts SP, Quarry MJ. A comb transducer model for guided wave NDE. vol. 36. 1998.

[85] Zhu W, Rose JL. Lamb wave generation and reception with time-delay periodic linear arrays: a BEM simulation and experimental study. IEEE Trans Ultrason Ferroelectr Freq Control 1999;46:654–64. https://doi.org/10.1109/58.764852.

[86] Li J, Rose JL. Implementing guided wave mode control by use of a phased transducer array. IEEE Trans Ultrason Ferroelectr Freq Control 2001;48:761–8. https://doi.org/10.1109/58.920708.

[87] Randall RB. Frequency analysis. Bruel and Kjaer, Naerum, Denmark; 1987.

[88] Wooh S-C, Shi Y. Optimum beam steering of linear phased arrays. vol. 29. 1999.

[89] Glushkov E V., Glushkova N V., Kvasha O V., Lammering R. Selective Lamb mode excitation by piezoelectric coaxial ring actuators. Smart Mater Struct 2010;19.

https://doi.org/10.1088/0964-1726/19/3/035018.

[90] Lines D, Wharrie J, Hottenroth J. Multi-Channel Ultrasound Toolbox: A Flexible Modular Approach for Real-Time Array Imaging and Automated Inspection. 2010.

[91] Alleyne D, Cawley P. A two-dimensional Fourier transform method for the measurement of propagating multimode signals. J Acoust Soc Am 1991;89:1159–68. https://doi.org/10.1121/1.400530.

[92] Wilcox PD. Omni-directional guided wave transducer arrays for the rapid inspection of large areas of plate structures. IEEE Trans Ultrason Ferroelectr Freq Control 2003;50:699–709. https://doi.org/10.1109/TUFFC.2003.1209557.

[93] Sicard R, Goyette J, Zellouf D. A SAFT algorithm for lamb wave imaging of isotropic plate-like structures. Ultrasonics 2002;39:487–94. https://doi.org/10.1016/S0041-624X(01)00087-7.

[94] Ghose B, Panda RS, Balasubramaniam K. Phase velocity measurement of dispersive wave modes by Gaussian peak-tracing in the f-k transform domain. Meas Sci Technol 2021;32. https://doi.org/10.1088/1361-6501/ac261b.

[95] Huber A. Dispersion Calculator (DC) 2018.

[96] L.Rose J. Joseph L.Rose - Ultrasonic Waves in solid media. Cambridge University Press; 2008.

[97] Zienkiewicz OC, Taylor RL, Fox DD. The Finite Element Method for Solid and Structural Mechanics. 7th ed. Elsevier Ltd.; 2014.

[98] Onscale software n.d. https://onscale.com/ (accessed May 18, 2023).

[99] Drozdz M, Moreau L, Castaings M, Lowe MJS, Cawley P. Efficient numerical modelling of absorbing regions for boundaries of guided waves problems. AIP Conf. Proc., vol. 820 I, 2006, p. 126–33. https://doi.org/10.1063/1.2184520.

[100] Cook RD, Malkus DS, Plesha ME, Witt RJ. Concepts and Applications of Finite Element Analysis, 4th Edition. 4th ed. Wiley; 2001.

[101] Thon A, Painchaud-April G, Duff A Le, Bélanger P. Development of a linear array electromagnetic acoustic transducer for shear horizontal guided wave inspection. NDT E Int 2023:102807. https://doi.org/10.1016/j.ndteint.2023.102807.

[102] Isla J, Cegla F. EMAT phased array: A feasibility study of surface crack detection. Ultrasonics 2017;78:1–9. https://doi.org/10.1016/j.ultras.2017.02.009.

[103] Petcher PA, Dixon S. Mode mixing in shear horizontal ultrasonic guided waves. Nondestruct Test Eval 2017;32:113–32. https://doi.org/10.1080/10589759.2016.1184268.

[104] Trushkevych O, Tabatabaeipour M, Dixon S, Potter MDG, Dobie G, Macleod C, et al. Miniaturised SH EMATs for Fast Robotic Screening of Wall Thinning in Steel Plates. IEEE Sens J 2021;21:1386–94. https://doi.org/10.1109/JSEN.2020.3021526.

[105] McMillan R, Tabatabaeipour M, Hampson R, Loukas C, Zhao T, Edwards RS, et al. Characterization of EMAT Guided Wave Reflectivity on Welded Structures for use in Ranging. IEEE Sens J 2022;23:4383–91.

https://doi.org/10.1109/JSEN.2022.3179326.

[106] Hirao M, Ogi H. EMATS for science and industry. Springer Science & Business Media; 2003.

[107] Mecademic n.d. https://www.mecademic.com/en/meca500-robot-arm (accessed May 18, 2023).

[108] Ritec n.d. https://www.ritecinc.com/ (accessed May 18, 2023).

[109] Pico Technology n.d. https://www.picotech.com/ (accessed May 18, 2023).

[110] Miao H, Huan Q, Li F. Excitation and reception of pure shear horizontal waves by using face-shear d24 mode piezoelectric wafers. Smart Mater Struct 2016;25. https://doi.org/10.1088/0964-1726/25/11/11LT01.

[111] Miao H, Huan Q, Wang Q, Li F. A new omnidirectional shear horizontal wave transducer using face-shear (d24) piezoelectric ring array. Ultrasonics 2017;74:167–73. https://doi.org/10.1016/j.ultras.2016.10.011.

[112] Miao H, Huan Q, Li F, Kang G. A variable-frequency bidirectional shear horizontal (SH) wave transducer based on dual face-shear (d24) piezoelectric wafers. Ultrasonics 2018;89:13–21. https://doi.org/10.1016/j.ultras.2018.04.010.

[113] Petcher PA, Dixon S. Weld defect detection using PPM EMAT generated shear horizontal ultrasound. NDT E Int 2015;74:58–65. https://doi.org/10.1016/j.ndteint.2015.05.005.

[114] Kogia M, Gan TH, Balachandran W, Livadas M, Kappatos V, Szabo I, et al. High

temperature shear horizontal electromagnetic acoustic transducer for guided wave inspection. Sensors (Switzerland) 2016;16:1–16. https://doi.org/10.3390/s16040582.

[115] Burrows SE, Fan Y, Dixon S. High temperature thickness measurements of stainless steel and low carbon steel using electromagnetic acoustic transducers. NDT E Int 2014;68:73–7. https://doi.org/10.1016/j.ndteint.2014.07.009.

[116] Carandente R, Cawley P. The effect of complex defect profiles on the reflection of the fundamental torsional mode in pipes. NDT E Int 2012;46:41–7. https://doi.org/10.1016/j.ndteint.2011.11.003.

[117] Liu P, Liu C, Zhang S, Wang Y, Wang Q. Depth-varying corrosion characteristics and stability bearing capacity of steel pipe piles under aggressive marine environment. Ocean Eng 2022;266:112649. https://doi.org/10.1016/j.oceaneng.2022.112649.

[118] Faro n.d. https://www.faro.com/ (accessed May 18, 2023).